

# Shared-Aperture 3D-Printed Dielectric Resonator Antenna Arrays for Millimeter-Wave Applications

by

Heba Imam Ahmed EL-Sawaf

A thesis  
presented to the University of Waterloo  
in fulfillment of the  
thesis requirement for the degree of  
Doctor of Philosophy  
in  
Electrical and Computer Engineering

Waterloo, Ontario, Canada, 2022

© Heba Imam Ahmed EL-Sawaf 2022

## Examining Committee Membership

The following served on the Examining Committee for this thesis. The decision of the Examining Committee is by majority vote.

External Examiner: Abdel Razik Sebak  
Professor, Dept. of Electrical Engineering,  
Concordia University

Supervisor(s): Kankar Bhattacharya  
Professor, Dept. of Electrical and Computer Engineering,  
University of Waterloo

Supervisor(s): Wael Mahmoud Abdel-Wahab  
Research associate professor,  
Dept. of Electrical and Computer Engineering,  
University of Waterloo

Internal-External Member: Eihab Abdel-Rahman  
Professor, Systems Design Engineering Dept.,  
University of Waterloo

Internal Member: Raafat Mansour  
Professor, Dept. of Electrical and Computer Engineering,  
University of Waterloo

Internal Member: Slim Boumaiza  
Professor, Dept. of Electrical and Computer Engineering,  
University of Waterloo

### **Author's Declaration**

I hereby declare that I am the sole author of this thesis. This is a true copy of the thesis, including any required final revisions, as accepted by my examiners.

I understand that my thesis may be made electronically available to the public.

## Abstract

With the increase in demand for higher data rates and higher bandwidth requirements, modern communication systems pursue innovative solutions that effectively utilize the high-frequency spectrum available at the Millimeter-wave (mm-wave) band and beyond (Terahertz bands). Phased arrays have found wide applications in satellite communication systems, especially with the decrease in implementation costs.

Phased array systems, operating at  $K$ -/  $K_a$ - bands, are considered the pillars of future communication systems. The advances in highly integrated circuits (ICs) allowed the full integration of transmitting and receiving channels in one chip. Thus, increased functionality in a small footprint can be achieved. However, phased array antennas are implemented by placing antenna platforms of each operating band next to each other. Therefore, the antenna platforms are space-consuming. Multiple radiators can utilize the same physical area, owing to the shared-aperture concept. However, fulfilling the performance requirement for radiators of each frequency band is a challenge. Limited work from the literature has been reported on shared aperture arrays operating in the mm-wave range with a small frequency ratio and with acceptable performance at both bands.

In this dissertation, the design, and verification of a novel shared aperture array is implemented using the dielectric resonator antennas (DRAs). With DRAs, the numerous flexible design aspects provide an advantage to meet the stringent requirement of shared-aperture arrays. Further, DRAs as non-metallic radiators are considered a good candidate for mm-wave applications due to their negligible ohmic loss. The 3D-printed technology is used in the realization of the DRAs. 3D-printing provides the advantage of design flexibility and dimensional accuracy as compared to machining methods. All the DRA designs are also fabricated using commercial machined substrates as a benchmark in comparison to the 3D-printed models. Up to the author's knowledge, this work is the first to compare the operation of 3D-printed DRAs with their counterparts. The presented shared-aperture array provides a low-cost solution for mm-wave applications. By properly designing the DRAs, the proposed technique can be further extended to modular form. An analysis of the effect of the orientation of the DRAs in the lattice of the multi-band structure on the antenna characteristics and the isolation between both bands is described.

Firstly, a single-DRA fed by substrate integrated coaxial line (SICL) at  $K$ -band is proposed to reduce the DRA feed circuit footprint. The design realizes a wide bandwidth of 3 GHz (19.95 - 23.04 GHz), 3 GHz (20.6 - 23.5 GHz) for the machined DRA, and 3D-printed DRA, respectively. The corresponding measured realized gains are 6.2 dBi, and 6 dBi for the machined DRA, and 3D-printed DRA, respectively. The measured co-polarization to the cross-polarization level is more than 30 dB for both DRAs.

Secondly, the design of a single-DRA fed by substrate integrated waveguide (SIW) at  $K_a$ -band on two substrate layers is described. The design realizes a wide bandwidth of 2.2 GHz (30.5 - 32.7 GHz), and 2.3 GHz (30.7- 33 GHz) for the machined DRA, and 3D-printed DRA, respectively. The corresponding measured realized gains are 5.5, and 5.3 dBi, respectively. The measured co-polarization to the cross-polarization level is more than 30 dB for both DRAs.

Thirdly, a  $K$ -/  $K_a$ - bands DRAs shared aperture sub-array is introduced using the adopted feeding techniques. The sub-array realizes isolation of more than 50 dB between both bands, wide bandwidth of operation of more than 2 GHz, and efficient utilization of aperture space. At the  $K$ - band, the machined and 3D printed DRA in the shared aperture configuration covered a broad -10-dB bandwidth of 5 GHz (19.5 to 24.5 GHz) and 5.5 GHz (21 to 26.5 GHz), respectively. At the  $K_a$ -band, the machined and 3D-printed DRA in the shared-aperture configuration covers a bandwidth of 2.4 GHz (30.7 to 33.4 GHz) and 2.3 GHz (31 to 33.3 GHz), respectively. The average realized gain is 9.25, 10 dBi for the  $K_a$ -band machined and 3D printed sub-array, and 6.3, 7 dBi for the  $K$ -band machined and 3D printed DRA in a shared sub-array configuration. The measured co-polarization to cross-polarization level is more than 30 dB for the  $K_a$ -band machined and 3D printed sub-array. For the  $K$ -band, the measured co-polarization to cross-polarization level is more than 26 dB, and 17 dB for the 3D printed and machined antenna in the shared array configuration.

Compared to other reported shared aperture arrays, the suggested sub-array achieved one of the state-of-art isolation and excellent radiation characteristics over a wide operating bandwidth. Moreover, the shared feeding space is efficiently utilized; by sharing the SIW walls with the SICL feeding lines. Furthermore, the PCB technology and 3D-printing allow full integration with planar circuits and efficient operation at mm-wave ranges compared to other reported fully metallic and bulky structures.

## Acknowledgements

All praise is due to Allah. I thank Allah for all the blessings that have been bestowed upon me since I began this course of my study, for his protection in difficult times and for all his givings to me.

This stage of my life wouldn't have been completed without Allah's grace, my supervisors' support, and my family and friends' care. I want to express my sincere gratitude to everyone who supported me throughout this journey.

I would like to thank my external examiner of my Ph.D. defence exam Prof. Abdel-Razik Sebak and my examination committee members; Prof. Slim Boumaiza, Prof. Raafat Mansour, and Prof. Eihab Abdel-Rahman for their valuable time in reviewing the thesis and for providing insightful feedback about my research. I would like to thank my supervisor, Prof. Kankar for all the support I received after Prof. Safavi's passing away.

My deepest gratitude to my supervisor "late Prof. Safieddin Safavi-Naeini" for allowing me to be part of CIARS family as his Ph.D. student, and for his valuable advice, patience and continuous support throughout my Ph.D. study. No words can describe the impact of the privilege of being under his supervision nor the pain of his loss. Prof. Safavi, you were a role model of how to be a humble, caring, kind, and knowledgeable leader. I have learned from him how to approach problems, and how to navigate through work and life challenges. I would never forget his enthusiasm and encouragement with my little successes and your support and wisdom when things seemed a bit tough for me. I haven't got the opportunity to learn from him everything, but I will follow all the lessons and teachings I witnessed in my life.

I would like to offer my deepest appreciation to my Co-supervisor, Dr. Wael Abdel-Wahab for his mentorship in my Ph.D. from introducing me to Professor Safavi-Naeini's group, and then guiding me in building my knowledge in almost all I now know about integration technologies, antenna design, and experimental expertise. Words cannot explain the extent of my gratitude for his invaluable support through my Ph.D. work, his tremendous assistance and teaching during the measurement stage in the lab and the thoroughly technical discussions.

A special thanks to CIARS team members; Chris Schroeder for her administrative support; Kaveh Feridani who patiently taught me lots of things; Seyed Ali Hosseini for the thorough discussions in research and life; Ardeshir Palizban for his technical support in preparing the fabrication files; Ahmed Ehsandar for his help in designing the mechanical support structures. I especially thank Naeimah Ghafarian who performed with me all antenna patterns measurements and for the continuous support in this process. I thank all

CIARs members for their continuous advice, constructive insights, and fruitful discussions in our previous group meetings. I have learned from all of you. The experience I have gained in CIARS group at the University of Waterloo was life-changing for me.

My father, Prof. Imam, and my mother Dr. Howayda, I am indebted to both of you for everything I achieved in my life. Your sacrifices, unconditional love, kindness, and endless support are behind any success I achieve. Without your duaas, I would have lost. The completion of the Ph.D. is the answer to your duaas and prayers for me. My brother, Mohamed, no words can describe how much I owe you. Thank you for everything you did and always do for me. You were always there when I needed you. My sister, Noha, the sweet of our family, thank you for all your support and encouragement to me when I was feeling lonely and down.

To my lovely husband, Ayman. Thank you for the many times you stood by me. Thank you for always believing in me and in what I can do. Thank you for pushing me to keep moving on when I lacked inspiration and lost confidence in myself. Thank you for helping me handle any stuff in difficult times. Thank you for your endless love, sacrifices and emotional support. I want you to know that this would not have been possible without you being with me.

To all my family – Thank you all for your encouragement and support. A special thank you to Uncle Abdelaziz Eltaliawy for his support

My heartfelt appreciation to all my dear friends in Waterloo with whom we shared lots of enjoyable memories in my Ph.D. journey and my friends in Port Said who were always checking on me and sending me good wishes. Thank you, Yasmin, Samar, Eman, and Heba.

I would like to take this opportunity to thank my supervisors in the master's degree, the late Professor Atef Ghuneim whose great lectures during my undergraduate study introduced me to electromagnetic and microwave theory and Prof. Ayman El-Tager for all his knowledge and support in my master's supervision. Special thanks to Dr. Heba Youssef Soliman for always being my role model in perseverance and hard work. Dr. Islam and Dr. Rania, no words can describe your impact on my life since my undergraduate studies. Thank you for all your support and help through the past years.

Without the contribution of each one mentioned above and for others, the journey could have been harder.

## Dedication

*To late Prof. Ali. whom we did not get a chance to say goodbye. May Allah rest him in peace, forgive his sins, and bring him to paradise.*

# Table of Contents

<b>List of Figures</b>	<b>xiv</b>
<b>List of Tables</b>	<b>xix</b>
<b>1 Introduction</b>	<b>1</b>
1.1 Mm-wave Motivation . . . . .	1
1.2 Satellite Communication: Overview, Existing systems . . . . .	4
1.3 Satellite Communication: Antenna Systems Technologies . . . . .	4
1.3.1 Electronically Steered Phased Arrays Antennas . . . . .	5
1.3.2 Reflectarrays . . . . .	5
1.4 Problem Definition and Research Objectives . . . . .	5
1.4.1 Phased Array Architectures . . . . .	6
1.4.2 Antenna Element . . . . .	8
1.4.3 Integration Technology . . . . .	9
1.4.4 Fabrication Technology . . . . .	10
1.5 Dissertation Organization . . . . .	10
<b>2 Literature Review of Shared-Aperture Phased Array Architectures</b>	<b>13</b>
2.1 Background . . . . .	13
2.2 Shared-Aperture Array Realization . . . . .	14
2.2.1 Interlaced Configuration . . . . .	15

2.2.2	Perforated Configuration . . . . .	16
2.2.3	Stacked Configuration . . . . .	17
2.2.4	Restructured Configuration . . . . .	18
2.3	Design Challenges of Shared-Aperture Arrays . . . . .	19
2.3.1	Mutual Coupling . . . . .	19
2.3.2	Grating Lobes . . . . .	19
2.3.3	Level of Integration . . . . .	19
2.3.4	Frequency Ratio . . . . .	20
2.4	Figures of Merits in Phased-Array Design . . . . .	20
2.4.1	Operating Frequency Band and Bandwidth . . . . .	20
2.4.2	Isolation between Frequency Bands . . . . .	21
2.4.3	Cross-Polarization Level . . . . .	21
2.5	Review of Recent Publications . . . . .	21
2.6	Conclusion . . . . .	24
<b>3</b>	<b>Shared Aperture DRA Arrays-Analysis</b>	<b>25</b>
3.1	Introduction . . . . .	25
3.2	Dielectric Resonator Antennas (DRAs) . . . . .	28
3.3	DRA Shared-Aperture Array Configuration . . . . .	29
3.4	Antenna Design . . . . .	29
3.4.1	Rectangular DRA . . . . .	31
3.4.2	Cylindrical DRA Design Procedure . . . . .	35
3.5	Sub-array Configuration . . . . .	37
3.6	Shared-Array Configuration . . . . .	42
3.6.1	Simulation Results . . . . .	42
3.7	Isolation Analysis . . . . .	45
3.8	Conclusion . . . . .	47

<b>4</b>	<b>Substrate Integrated Coaxial Line-Integrated DRA</b>	<b>49</b>
4.1	Introduction . . . . .	49
4.2	Planar Transmission Lines Technologies . . . . .	50
4.3	Substrate Integrated Coaxial Line . . . . .	51
4.3.1	Substrate Integrated Coaxial Line Characteristics . . . . .	52
4.3.2	Substrate integrated Coaxial Line-fed Antennas . . . . .	52
4.3.3	Analysis . . . . .	53
4.3.4	SICL Transitions . . . . .	53
4.3.5	SICL Versions . . . . .	54
4.4	SICL-fed DRA Design . . . . .	57
4.5	Simulation versus Measurement Results . . . . .	64
4.5.1	S-parameters . . . . .	66
4.5.2	Radiation Pattern Gain . . . . .	68
4.6	Sensitivity Analysis of Design Parameters . . . . .	68
4.7	Conclusion . . . . .	69
<b>5</b>	<b>Substrate Integrated Waveguide DRAs</b>	<b>70</b>
5.1	Substrate Integrated Waveguide- An overview . . . . .	70
5.1.1	Substrate Integrated Waveguide Characteristics . . . . .	71
5.1.2	Analysis . . . . .	72
5.1.3	SIW Transitions . . . . .	72
5.1.4	SIW Versions . . . . .	73
5.2	Ka-band SIW-fed DRA Design . . . . .	76
5.3	Simulation versus Measurement Results . . . . .	81
5.3.1	S-parameters . . . . .	82
5.3.2	Radiation Pattern Gain . . . . .	85
5.4	Sensitivity Analysis of Design Parameters . . . . .	85
5.5	Conclusion . . . . .	86

<b>6</b>	<b><i>K</i>-/<i>K<sub>a</sub></i>-bands Shared-Aperture Array</b>	<b>87</b>
6.1	Introduction . . . . .	87
6.2	Shared-aperture Array Configuration . . . . .	89
6.2.1	Sub-Array Configuration . . . . .	90
6.2.2	Principle of Operation . . . . .	90
6.2.3	Integration Feeding Technologies . . . . .	91
6.3	<i>K<sub>a</sub></i> -band Feeding Network and Shared-aperture Configuration . . . . .	93
6.3.1	Shared-aperture Simulation Results . . . . .	94
6.4	Fabrication and Material Characterization . . . . .	96
6.4.1	Machining DRAs . . . . .	97
6.4.2	3D-printing DRAs and Material Characterization . . . . .	97
6.5	Simulation versus Measurement Results . . . . .	98
6.5.1	S-parameters . . . . .	98
6.5.2	Radiation Patterns and Gain Measurements . . . . .	102
6.6	Comparison with Recent Literature . . . . .	103
6.7	Comment on Characterization . . . . .	105
6.8	Conclusion . . . . .	106
<b>7</b>	<b>Contributions and Future Work</b>	<b>107</b>
7.1	Contribution . . . . .	107
7.2	Future Work . . . . .	109
7.3	List of Publications . . . . .	110
	<b>References</b>	<b>112</b>
	<b>APPENDICES</b>	<b>129</b>
<b>A</b>	<b>Sensitivity Analysis of SICL-DRA Parameters</b>	<b>130</b>
A.1	Sensitivity of SICL-DRA Design Parameters . . . . .	130

<b>B Sensitivity Analysis of SIW-DRA Parameters</b>	<b>134</b>
B.1 Sensitivity of SIW-DRA Design Parameters . . . . .	134

# List of Figures

1.1	Mm-wave band, highlighting SatCom bands of operation. . . . .	2
1.2	Satellite communication possibilities in 5G [1] . . . . .	3
1.3	Miniaturization using shared-aperture arrays . . . . .	7
2.1	The two different realizations for co-aperture arrays [2] . . . . .	14
2.2	Shared-aperture dual-band interlaced array [3] . . . . .	16
2.3	Shared-aperture dual-band perforated array [4] . . . . .	17
2.4	Configuration of the stacked dual-band element [5] . . . . .	18
2.5	Configuration of the restructured antenna [6] . . . . .	18
3.1	Shared-aperture design procedure . . . . .	27
3.2	Proposed shared-aperture array configuration . . . . .	30
3.3	Aperture-fed DRA configuration . . . . .	31
3.4	Cross-section of the aperture fed rectangular DRA . . . . .	32
3.5	Reflection coefficient and radiated power of the square DRA (a)Rx (b)Tx .	33
3.6	Realized gain of the square DRA (a)Rx (b)Tx . . . . .	34
3.7	Radiation pattern gain of the square DRA . . . . .	34
3.8	Electric Field Distribution of the square DRA(V/m) . . . . .	35
3.9	Cross-section of the cylindrical DRA . . . . .	36
3.10	Reflection coefficient and radiated power of cylindrical DRA (a)TX (b)RX	37
3.11	Radiation pattern gain of the cylindrical DRA . . . . .	38

3.12	Electric Field Distribution of the cylindrical DRA . . . . .	38
3.13	$K$ -/ $K_a$ - band sub-array configuration . . . . .	39
3.14	The simulated reflection/coupling coefficient and radiated power of the interleaved sub-array . . . . .	40
3.15	The simulated realized gain of the sub-array. a)Rx b)Tx . . . . .	40
3.16	The radiation characteristics of the shared-aperture sub-array . . . . .	41
3.17	Full shared-array configuration . . . . .	42
3.18	The Reflection/coupling coefficients of the shared-aperture array . . . . .	43
3.19	The realized gain of the shared-aperture array a)Rx b)Tx . . . . .	43
3.20	The radiation characteristics of the shared-aperture array a)Rx b)Tx . . . . .	44
3.21	The isolation between The TX and RX DRAs . . . . .	44
3.22	Sub-array configuration . . . . .	45
3.23	The Reflection/coupling coefficients of the shared-aperture array . . . . .	46
3.24	The realized gain of the shared sub-array . . . . .	46
3.25	The radiation characteristics of the shared-aperture array a)Rx b)Tx . . . . .	47
4.1	Schematic of the substrate integrated technologies: a) SIW b) SICL . . . . .	49
4.2	Geometry of the SICL . . . . .	51
4.3	SICL modified versions a) ESICL b) MCTL c) RSICL d) ASICL e) SIDSL . . . . .	55
4.4	Proposed SICL-fed K-band DRA. a) Exploded view b) Cross-sectional view . . . . .	57
4.5	Geometry of the Proposed SICL-fed K-band DRA . . . . .	58
4.6	Propagation constant of the SICL-line a) higher order mode vs width b) propagating mode vs frequency . . . . .	59
4.7	The generated SICL modes a) Fundamental: TEM mode b) Higher order mode: TE <sub>10</sub> . . . . .	59
4.8	Reflection Coefficient the SICL-fed DRA versus a) DRA's length b) Slot longitudinal length . . . . .	60
4.9	Geometry of the Coaxial to SICL Transition . . . . .	61
4.10	Configuration of the B2B structure of the SICL . . . . .	62

4.11	Simulation results of the B2B SICL line . . . . .	62
4.12	Simulation results for the SICL-fed DRA. a) The S-parameters and Gain b) Radiation pattern gain . . . . .	63
4.13	Fabricated PCB boards a) $K$ -band antenna boards b) B2B circuit boards . . . . .	64
4.14	SICL fed DRA: Measured Vs simulated Reflection coefficient and Gain . . . . .	65
4.15	SICL-back to back transition: Measured Vs simulated Return S-parameters . . . . .	65
4.16	Measured vs simulated normalized radiation patterns of the 3D-printed $K$ -band antenna . . . . .	66
4.17	Measured vs simulated normalized radiation patterns of the machined $K$ -band antenna . . . . .	67
4.18	Measured vs simulated realized gain and directivity of the $K$ -band DRA . . . . .	67
5.1	Schematic of the substrate integrated waveguide implementation: a) Circular vias b) Rectangular trench . . . . .	71
5.2	SIW modified versions a) Sub-mode SIW b) T-FSIW c) C-FSIW d) RSIW e) SISW f) Slow-wave SIW . . . . .	74
5.3	Proposed SIW-fed $K$ -band DRA. a) Exploded view b) Top and Cross-sectional views . . . . .	77
5.4	Structure of the SIW-DRA antenna. . . . .	78
5.5	Structure of the SIW-B2B structure . . . . .	78
5.6	Simulation results of the B2B SIW line . . . . .	79
5.7	Simulation results of the SIW-fed DRA: a) The S-parameters and Gain b) Radiation pattern gain . . . . .	79
5.8	Fabricated PCB boards a) $K_a$ -band antenna boards b) B2B circuit boards . . . . .	81
5.9	SIW-fed DRA: Measured Vs simulated reflection coefficient and gain . . . . .	82
5.10	SIW-back to back transition: Measured Vs simulated S-parameters . . . . .	83
5.11	Parametric analysis of gap effect on the SIW-back to back transition . . . . .	83
5.12	Measured vs simulated normalized radiation patterns for the 3D-printed $K_a$ -band antenna . . . . .	83
5.13	Measured vs simulated normalized radiation patterns for the machined $K_a$ -band antenna . . . . .	84

5.14	Measured vs simulated realized gain and directivity of the $K_a$ -band DRAs	84
6.1	Proposed shared-aperture DRA sub-array. (a) Exploded view (b) Cross-sectional view	90
6.2	Electric field distribution when $K_a$ band DRAs excited a) 30 GHz b) 20 GHz	91
6.3	Geometry of the proposed shared-aperture	92
6.4	Field distribution in the shared-aperture sub-array (a) $K_a$ -band array excited, with $K$ -band match-loaded (b) $K$ -band excited, with $K_a$ -band match-loaded	93
6.5	Simulated S-parameters of the shared-aperture sub-array:(a) $K$ -band (b) $K_a$ -band	94
6.6	Simulated radiation pattern gains of the shared-aperture sub-array a) $K$ -band, b) $K_a$ -band	95
6.7	3D-printing characterization. a) 3D-printed samples b) DAK-TL setup	96
6.8	Fabricated PCB boards and 3D-printed sheets of the $K$ -/ $K_a$ -shared-aperture	98
6.9	Measured vs simulated reflection coefficient and gain of the shared-aperture 3D-printed sub-array a) $K$ -band b) $K_a$ -band	99
6.10	Measured vs simulated reflection coefficient and gain of the shared-aperture machined sub-array a) $K$ -band b) $K_a$ -band	100
6.11	Measured vs simulated normalized radiation patterns of the 3D-printed $K_a$ -band sub-array in shared-aperture configuration	100
6.12	Measured vs simulated normalized radiation patterns of the machined $K_a$ -band sub-array in shared-aperture configuration	101
6.13	Measured vs simulated normalized radiation patterns of the 3D-printed $K$ -band antenna in shared-aperture configuration	101
6.14	Measured vs simulated normalized radiation patterns of the machined $K$ -band antenna in shared-aperture configuration	102
6.15	Simulated S-parameters for solid model vs 3D-Printed model	105
A.1	Reflection coefficient variation with a) $L_{S2}$ b) $W_{S2}$ c) $L_{S1}$ d) $W_{S1}$	131
A.2	Reflection coefficient variation with a) $W_y$ b) $L_{Stub}$ c) $L_w$ d) $W_{MSL}$	131

A.3	Reflection coefficient variation with a) $d_{pin}$ b) $r_{pad}$ c) $D_{pad2}$ d) $D_{cut2}$ . . . . .	132
A.4	Reflection coefficient variation with a) $L_t$ b) $W_t$ c) $d_{pad}$ . . . . .	132
A.5	Reflection coefficient variation with a) $R_x$ b) $h_{Rx}$ . . . . .	133
B.1	Reflection coefficient variation with a) $L_{st}$ b) $W_{slot}$ . . . . .	134
B.2	Reflection coefficient variation with a) $d_{pad2}$ b) $d_{dp2}$ c) $D_{cut2}$ . . . . .	135
B.3	Reflection coefficient variation with a) $L_{Dt}$ b) $Y_{c1}$ c) $L_{w1}$ . . . . .	135
B.4	Reflection coefficient variation with a) $L_{DRA}$ b) $h_{DRA}$ . . . . .	136

# List of Tables

2.1	Reported publication on shared aperture arrays . . . . .	22
3.1	Required specifications for the proposed interleaved phased array . . . . .	26
3.2	DRA elements dimensions . . . . .	33
3.3	DRA elements dimensions . . . . .	36
4.1	Geometrical dimensions of the SICL-DRA antenna in (mm) . . . . .	58
4.2	Geometrical dimensions of the SICL-B2B structure in (mm) . . . . .	62
5.1	Geometrical dimensions of the SIW-DRA antenna in (mm) . . . . .	80
5.2	Geometrical dimensions of the SIW-B2B structure in (mm) . . . . .	80
6.1	Target specification for shared-aperture array . . . . .	89
6.2	Geometrical dimensions of the shared-aperture feeding network in (mm) . . . . .	94
6.3	Average Simulated vs Measured Shared-aperture Antenna Parameters . . . . .	103
6.4	Performance Comparison with Recent Literature . . . . .	104

# Chapter 1

## Introduction

Nowadays, the continuous demand for high-quality data services has led the drive to move to millimetre-wave (mm-wave) frequencies, seeking more bandwidth to fulfill the consumers' needs [7]. Taking the current COVID-19 pandemic as an example, technology played a vital role in creating an alternative virtual environment to our previous life by connecting people and devices, commonly known now as ( the new normal). Internet usage and mobile network traffic have increased by more than 40 % the last year [8], with an expectation that the trend will massively increase in the next couple of years. In the era of "Tele-Everything" from medicine and education to travel, there is a high demand for broadband video services, which means higher and higher data rates. Further, real-time transmission and reception are of utmost importance in self-driving vehicles in which latency and transmission speed are crucial [9]. On the other hand, there are still communities in rural areas that are not served by appropriate data connections. Thus, the extreme bandwidth available at mm-wave emerged as the potential solution for those demands. Those benefits come at the price of increased system complexity to mitigate the unwanted propagation characteristics of mm-wave radiation. With the recent advances in manufacturing technologies in both circuits and antennas, it is now possible to have systems for market mass commercial production at the mm-wave band.

### 1.1 Mm-wave Motivation

Fig. 1.1 represents the electromagnetic spectrum, highlighting the current applications operating at those bands. Most commercial wireless networks use the sub-6 GHz band, covering narrow bandwidth. However, the mm-wave spectrum can support higher operation

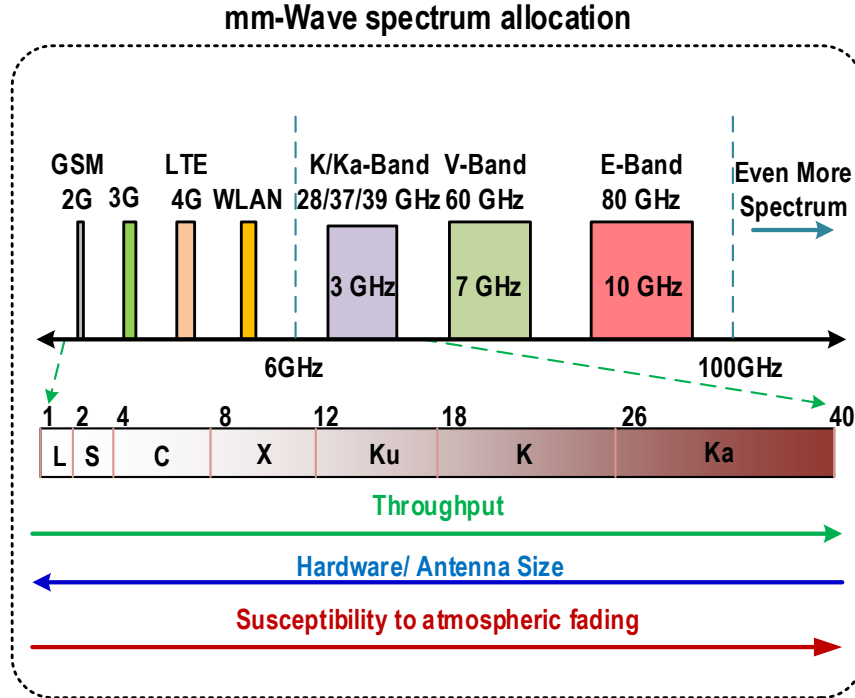


Figure 1.1: Mm-wave band, highlighting SatCom bands of operation.

bandwidth, covering frequencies from 30 to 300GHz. Earlier on, non-cellular satellite and military communication systems are the industries profiting from using mm-wave bands. The legalization of commercial mm-wave bands is opening opportunities for growth in two main sectors: 5G- and satellite communications (SatCom). Further, SatCom systems have great potential for speeding the implementation of 5G-systems [10], benefiting from the inherent well-established research in this domain, as demonstrated in Fig.1.2. Integrating SatCom-based systems into 5G- is promising in the following scenarios: Supplying high-speed links to central gateways, backhauling to local cells, Communication on the move to mobile units (SatCom on the move), and even multicast to individual urban areas [11] Moreover, the recent advances in manufacturing, computation capabilities, and higher integration levels are promising in enabling the production of miniaturized dense components in mm-wave systems. Furthermore, substrates manufacturers are currently supplying lam-

inates, targeting efficient performance at higher frequency bands. Accordingly, the diverse available resources available are releasing the barrier to developing cost-effective mm-wave systems for mass production. Thus, opening new challenges for the system implementation and introducing novel topics in multidisciplinary research areas.

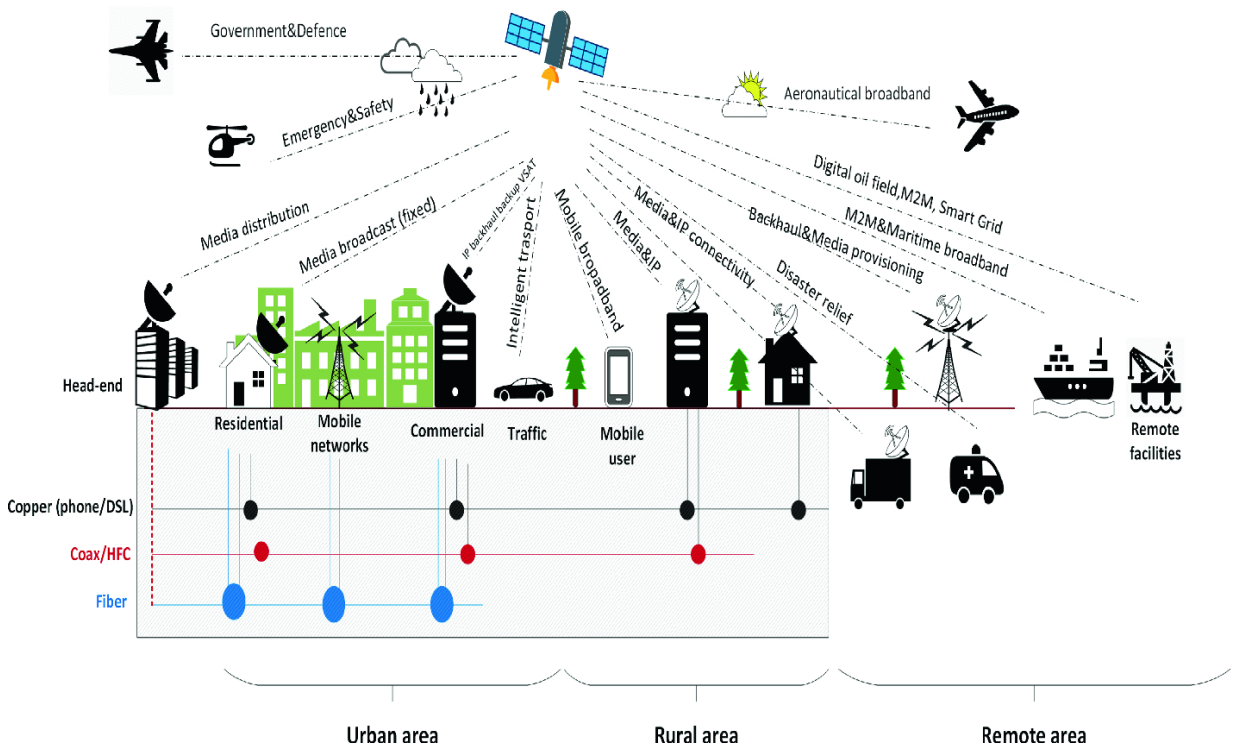


Figure 1.2: Satellite communication possibilities in 5G [1]

Communication systems operating in mm-wave are expected to fulfill various demands, including the size, required performance, and cost. Specifications target miniaturized, compact, and low-profile structures. Miniaturization also directly impacts the complexity of integration and component shielding in modules. Further, mm-wave signals are subject to severe atmospheric conditions, resulting in path loss, signal blockage, and interference problems. Therefore, highly directive antenna arrays are considered in combatting atmospheric attenuation. Moreover, the choice of low loss components is essential, including interconnects, antennas, and feed lines. All of the stated factors pose rigorous design requirements on both the circuit and antenna level to achieve highly-integrated solutions, enabling low-cost wireless communication systems.

## 1.2 Satellite Communication: Overview, Existing systems

Satellite communication(SatCom) systems operate at wide range frequency bands (up to 50 GHz) as presented in Fig. 1.1 [12,13]. SatCom systems, previously targeting only data broadcasting, navigation, and military operation applications [14], are now promising in 5G-systems inclusion. Satcom systems operating at  $K$ -/ $K_a$ -band have been identified as pillars of the "future internet" architecture [15]. However, SatCom terminals have to cope with several challenges at Ka-band [16]. High gain directive beams are required to combat the atmospheric attenuation while moving to the higher spectrum, as mentioned in the previous section [17] [18].

Satellite stations are categorized into Low Earth Orbit (LEO), Medium Earth Orbit (MEO), and Geostationary Earth Orbit (GEO), based on their orbital features. Mm-wave SatCom through LEO and MEOs provides robust signal quality and controlled latency with minor time delay than GEO systems. Moreover, hybrid constellations are established, combining advantages of both traditional and newly developed ones [13].

## 1.3 Satellite Communication: Antenna Systems Technologies

This section will highlight the antenna architectures suitable for SatCom systems, covering the well-developed antenna solutions: reflectors, phased arrays, reflectarrays antennas. Traditionally, mechanically-steered parabolic reflectors have been used exclusively in ground terminals of diverse applications, providing high gain and directivity. Driven by the need for miniaturizing, the concept of reconfigurable flat panel antennas (FPAs) evolved as a compact, low profile, lightweight solution to its bulky counterpart, parabolic reflectors. Challenging to achieve similar RF performance to the high gain reflectors while maintaining the commercial market needs, research has been ongoing on FPAs to provide a versatile solution for all those constraints. Some FPAs targeted fixed-direction radiation patterns with mechanical steering capability; however, their implementation still suffers from a higher profile due to the associated mechanical attachments. The main implemented categories in this group will be highlighted.

### 1.3.1 Electronically Steered Phased Arrays Antennas

Electronically steered phased arrays (ESPA) are composed of antenna arrays, excited by a combination of series- and corporate- feed networks, and integrated with phase shifters in a specific arrangement. Changing the relative phase between the radiators produces a directed beam in a specific direction while suppressing radiation in other directions. One of the challenges in the implementation of fully ESPA is their large footprint and the deterioration of the RF performance with scan angle. The latter is enhanced using digital processing techniques. On the other hand, ESPA is featured by their low profile, low-cost manufacturing using printed circuit boards (PCBs), and scalability due to modularity. ESPA in the mm-wave range is promising; however, the lossy feeding network, conductor losses, and narrow bandwidth of printed antennas are essential considerations for the proper implementation. In conclusion, miniaturized high-efficient antennas and low manufacturing costs are the critical challenges at those frequencies.

### 1.3.2 Reflectarrays

Reflectarrays, featuring reflector-based and planar array antenna characteristics, are realized to achieve a high gain focused beam. Reflectarrays are composed of tunable radiating elements (i.e., printed antennas, dielectric resonator antennas) and a suspended feeding source. Resonant-loaded radiating elements compensate for the phase delay from the source feed, accordingly controlling the required direction of the radiated beam. The drawback of this structure is narrow bandwidth behaviour, therefore, limiting their applications.

## 1.4 Problem Definition and Research Objectives

Section 1.3 presented an overview of the potential of satellite communication systems in mm-wave ranges, highlighting the significant fulfilling needs to provide compact broadband systems that feature low-cost implementation for mass production. In this context, phased array systems present a great potential to fulfill those requirements. Phased array technology brings tremendous advantages. Besides, it introduces significant challenges, especially at mm-wave frequencies. In addition, the electronic beam steering feature provides fast beam scanning [19]. Thus, it increases the reliability of the system. Further, the Use of multiple directive beams allows spectral reuse [19]. Thereby, the system capacity increases.

Focusing on the development of low-cost wideband low-profile antenna solutions, the radiating elements should provide vast bandwidth operation while fulfilling a compact, low-

profile nature. The metallic antennas, commonly used in the phased-array application, are limited by the narrow bandwidth. In addition, achieving large bandwidth require using thick substrates or introducing air cavities accordingly, multilayer stack up is required, which impacts low profile requirement. Further, advances in millimetre-wave (mm-wave) monolithic integrated circuit fabrication technologies allowed multifunctional TX and RX chipsets to target miniaturization and mass production at a low cost. On the other hand, implementing Rx and Tx radiators on separate platforms increases the phased array system's overall size and cost. Therefore, it is of utmost necessity to integrate the antenna functionalities of both the Tx and Rx band radiators on the same platform. Accordingly, the Ph.D. research work's vision was to investigate the enabling technologies and develop a proof-of-concept prototype for a low-cost, wideband, scalable, and modular phased array system. This vision is fulfilled through developmental efforts on four main aspects: the phased array architecture, the antenna element, the integration technologies, and the fabrication technology.

### 1.4.1 Phased Array Architectures

Multifunctional phased array systems, such as SatComs, commonly require simultaneous operation operating over two or more separated frequency bands. Undoubtedly, implementing such a phased array using a separate platform, placed side by side, benefits from increased flexibility in choosing the required specifications. Nevertheless, miniaturization of radiating aperture, implemented by combining the required multiband antenna functionalities in one platform, will significantly reduce the size and cost of phased arrays. This system demand can be fulfilled using three-antenna array elements implementations: broad bandwidth elements covering the required frequency bands, multiband antenna elements, and separate antennas for each frequency band on the same aperture.

For instance, Vivaldi antennas and tightly coupled arrays are examples of implementing radiating apertures using ultrawideband antenna arrays. Multibeam wide-scan capabilities with enhanced system performance and minimal aperture size are achieved. However, a higher antenna profile is needed for wide frequency range operation, mainly due to a backed ground plane. Further, those structures suffer from complex integration mechanisms. Accordingly, their increased cost and hard-to assemble nature limit their practical usage, especially at mm-wave frequencies. The reason for this is the need for external baluns or hybrids integration and special machining requirements. In addition, the cell size in the tightly coupled array is tiny, which results in very complex integration and routing problems. Moreover, the elements are too dense at the lower frequency band operation. Accordingly, more T/R modules are required. Hence, this approach will cause increased

cost and weight. Further, the complexity of the feed circuit occurs with dual-polarization excitation.

Multiband antennas are as well featured with minimal aperture size. However, achieving the required system specifications is mainly challenging. Realizing the desired bandwidth at the operating frequencies is one possible limitation since thick substrates are usually required. In addition, achieving dual polarization with attractive isolation between the two bands requires a complicated feeding circuit because of the difficulty of signal routing and fulfilling the required isolation between both states of operations. In addition, this approach is more appropriate for applications where the frequency ratio between elements is small (usually less than two).

Shared antenna arrays are implemented by segmentation the radiating aperture for multiple radiators. Individual radiators are simultaneously operating each at their respective functionality, maximizing the aperture efficiency, as illustrated in Fig. 1.3. Allowing the radiators at two different frequency bands to share the same aperture can be considered array miniaturization from the system's point of view. Accordingly, the overall form factor and weight are minimized. In our dissertation, shared-aperture arrays are employed as the basic array architecture.

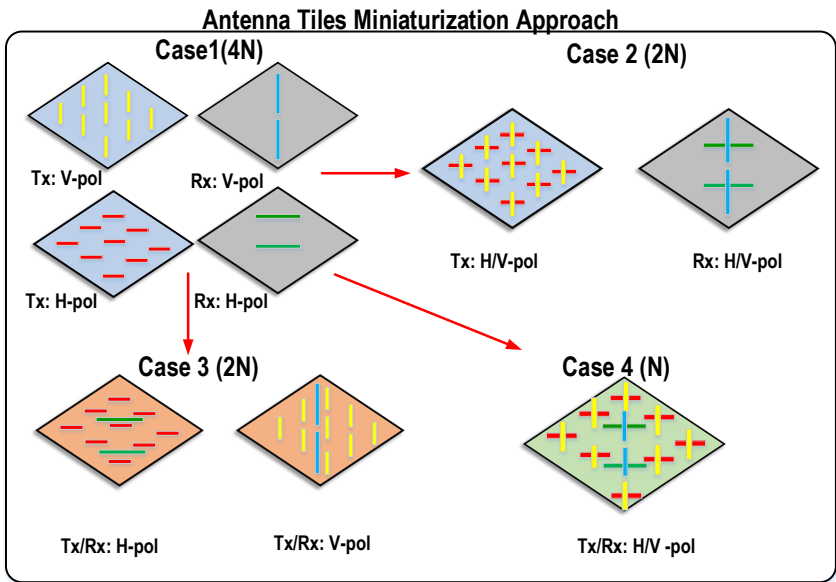


Figure 1.3: Miniaturization using shared-aperture arrays

## 1.4.2 Antenna Element

Focusing on the radiating element, the increasing demands of mm-wave systems require highly-efficient radiators while preserving a reduced footprint. Aperture antennas, for instance, reflector-based and lens antennas, are well-established antennas, characterized by excellent radiation characteristics, at the expense of high profile and high manufacturing costs. On the other hand, printed front-end antennas implemented for mm-wave applications, such as microstrip antennas, and integrated on-chip antennas, are featured by integrability with the solid-state device. In addition, their low profile, lightweight, and low manufacturing cost make them appealing choices for mm-wave mass production applications. Meanwhile, integrated on-chip antennas suffer from poor radiation efficiency, owing to the electrical properties of the IC's silicon substrate. Moreover, microstrip antennas' performance depends on the conductor's losses, substrate's behaviour at high frequencies, and thickness. Therefore, advanced integrated solutions, such as dielectric superstrates and lenses, are typically required to enhance the radiation efficiency, and impedance bandwidth [20].

Alternatively, Dielectric resonator antennas (DRAs) are favourable alternatives to traditionally used metallic radiating elements in high-frequency applications, especially in the mm-wave band. This is mainly attributed to the fact that DRAs do not present conduction losses and are featured by high radiation efficiency. Several methods have been reported for DRA excitation, similar to those used with microstrip antennas. Arraying the DRAs is desirable for high-gain beamforming/steering applications. Additionally, DRAs' design provides a level of flexibility, other than metallic antennas restricted by resonant length. Owing to the mentioned advantages, DRAs are chosen for our shared-aperture implementations. Our research work begins by investigating the achievable performance using DRAs in shared aperture configurations, targeting  $K$ - and  $K_a$ -bands.

Chapter 3 of the thesis is devoted to illustrating the design criteria implemented for those antennas. Further, enhancing the aperture efficiency of such antennas is demonstrated by integrating DRAs with substrate integrated feeding technologies, which is addressed in the next section. Objectively, the low-cost implementation of DRAs at higher frequencies is challenging due to limitations in fabrication technologies. Therefore, our research proposes using additive manufacturing technologies in order to provide a low-cost implementation for mass production.

### 1.4.3 Integration Technology

Integration of mm-wave components has a pivotal role in manufacturing efficient and reliable systems, leveraging low-cost mass production [21]. Commonly, microstrip lines and their variants such as coplanar waveguide (CPW) and grounded coplanar waveguide (GCPW) are used as the feeding mechanism for planar antennas owing to their ease of integration with active components. Further, electromagnetic coupling, for instance, aperture feeding through slots, is preferred at high frequencies to avoid spurious radiation. However, their parasitic coupling and low power handling capabilities are noticeable at mm-wave ranges. The beginning of this century witnessed the breakthrough technology class, the substrate integrated waveguides (SIWs). SIW technology-enabled planar synthesizing of the commonly highly efficient non-planar guiding structures (i.e., waveguides). Afterward, a vast range of high-performance SIW components and diverse forms have been proposed, allowing impeccable integration with planar transmission lines using low-cost processing technologies.

SIW transmission line, proposed in [22], aimed to attain the advantages of rectangular waveguides, with the convenience of fully planar realization and simplicity of integration with other planar circuits. The SIW is composed of two rows of metalized vias, connecting the top and bottom metal plates of a dielectric substrate [22]. Similar to the rectangular waveguide, the side walls confine the propagating wave within the substrate layer. Likewise, SIW supports the fundamental  $TE_{10}$  propagation mode. Advantaged by the integrated substrate, the height and the overall size of the SIW are less than the conventional 3-D waveguide.

Correspondingly, substrate integrated coaxial line (SICL) has been proposed in [23] as a substrate integrated correspondent to the coaxial line. The SICL consists of a rectangular coaxial structure, printed inside a substrate, and shielded by metalized via on both sides [23]. The SICL supports the  $TEM$  mode, acquiring the same advantages as non-planar coaxial lines. Besides, It provides flexible integration with planar structures and low-cost fabrication using standard printed circuit board manufacturing technique [21]. Diverse components and design techniques have been lately demonstrated in the literature for different applications using SICL.

In our dissertation, a hybrid structure combining SIW and SICL technologies is suggested to provide two orthogonal uncoupled transmission modes,  $TE_{10}$  and  $TEM$ , respectively. This strategy is one of the implemented techniques to provide a high level of isolation between radiators in the shared-aperture configuration. The hybrid feeding network will be performed by feeding the Rx DRA by the SICL and the Tx DRA by the SIW. The standalone radiators' design is presented in Chapters 4 and 5.

#### 1.4.4 Fabrication Technology

Commercializing mm-wave systems requires decent enhancement in technological constraints, including, but not limited to, reducing features' size and weight and minimizing manufacturing cost. Therefore, the fabrication of modernized antenna solutions desires, concurrently, to endorse peculiar electromagnetic (EM)-compatible design approaches and to incorporate leading-edge manufacturing techniques [24]. Over the last few years, the satellite industry made use of miniaturized components, investing in 3D printing and laser technology. 3D printing offers various advantages, such as increased production speed and complex manufacturing capabilities. The recent advances in 3D-printing technology regarding available materials and featured tolerances have promoted more significant degrees of freedom, cost-effectiveness, and feasibility of scale manufacturing. Mainly, superior antenna performance, achieved by tailoring electromagnetic radiation, is currently achievable using 3D-printed complex structures. Therefore, 3D-printing microwave components have been lately an attractive research topic for mm-wave applications.

For our dissertation, 3D printing technology [25] is introduced for the fabrication of DRA, benefiting from its advantage of manufacturing 3D shapes with high precision. Dielectric 3D printing involves different methods, differing in the feature size limitation, available materials, and final product features (i.e., surface roughness, homogeneity). Fused Filament Fabrication (FFF), commonly known as Fused Deposition Modeling (FDM), is one method based on extruding heated filament and deposited through a nozzle. The limitation of the FDM method lies in the surface finish and the unavoidable occurrence of voids in the 3D-printed parts. Therefore, proper characterization is required to ensure the 3D-printed EM performance, as designed. The process of the 3D-printed DRAs, characterization, and challenges related to both processes are discussed in Chapter 6.

Furthermore, the DRAs' feeding circuit is implemented using a simple stack-up, leveraging the low-cost standard printed circuit board technology. In addition, the proposed shared-feed network will allow easy implementation without several buried vias.

### 1.5 Dissertation Organization

This dissertation describes the approach to implementing a shared-aperture array using dielectric resonator antennas.

Chapter 1 introduced the context and the motivation of this Ph.D. research work, offering an overview of the mm-wave communication, from the allocated spectrum to the

technological challenges. A particular emphasis is given to presenting the potential of phased array SatComs at  $K$ - and  $K_a$ - band for a cost-effective, low-profile antenna solution. The aspects of the proposed implementation are introduced.

Chapter 2 presents the concept of shared-aperture arrays, from the different realized configurations and the novel implementations to this concept, together with the introduced antenna solutions. A significant emphasis is placed on highlighting the challenges in shared-aperture arrays' implementation. The benchmark performance of the published shared-aperture arrays is investigated, focusing on the work targeting the  $K$ -/ $K_a$ -bands. The goals of the Ph.D. work are then discussed, highlighting which aspects are maintained for an efficient antenna to be scaled for low-cost modular phased array applications.

Chapter 3 reviews the dielectric resonator antennas for mm-wave applications and the principle of operation of aperture-fed dielectric resonator antennas. The design of linearly-polarized dielectric resonator antennas operating at  $K$ - and  $K_a$ -bands is elaborated. A preliminary sub-array design is proceeded to analyze the performance of the suggested antenna in interlaced configuration. Then, the coupling between the  $K$ - and  $K_a$ -bands antenna is presented, followed by the implemented design approach to increase the isolation between the antennas by appropriately locating the antennas relative to each other. Finally, a conclusion of the expected performance for using the suggested antenna concludes the chapter, and the suggested substrate integrated feeding mechanism for both  $K$ -/ $K_a$ -bands to further enhance the isolation.

Chapter 4 presents the substrate integrated coaxial line fed DRA for  $K$ -band operation, highlighting the development of this technology, its advantages, the related presented integrated antennas, and transitions to other technologies in literature. The design of the integrated dielectric resonator antenna with substrate integrated coaxial line is discussed, along with the principle of operation. The dielectric resonator antenna fabrication using 3D printing is highlighted, in addition to a machined prototype as a benchmark for comparison. Measurement results of the prototypes are discussed, highlighting key features of the suggested antenna.

Chapter 5 presents the substrate integrated waveguide fed DRA for  $K_a$ -band operation, reviewing the development of this technology, its advantages, the related presented integrated antennas, and transitions to other technologies in literature. The design of the integrated dielectric resonator antenna with substrate integrated waveguide is discussed. The dielectric resonator antenna fabrication using 3D printing is highlighted, in addition to a machined prototype as a benchmark for comparison. Measurement results of the prototypes are discussed, highlighting the key benefits of the proposed implementation.

Chapter 6 presents the proposed  $2 \times 2$  shared-aperture array, along with the associ-

ated feeding network for the  $K_a$ -band. The main features of the proposed sub-array are compared with published literature working at the same frequencies.

Chapter 7 concludes this work with conclusions and perspectives of this research work and proposes possible future expansion.

# Chapter 2

## Literature Review of Shared-Aperture Phased Array Architectures

This chapter reviews relevant literature on shared-aperture phased arrays. It first introduces the concept and configurations of the shared-aperture arrays and then discusses the design challenges of the shared-aperture phased arrays. Next, the performance design merits are provided, followed by a review of selected papers with their advantages/limitations. Finally, the conclusion and the proposed configuration are summarized.

### 2.1 Background

Shared-Aperture (shared-aperture) arrays are multi-band antenna arrays whose elements are combined in a shared physical space either partially or fully [26]. They are sometimes referred to as interleaved arrays or co-aperture arrays. Shared-aperture arrays have the advantages of reduced size, weight, and power requirements compared to other independent multi-band configurations. Further, multiple radiation functions can be simultaneously implemented within the same aperture [27]. Moreover, with the recent developments in the Monolithic microwave integrated circuit (MMIC) industry, a single chip can monolithically integrate numerous Tx, and Rx units [15]. Consequently, it is demanded to integrate multiple antenna radiators within the same radiating aperture to align with the miniaturization trend [15]. Therefore, the interest in implementing shared-aperture platforms in

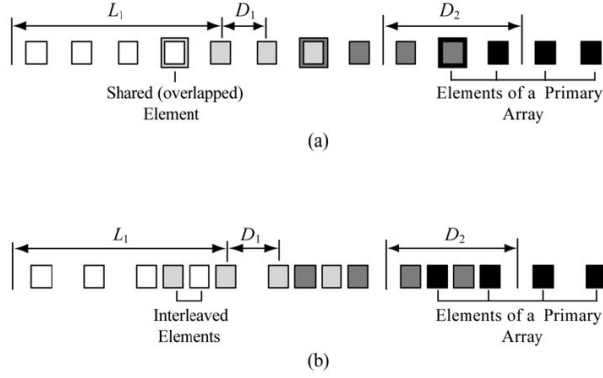


Figure 2.1: The two different realizations for co-aperture arrays [2]

active phased arrays has increased. Further, shared-aperture arrays can play an essential role in developing modular phased arrays.

The origin of the shared-aperture antenna arrays can be traced back to the 1970s when Hasio [28] presented an analysis of the multiple waveguides in a shared-aperture array configuration. Later, a dual-band shared-aperture array using waveguides with dipoles and the wideband tapered radiator was proposed in [29], and [30], respectively. Afterwards, most of the work reported in the literature focused on using planar structures to implement shared-aperture phased arrays.

## 2.2 Shared-Aperture Array Realization

Two main approaches are used for implementing a shared aperture array based on the array configuration, as presented in Fig. 2.1. In the first, the overlaid approach, one element is shared between two subarrays, each subarray belongs to a different frequency band [2] as shown in Fig.2.1. The shared element appears as a superimposed element belonging to two different subarrays [2]. Secondly, in the interleaved approach, some of the end elements of neighbouring subarrays share the aperture with that of another subarray, as shown in Fig. 2.1. Each element belongs to only one subarray.

Different configurations have also been reported in the literature for implementing the shared-aperture array:

## 2.2.1 Interlaced Configuration

The terms "nested," "interlaced," and "shared-aperture" are used interchangeably in literature to describe this configuration. Fig. 2.2 shows the concept for an interlaced array of different elements. In this configuration, the higher-band radiators are uniformly distributed, and the lower band ones are placed in the gaps between the higher-band elements. Each radiator represents a single frequency operation with a particular polarization [31]. There are no design limitations on the choice of higher-band radiator type. However, it is recommended that the lower-band element design be smaller to facilitate the interleaving process. In addition, the radiation pattern is greatly affected by the mutual coupling between elements in small antenna separation [32]. Hence, the lower-band element type and design are crucial for the efficient operation of the shared-aperture array.

The most used radiator types are the slot and the patch, whereas the most widely used radiator shapes are the strip-, ring- and cross-shaped. The Interlaced configuration was used in [31] to implement a shared aperture for C-band microstrip patches, and X-band printed slot elements. In [3], a feed for parabolic cylindrical reflector antenna, composed of  $K_u$ -/ $K_a$ -bands shared-aperture microstrip arrays are presented where the  $K_a$ -band single polarized microstrip patches are interlaced with the  $K_u$ -band dual-polarized microstrip slots. Nested Folded dipoles were used in [27]. Strip patches for lower-band elements are shared-aperture with patch antenna in [33], and dipoles shared with dipoles/(slots) are used in [34] [27] [35]. The shared-aperture slot with slot was used in [31]. Cross slot for the lower band is shared-aperture with patch in [3].

Since slots and dipoles require less space than patches, routing of the signal distribution circuit will be easier [31]. However, the burden on some applications' requirements, such as dual-polarization and higher bandwidth, requires multiple dielectric layers and a thicker profile, especially in the design of the lower-band elements. In addition, the slot array has the advantage that it does not contribute to spurious radiation since the signal distribution network is hidden behind it. However, its disadvantage is that a reflector ground plane is required because of its bidirectional nature [31]. In the case of shared-aperture patches, a higher dielectric constant is needed to make room for both patches, but this solution will decrease the bandwidth of the microstrip antenna. In addition, the radiation efficiency will decrease, and mutual coupling effects will be more substantial due to increased surface wave energy.

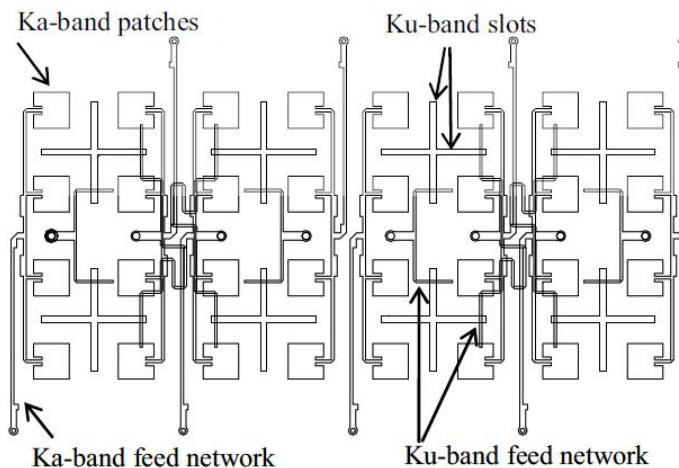


Figure 2.2: Shared-aperture dual-band interlaced array [3]

### 2.2.2 Perforated Configuration

Fig. 2.3 shows the concept of the perforated configuration of different elements. Perforations (windows) are made to place the layout of the higher frequency band radiator inside the structure of the lower frequency band element. This configuration can be considered a combination of the two main approaches previously stated in realizing a shared aperture array. Perforated configuration was initially proposed by Shafai [36] [36], where *C*-Band elements are arranged in the perforations of the lower *L*-Band radiators.

The perforated approach and its modified types of circular and perforated cross patch [37] were presented in the implementation of dual-band dual-polarized shared-aperture arrays in [36–38]. In [4], perforated microstrip patches are used for *X*-band operation where the parasitic patches of the *K<sub>a</sub>*-band are printed on the perforated area. In [36], a proximity-fed perforated *L*-band patch antenna and a 4×4 subarray of aperture-coupled patch antennas, placed in the perforated area, are presented.

The perforated-patch structure has the advantage of a lower profile than the other configurations. However, the design of the perforated configuration has some limitations compared to the others. The antenna bandwidth has an almost inverse relationship with the amount of perforation [39]. In addition, perforation in patches causes a high cross-polarization level. Further, the perforation on the lower band radiator and the frequency ratio between the lower and higher band frequency bands impact the ability to use the perforated configuration with any frequency ratio.

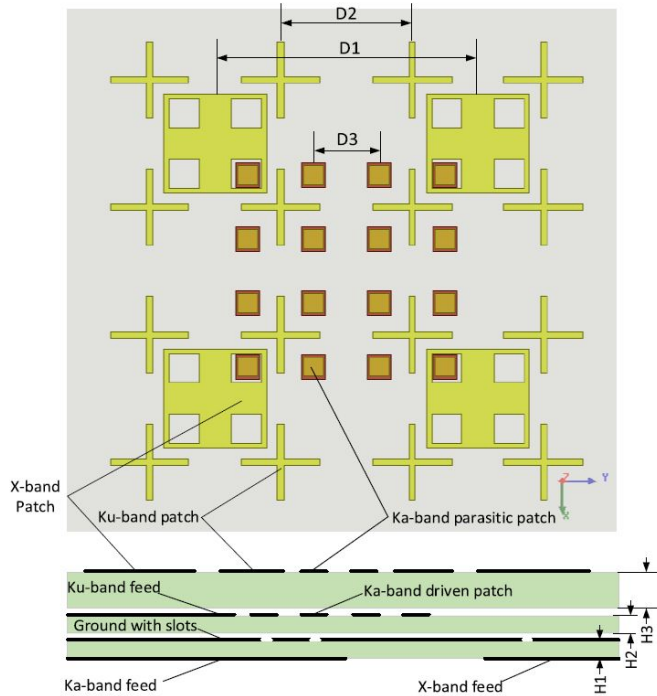


Figure 2.3: Shared-aperture dual-band perforated array [4]

### 2.2.3 Stacked Configuration

Fig. 2.4 shows the configuration of the stacked array [5], two radiators are placed on top of each other and separated by a dielectric layer. This configuration can be considered as an implementation of the overlaid realization approach. Usually, the lower-band radiator is placed below the higher-band radiator (i.e., in the bottom layer) to avoid the blockage of the radiation. The stacked configuration possesses the following advantages over the past configurations; the lower-band element is not confined by the space limitation of the perforation in the case of the perforated configuration, nor by the separation between the radiating elements in the case of the interlaced configuration. However, the stacked configuration increases the antenna's profile. In addition, a complex feeding network is required to achieve sound isolation between both radiators and low cross-polarization, mainly if the aperture coupling method is used for the feeding mechanism. Besides, the polarization characteristics are deteriorated due to the interaction between the stacked elements [39].

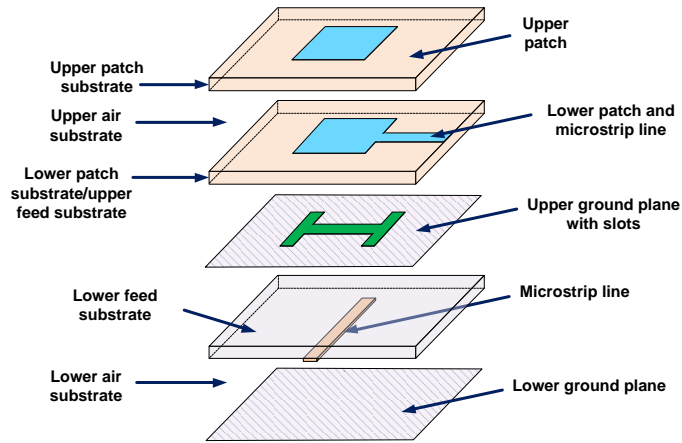


Figure 2.4: Configuration of the stacked dual-band element [5]

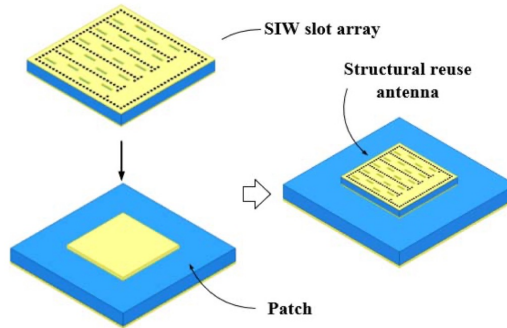


Figure 2.5: Configuration of the restructured antenna [6]

## 2.2.4 Restructured Configuration

Fig. 2.5 presents the concept of structure reuse implemented recently in multiple publications [6, 40], in which one of the radiators is re-functionalized partially or fully to fulfill another function at the other frequency band's operation. For example, a Ku-band array on a PCB is reused as the wall of a Ka-band rectangular waveguide antenna as in [40]. This configuration is mainly helpful for applications combining antennas with large frequency ratios, such as applications targeting the sub-6 GHz and the mm-wave band. In this context, a 3.5 GHz patch antenna serves as a slotted SIW array at 60 GHz in [6]. Despite the advantage offered by this configuration of high aperture efficiency, however, the overall size of the shared aperture is mainly large if used in low-frequency ratio applications. In this

case, the most implemented shared-aperture is 3-dimensional. Further, several supporting structures and suppressing interference structures such as frequency selective surface (FSS) are required to achieve the necessary isolation. Therefore, the designed structures are bulky, making them unsuitable for planar, low-profile targeted applications.

## 2.3 Design Challenges of Shared-Aperture Arrays

Several design challenges must be considered with the vast requirements for efficient, low-profile shared-aperture systems.

### 2.3.1 Mutual Coupling

Electromagnetic (EM) interference between channels is a significant obstacle, which leads to unwanted high cross-polarization and mutual coupling levels [27]. The amount of the mutual coupling between nearby radiators plays a critical role in the performance of the shared-aperture array, especially with antenna arrays of nearby frequency bands. Therefore, the low mutual coupling should be maintained between the antenna elements. In addition, one essential requirement is to design the lower and higher bands with a significant isolation level, similarly, with orthogonal polarization feeds in dual-polarized array systems.

### 2.3.2 Grating Lobes

The spacing between elements is confined by the necessary conditions to avoid the occurrence of grating lobes, especially when the array is allowed to scan [38]. Considering that different array element spacings are required for different frequencies, the shared-aperture array configuration proves to be convenient for dual-band array systems. Accordingly, less space will be necessary for the whole array implementation [38].

### 2.3.3 Level of Integration

The level of integration imposes stringent design requirements when it comes to the implementation of separate feed networks for each band [4]. The other challenging burden in the procedure is to place the multiple feed networks into a shared aperture in the case of a

dual-band dual-polarized array while maintaining high isolation. Owing to the limitations of the layout, a single substrate layer is required to feed two independent ports, either two polarizations or two frequencies [38]. Therefore, two substrate layers are at least needed for dual-polarization operation at two frequency bands [38]. Hence, meeting the isolation requirements will also be a challenge.

### 2.3.4 Frequency Ratio

One of the challenges of implementing a dual-band array is the frequency ratio. For low-frequency ratio arrays, the most reported work uses dual-band elements. Dual-band elements usually need a complicated feeding network; either complete separate feed networks are utilized for each frequency band, or a duplexer is used at the final stage to combine the two feeds into only one feeding port [41]. In addition, the mutual coupling between elements is unavoidable. Further, expanding the array imposes another challenge on the placement of the radiators in a way to cease the occurrence of grating lobes [41].

## 2.4 Figures of Merits in Phased-Array Design

The mm-wave systems' specifications push for increased antenna performance requirements. The designed shared-aperture array should support the ability to be extended to a more extensive array and to be manufactured in modular form. In addition, low profile, lightweight, and low cost are also critical features that should be considered in the design. A set of parameters is used to evaluate the performance of the shared-aperture array to compare the different configurations reported. These parameters and their definitions will be presented in this section.

### 2.4.1 Operating Frequency Band and Bandwidth

The frequency band of interest is  $K$ -/ $K_a$ -band for mm-wave phased array applications. The  $K_a$ -band is allocated between 26.5 and 40 GHz and conventionally covers a part of the K-band around 20 GHz [24]. The specified frequency intervals for both the downlink (Rx) are 17.7–21.2 GHz, and the uplink (Tx) frequency bands are 27.5–31 GHz [24]. Significant investment has been made in this band, which will offer significantly lower operating costs and, at the same time, produce a substantial increase in the available bandwidth. The antenna bandwidth indicated in this thesis is the impedance bandwidth ( $|S_{11}| \leq -10$  dB

). To fulfill the mm-wave systems requirement, the typical bandwidth in our application is 2-3 GHz.

### 2.4.2 Isolation between Frequency Bands

The isolation level between the ports of the dual or multi-band systems is important for realizing an efficient shared-aperture array. It represents the power coupled from one port to another port of the elements operating in different frequency bands. Most publications reported the isolation in the vicinity of 20 to 30 dB for shared -aperture in the X- and C-bands. Isolation between radiators is mainly affected by the mutual coupling between them. Nevertheless, achieving high isolation is challenging in mm-wave bands due to the near element separation [40] and the size of the commonly-used resonant-length-based radiators. In our thesis, the isolation level required is at least 50 dB. Isolation between orthogonal polarization is also an important condition for the operation of the dual-polarized antenna. In this case, the coupling between the orthogonally polarized ports should also be minimized. At least 25 dB of isolation will be required for dual-polarized antennas.

### 2.4.3 Cross-Polarization Level

The elements of the antenna array of any type can be excited with two independently orthogonal polarizations [42]. The cross-polarization (X-pol) is the polarization in a direction orthogonal to an intended state of polarization (Co-pol). The cross-polarization level is defined as the ratio of the X-polarized field component to the Co-polarized field component in the boresight direction. The cross-polarization level deteriorates for the phased array radar system as the main beam is scanned from the boresight direction, with its highest level in the diagonal planes [43]. Therefore, it is necessary to design a phased array antenna with sufficient cross-polarization isolation between the orthogonal antenna ports over the whole scanning angle [43]. In our thesis, the cross-polarization level is set to -25 dB.

## 2.5 Review of Recent Publications

This section will review recent publications on shared-aperture arrays. Table 2.1 lists some of the recent publications on shared-aperture arrays. The comparison focuses on the operating bands, bandwidth, isolation, cross-polarization, spacing between elements in the sub-array, and the sub-arrays ability to be expanded in modular form.

Table 2.1: Reported publication on shared aperture arrays

FOM	$f_0$ (GHz)	BW (GHz)	Polarization	Isolation (dB)	X-polarization (dB)	Element spacing/ $\lambda_0$	Modular
[41]	5.2/ 10	0.2/ 0.6	dual linear	-20/ -24	-24/ -26	0.42/ 0.8	no
[27]	1/ 2	-	linear	-20/ -17	-20/ -25	0.5/ 0.5	yes
[44]	20/ 30	1.7/2.2	linear	-	-20/ -20	0.5/ 0.53	yes
[4]	9.6/ 14.8/ 34.5	0.3/ 1/ 1.7	dual linear	-	-28/ -25/ -25	0.77/ 0.59/ 0.69	no
[45]	12.17/ 17.5	2.5/2.8	circular	-	-19 / -17	-	yes
[46]	9.6/37.7	0.6/4	linear	-22/-24	-20/-20	-	-
[47]	5.3/ 8.2	1.2/ 1.7	circular	-20/ -20	-20/ -20	0.84/ 0.65	yes
[48]	20/ 30	-	linear	-50	-	-	yes

In [41], a dual-polarized antenna for C-/X- bands are introduced, whereby a stub-loaded resonator is used to feed the stacked radiators. Multilayer technology is used in the implementation of the antenna. This configuration has the advantage of better isolation between the two frequency bands, but the top radiators block when the array is allowed to scan [49]. In addition, there is increased cost and complexity in manufacturing the multilayer structure, mainly when several units are used for larger arrays. Further, the separation chosen at the higher band is 0.8 of a wavelength, which implies that it would not prevent the occurrence of grating lobes in the case of scanning. It is also noticed that the elements exhibit quite a narrow band, which limits its operation to specific applications.

In [50] [27] [45], only one substrate layer is used for the implementation of the shared aperture. This has the advantage of achieving a low-profile array. However, since only one feed port is used for both radiators, the separation between radiators is not independently set. If kept at  $\lambda_o/2$  at the lower band frequency, the occurrence of grating lobes at the higher band will not be avoided. In contrast, the reverse can cause strong mutual coupling at the higher band elements and, indeed, will deteriorate the isolation performance of the dual-band array.

Inkjet printing technology is used in [27] on photographic paper as a low-cost, fast, and economical method since it uses no masks and reduces material waste [51]. It can also be used with various substrates, such as low-cost organic and polymer substrates [51]. In addition, the discovery of nanoparticle and nano-enabled inks has enabled inkjet-printing

technology to achieve narrow widths and spaces. However, this technology is bounded by the large dielectric and conductive losses, which limits its implementation in mm-wave [27]. Furthermore, the feasibility of implementation in large arrays is not possible due to the considerable mechanical warping [27]. Further, the array suffers from a high profile due to the inclusion of a ground plane, which is inserted at  $0.25 \lambda$  at 2 GHz below the substrate to improve the impedance bandwidth [27].

In [44], coaxial printed patch rings are introduced and interleaved in a triangular lattice. The simulation results were implemented by considering that only the central element of the array is connected, while the rest of the elements are terminated by  $50\Omega$ . This method doesn't indicate the performance of the shared-aperture array behaviour. The co-polar radiation patterns show broad beams through a hemispherical coverage [44]. However, the isolation between the Tx and Rx band was not reported, even though it is an essential parameter in declaring the effectiveness of the dual-band arrays. In addition, high cross-polarization at the Rx was reported to be due to the poor shielding of the outer conductor [44].

A shared-aperture supporting three frequency bands and dual-polarization is presented in [4]. The tri-bands are fulfilled using a perforated patch, stacked patch, and crosspatch radiators. Congestion in the radiation elements and feeding networks is noticed. Further, neither the isolation between the operating bands nor the cross-polarization level is reported. Last, the configuration is not suitable for modular operation. A dual-band dual-CP array proposed in [45] directly connects two microstrip patches that have different bands and polarization. The configuration is a new, low-cost implementation for shared aperture arrays. However, it cannot be applied to other bands of varying frequency ratios. Since the radiators at both frequencies are equally separated with the same value, this method would not be convenient in scanning arrays. In addition, placing the elements side by side increases the size of the collection. It may also affect the mutual coupling between radiators because of the slight separation between each other.

The interlaced configuration used in [46] implements a shared aperture array with cross-dipoles at the X-band and Ka-band patch antennas. Parasitic elements were used to enhance the bandwidth of the elements. Accordingly, the structure suffers from the congestion of the feeding network.

In [47] a C-/X-band shared aperture array is proposed for satellite communications. Circular polarization is implemented using a single-feed dual-coupling structure. The array achieves overall good performance. However, the performance of the sub-array in the dual-band operation is not reported.

A bandpass filter in [48] is integrated with a shared-aperture phased-array to achieve

a 50 dB isolation between the utilized bands. A more compact design can be achieved by using a multilayer PCB technology [48]. The idea of integrating a filter with the shared aperture is promising for reaching excellent isolation between the Tx and Rx bands. However, the integration effect on the radiation pattern, cross-polarization, and scan angle is not reported. In addition, the filter could increase the whole size of the integrated shared-aperture array. Furthermore, the narrowband nature of the filter would deteriorate the antenna's bandwidth.

## 2.6 Conclusion

Very few works have reported implementing a shared aperture array with reasonable isolation and wide-bandwidth operation while preserving low-profile features. Most of the publications rely on multilayer PCB technology to achieve wideband operation. However, this approach comes to the cost of complex structures and feeding circuits. Moreover, Few reported work targeted shared aperture array in  $K/K_a$ -band, with significant performance and suitable implementation for planar integration. At those bands, the separation between elements decreases, affecting the mutual coupling between the radiators and decreasing the isolation. Most implemented shared-aperture arrays rely on microstrip lines, which are not suitable for high-frequency applications. Moreover, the commonly used patch radiators suffer from narrow bandwidth operation and require thick substrates to achieve the required bandwidth.

# Chapter 3

## Shared Aperture DRA Arrays-Analysis

This chapter discusses the design aspects of the proposed shared-aperture phased array. First, it introduces the motivation for this thesis. Then, the methodology and steps of the design are explored. Finally, the proposed suggestions for mm-wave implementations are provided.

### 3.1 Introduction

This section addresses the motivation behind implementing shared-aperture arrays using dielectric resonator antennas (DRAs). First, implementing phased arrays, commonly with separate antenna platforms for uplink and downlink frequencies, are space-consuming. Accordingly, shared-aperture arrays can be considered an array miniaturization technique from the system point of view implementation. Therefore, it has the advantage of reducing the total aperture of multi-band phased arrays.

In addition, DRAs have attractive features such as their small size, high radiation efficiency, design flexibility, and large impedance bandwidth [52, 53]. The high efficiency is due to the reduced metallic loss and is a superior feature in high-frequency applications. In [54], the radiation efficiency of a DRA, operating at the  $K_a$ -band, is compared to that of a microstrip antenna, achieving a 15% higher value. Therefore, DRAs are a favourable alternative to metallic radiators such as microstrip antennas at millimetre wavelengths [53–57] for those unique features. In addition, the ability to achieve smaller element dimensions

using higher permittivity material is a design strategy that further increases design flexibility. Consequently, DRA fits well with the multi-requirements needed for shared-aperture arrays.

Finally, with the advances of additive manufacturing, commonly known as 3D printing, considerable performance advantages can be achieved in antenna manufacturing, such as fabricating complex geometries while satisfying the required size demands for specific requirements. In addition to developing antenna configurations that can not be easily manufactured with the conventional fabrication methods. However, little work has been done demonstrating such structures for high frequencies [58], and no published work has discussed the implementation of DRAs for shared-aperture configurations.

The initial specifications for the proof-of-concept prototype structure are summarized in Table 3.1.

Table 3.1: Required specifications for the proposed interleaved phased array

Specifications	$K$ -band	$K_a$ -band
Bandwidth (GHz)	2-3	2-3
Polarization	linear	linear
Cross-polarization (dB)	-25 dB	-25 dB
Isolation (dB)	-40 to -50 dB	-40 to -50 dB

This thesis presents the process of validating a proof-of-concept prototype of the shared-aperture array. The steps of the analysis introduced to demonstrate the validity of the new concept are illustrated in Fig. 3.1. The specific objective of the thesis is to investigate the features of the proposed shared-aperture array. The main goal is to embed the Tx and Rx antennas into the same aperture with minimum isolation between the two bands, analyze the factors that affect the performance of the shared-aperture array, and ultimately, for future work, implement a dual-polarized shared aperture phased array.

Based on the array configuration, the following criteria are perceived in investigating the competence of the proposed approach in developing a shared-aperture phased array with the prespecified requirements. Commonly, the grid or lattice shape directly affects the number of elements and the performance of the antenna array. In addition, the antenna elements' position and orientation have a significant effect on the radiation pattern of the antenna array. The distance between the antenna elements should fulfill the necessary conditions to avoid the occurrence of grating lobes. Moreover, the effect of the mutual coupling between the radiators should be considered. Finally, an important step is to evaluate the near field interaction between array elements at different frequency bands

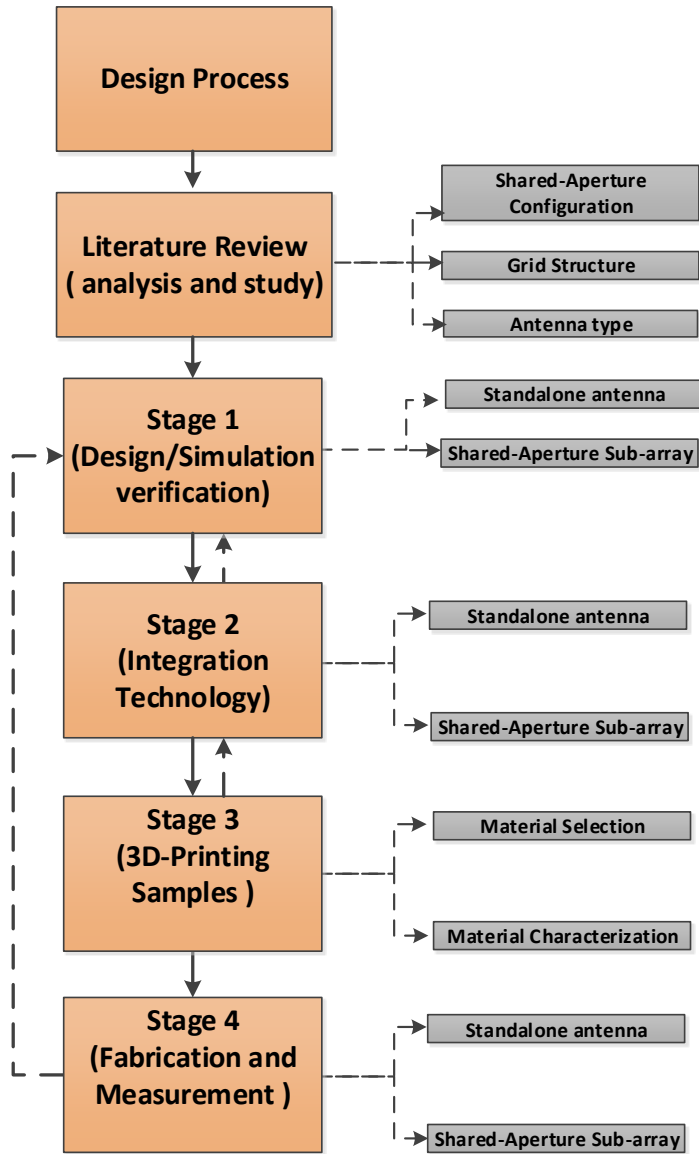


Figure 3.1: Shared-aperture design procedure

to determine the most convenient way to enhance the shared-aperture array’s radiation characteristics.

Regarding the antenna element, DRA is identified as the convenient antenna type for mm-wave applications. The work begins with the conventional approach for designing DRAs, selecting a DRA from the standard used shapes and calculating the DRA dimensions for the specified frequency band using analytical and computational electromagnetic simulators. Afterwards, modifications to the design can be applied for specific required features, such as dual polarizing ability, larger bandwidth, and smaller footprint.

The following section will present a brief review of the DRAs. Next, the design procedures of the antenna element and the sub-array are shown in the subsequent sections.

## 3.2 Dielectric Resonator Antennas (DRAs)

DRA has attracted researchers since first proposed by Long [59] as a promising radiator. Since then, DRAs have been used in various applications [60–62]. DRAs operate by exciting the proper electromagnetic mode inside the resonator. For the electromagnetic wave to radiate from the resonator, the relative permittivity should be between 5 and 30 [63]. The most commonly studied shapes of the resonator are rectangular [52], cylindrical [59], and hemispherical [64]. Rectangular shaped DRA has a lot of advantages over cylindrical and hemispherical shaped DRAs. Characterized by three degrees of freedom, rectangular DRAs feature considerable design flexibility compared to other shapes. This is deemed useful when a required profile is one of the design constraints. Further, the DRA dimensions and the selected dielectric constant control the desired bandwidth at a given resonant frequency. Cylindrical DRAs (CDRAs) were first reported by Long [59], and afterwards, CDRAs have probably been the most used DRA in several applications. Other DRA shapes are reported in the literature to provide enhanced performance to the standard shaped DRAs such as bowtie [65], stacked [66], and staired pyramid DRAs [67].

DRA can be excited by the same methods of excitation used for conventional patch antenna [63]. The most frequent way of excitation is aperture coupling. This method is the easiest to carry out, especially at mm-wave [67]. Moreover, DRA, aperture-fed by substrate integrated waveguide (SIW), provides highly-efficient radiators in mm-wave applications [53, 68–70].

DRAs can be analyzed analytically using the magnetic wall model [63]. This model represents the DRA’s dielectric-air surfaces by perfect magnetic conductors (PMC) walls. Therefore, the eigenmode problem can be used to solve for modes of the dielectric cavity.

Afterwards, the resonant frequencies and field distributions of the individual modes can be obtained by solving the eigenmodes of the dielectric cavity. After that, the magnetic currents on the surface are calculated. Then, the far-field transformation method is used to obtain the corresponding radiation pattern of each radiating mode. The magnetic wall approach does not consider radiation losses in the analysis. Accordingly, it is an approximate method for getting a good first approximation of the required results.

A DRA can support an infinite number of resonant modes. The excited modes of the DRA depend on the material properties, the operating frequency, and the dimensions and shape of the resonator. Two excited modes can be found in the cylindrical-shaped DRA: the transverse magnetic mode  $TM_{01\delta}$  (defined as well as  $TM_{011}$ ), whose radiation pattern resembles that of a vertical electric dipole and the hybrid electromagnetic mode  $HEM_{11\delta}$  (defined as well as  $HEM_{111}$ ), with a radiation pattern like that of horizontal magnetic dipole [61], [63]. In rectangular DRA, similar excited modes with equivalent radiation patterns are obtained [61]. DRAs are considered a convenient, efficient candidate for phased arrays at mm-wave applications. However, no DRA array design has been proposed for shared-aperture phased arrays.

### 3.3 DRA Shared-Aperture Array Configuration

The proposed implementation for the DRAs shared-aperture array's study is presented in Fig. 3.2. The interlaced (interleaved) configuration is chosen to allow the higher and lower bands antenna elements to be designed independently, which provides more design flexibility. In addition, with the development of the multifunctional Tx/Rx MMIC, where each module includes multiple transmit (Tx) and receive (Rx) channels integrated on the same chip, the interlaced proves to be a promising platform for future implementation of active phased arrays. To validate the proposed configuration, a sub-array design was adapted first to help understand the mechanism of the interleaved  $K$ -/ $K_a$ - DRA array's operation. After completing this part, the sub-array will be extended to the complete array configuration.

### 3.4 Antenna Design

Antenna element selection and design are crucial in implementing the shared-aperture array. The radiating element performance determines some array specifications, such as the bandwidth and the cross-polarization level.

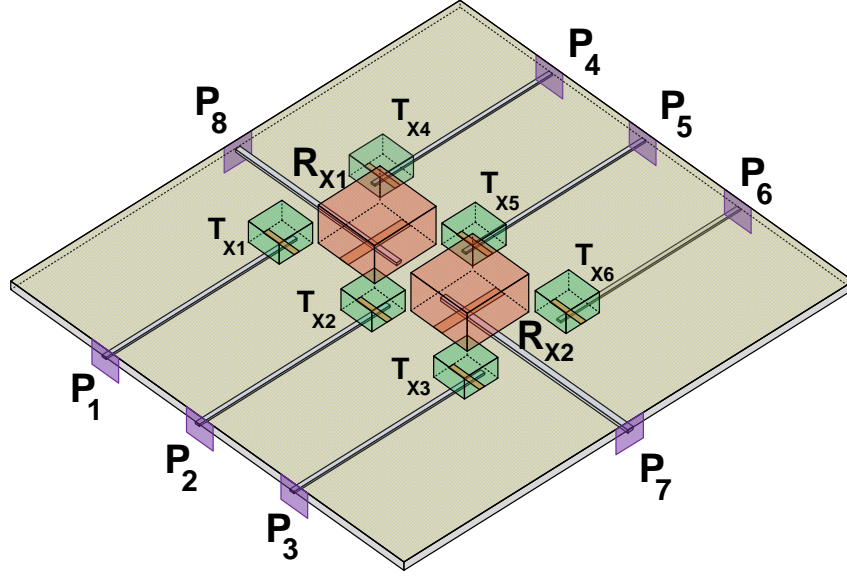


Figure 3.2: Proposed shared-aperture array configuration

For the higher-band radiator in the dual-band shared-aperture array, a broad bandwidth with a compact structure is preferred to allow more space for interlacing the lower-band elements. On the other hand, a minimum footprint is required for the lower-band radiators to reduce the coupling between antenna elements. The lower band element thickness will determine the array's profile.

Numerous DRA basic designs exist in the literature; rectangular DRA and cylindrical DRA are chosen for our study and the implementation of our novel shared-aperture array. In our proposed designs, Rogers *RT/ Duroid 6010LM* with the relative permittivity ( $\epsilon_r$ ) 10.2 is used as the material of the DRA, and Rogers *RO4360G2* with relative permittivity ( $\epsilon_r$ ) 6.15 is used as the substrate material in the feeding structure design.

For simplicity, the DRA is excited by the aperture coupled method. The aperture is equivalent to a magnetic current source, oriented along the slot, exciting the field inside the DRA. The geometry of the aperture-fed DRA is shown in Fig. 3.3. Aperture coupling is advantageous in mm-wave as it isolates the radiating aperture from any spurious radiation or coupling from the feed circuit. The antenna consists of a substrate on which the ground plane is mounted, where the microstrip feed lines are located at the bottom of the substrate, and a slot is etched on the ground plane. The DRA is mounted on the top of the ground. The following section presents the simulation results for the  $K$ -/ $K_a$ - band elements designed using the previously mentioned shapes.

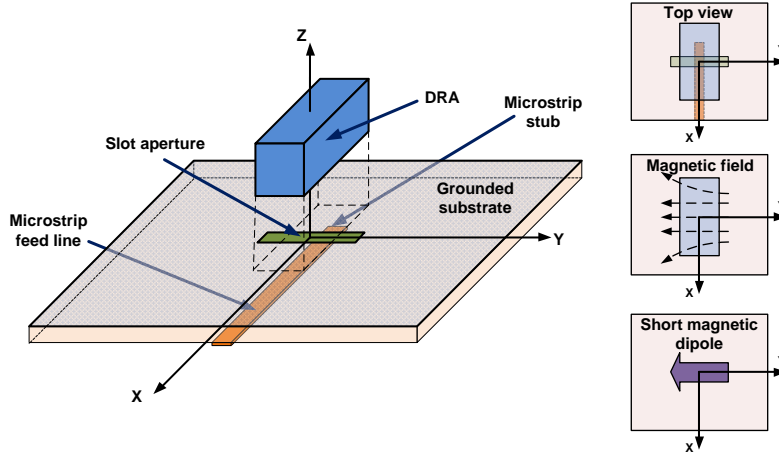


Figure 3.3: Aperture-fed DRA configuration

### 3.4.1 Rectangular DRA

In isolated rectangular DRA, the various excited modes are the  $TE$  and  $TM$  modes, whereas only the  $TE$  modes are excited for DRAs positioned on the ground plane. The rectangular DRA's  $TE$  modes resemble the magnetic dipole radiation and are oriented toward one of the rectangular axes ( $TE_x$ ,  $TE_y$  and  $TE_z$ ). The resonant frequency of  $TE$  modes can be calculated by solving the transcendental equation [52, 61], and is a function of the DRA dimensions. Accurately choosing those dimensions ensures that the undesired modes are suppressed within the desired operating frequency band.

Fig. 3.4 shows the configuration of the designed rectangular DRA. The antenna parameters are listed in the caption. The thickness of the DRA is chosen based on the commercially available standard heights. The power is coupled into the DRA through a narrow slot of length  $L_{slot}$ , and width  $W_{slot}$ , which is excited by a microstrip feed line of stub length  $l_{stub}$  and width  $W_{stub}$ . The dimensions of the DRA should be chosen to excite the correct fundamental mode for radiation. The design procedure is described briefly. The Rx and Tx DRAs are designed to resonate around the  $K$ - and  $K_a$ - band, respectively. The resonant frequency of the DRA is calculated theoretically using the formulas in [52, 61] and verified with the Eigenmode solution using the Ansoft HFSS simulator. The slot length is initially set to half the guided wavelength, and the width is fixed to a  $0.1 \times$  slot length. Parametric analysis is performed for all antenna parameters to obtain a reflection coeffi-

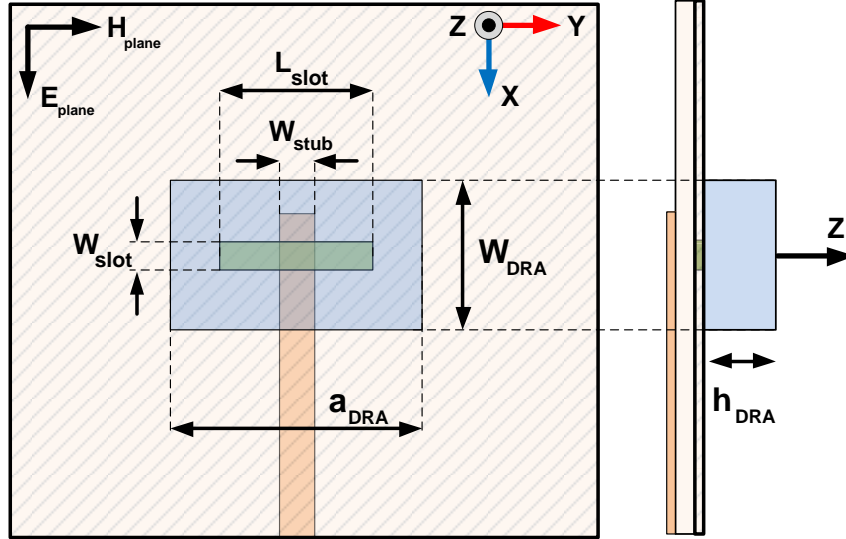


Figure 3.4: Cross-section of the aperture fed rectangular DRA

cient below -10 dB over the required band. The mode excited in the DRA is the  $TE_{11\delta}$  mode. This analysis used two configurations for the DRAs: square and rectangular. The square DRA is employed to extend the implementation to a dual-linearly polarized radiator for the next stage of the  $K$ -/ $K_a$ - dual-polarized shared-aperture array. In addition, the rectangular DRA requires less space, making it more suitable as more room will be available to interlace the lower-band elements. The calculated dimensions of the designed  $K$  and  $K_a$ - band DRAs are listed in Table 3.2.

## Simulation Results

This section presents the simulation results of only the square configuration of the  $K$ - and  $K_a$ - band DRAs. The full-wave electromagnetic (EM) simulations have been performed using HFSS [71].

Fig. 3.5a shows the simulated reflection coefficient and the radiated power for the designed DRA antenna at the  $K$ -band. The reflection coefficient is below -10 dB over the band from 18.2 GHz to 20.5 GHz. The efficiency at 19.4 GHz for the single element is 97.5 %. Figure 3.5b shows the simulated reflection coefficient and the radiated power for the designed DRA antenna at the  $K_a$ -band. The reflection coefficient is below -10 dB over the band from 28.3 GHz to 31.4 GHz. The efficiency at 29.7 GHz for the single element is 98

Table 3.2: DRA elements dimensions

Band	$f_R$ (GHz)	Config.	$a_{DRA}$ (mm)	$w_{DRA}$ (mm)	$h_{DRA}$ (mm)	$L_{slot}$ (mm)	$W_{slot}$ (mm)	$W_{stub}$ (mm)
$K_a$	29.7	Square	2.9	2.9	1.27	2.7	0.2	0.3
$K$	19.2	Square	3.8	3.8	1.9	5	0.2	0.3
$K_a$	32.12	Rect.	3	1.5	1.27	2.4	0.2	0.3
$K$	20.9	Rect.	5	2	1.9	1.9	3.5	0.3

%.

Fig. 3.7a and Fig. 3.7b present the H and E-plane gain patterns of the designed DRA antennas at the  $K$ - and  $K_a$ -band respectively. The cross-polarization levels at the boresight are less than 40 dB and 50 dB in both E- and H- planes, for the  $K$ - and  $K_a$ -band antennas, respectively.

Fig. 3.8a and Fig. 3.8b show the electric field's vector plot distribution inside the the  $K$ - and  $K_a$ -band DRAs, respectively. The E-field confirms the excitation of the correct mode of radiation inside the DRAs. These results show that the dominant  $TE_{11\delta}$  mode is excited in both radiators.

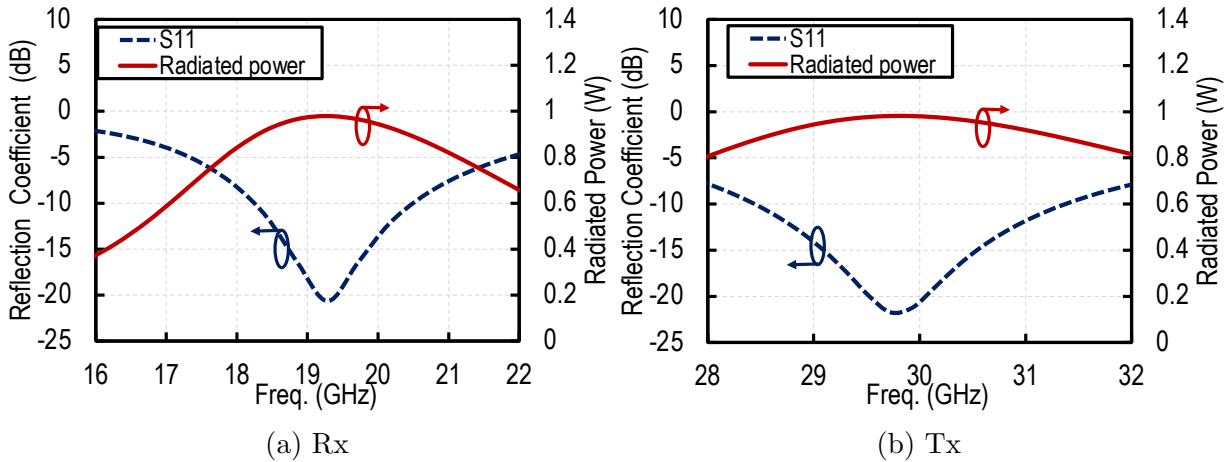
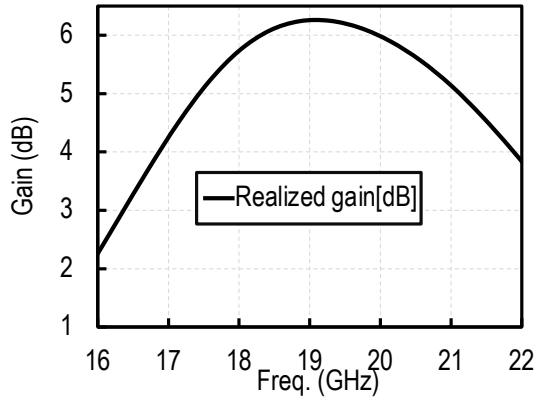
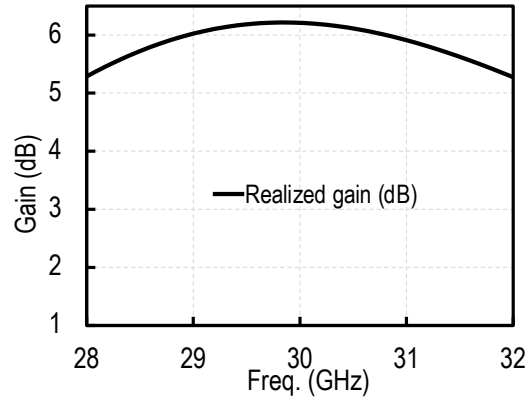


Figure 3.5: Reflection coefficient and radiated power of the square DRA (a)Rx (b)Tx

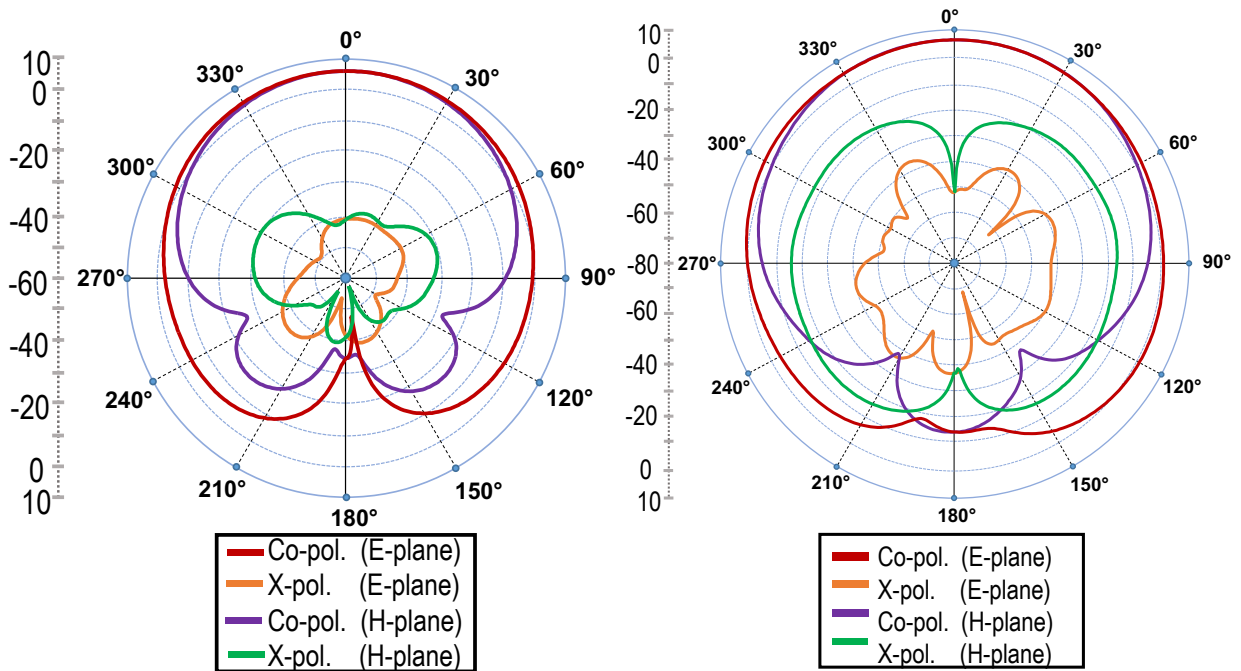


(a) Rx



(b) Tx

Figure 3.6: Realized gain of the square DRA (a)Rx (b)Tx



(a) Rx

(b) Tx

Figure 3.7: Radiation pattern gain of the square DRA

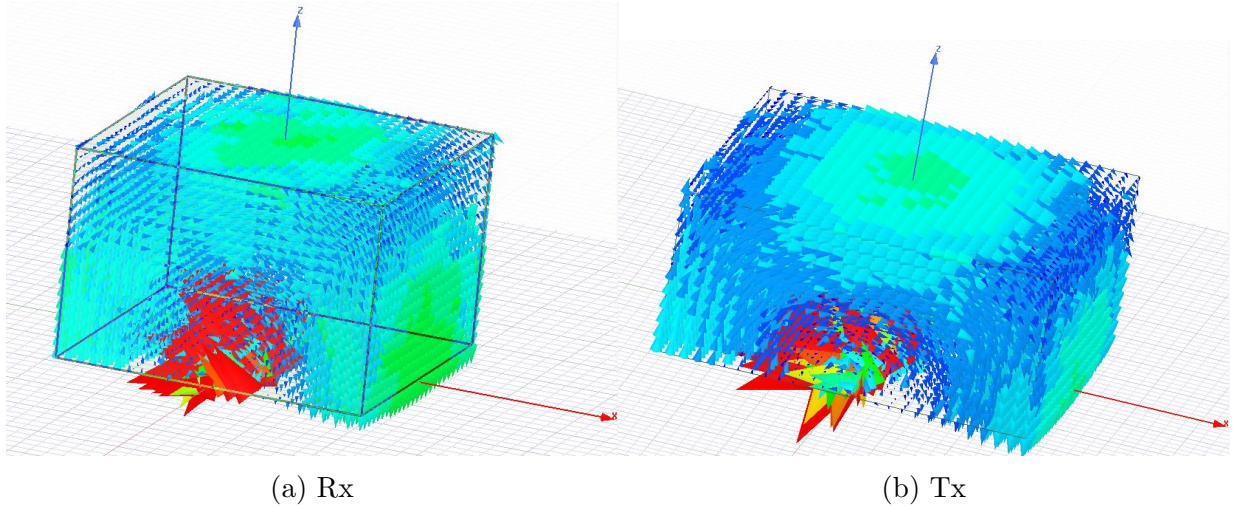


Figure 3.8: Electric Field Distribution of the square DRA(V/m)

### 3.4.2 Cylindrical DRA Design Procedure

In a cylindrical DRA mounted on a ground plane, the hybrid electromagnetic mode  $HEM_{11\delta}$  is the first excited radiating mode with the lowest resonant frequency [59] [72]. It radiates broadside radiation patterns in both (E-and H-) planes, corresponding to those of microstrip patch antenna (i.e., a short horizontal magnetic dipole).

Fig. 3.9 shows the configuration of the aperture coupled cylindrical DRA. The antenna parameters are listed in the caption. The mode excited in the DRA is the  $HEM_{11\delta}$  mode. According to the design procedure used, the Rx and Tx DRAs are designed to resonate over  $K$ -/ $K_a$ - band. The resonant frequency of the supported modes by the cylindrical DRA is calculated using the general resonance formula for modes given in [63] [72], and verified with the Eigenmode solver using the HFSS simulator [71]. This method provides a reasonable initial approximation of dimensions that is further tuned. A parametric study using HFSS is conducted to achieve the minimum possible footprint by considering different diameter to height ratios (i.e., aspect ratio). The dimensions of the designed  $K$ -/ $K_a$ - band cylindrical DRAs are listed in table 3.3

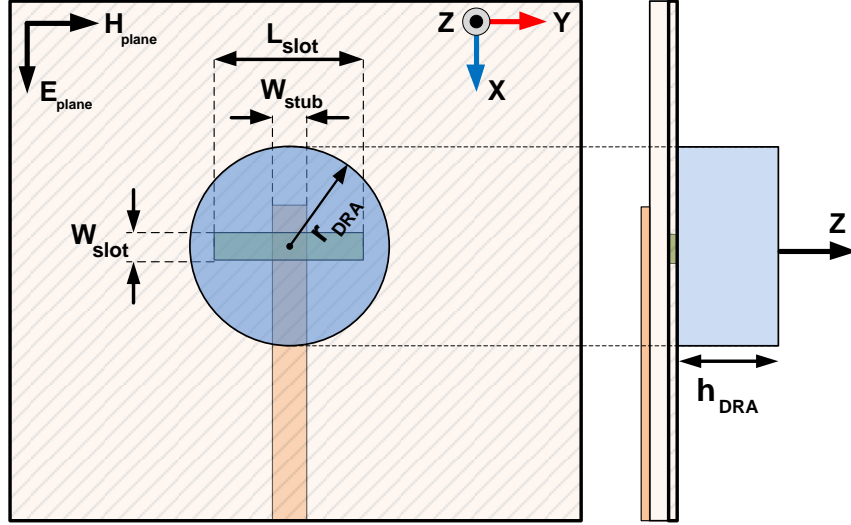


Figure 3.9: Cross-section of the cylindrical DRA

Table 3.3: DRA elements dimensions

Band	$f_R$ [GHz]	$r_{DRA}$ (mm)	$h_{DRA}$ (mm)	$L_{slot}$	$W_{slot}$	$W_{stub}$
$K_a$	29.7	2.9	1.27	2.7	0.2	0.3
K	19.2	3.8	1.9	5	0.2	0.3

## Simulation Results

Simulation results of the cylindrical configuration of the  $K$ - and  $K_a$ - band DRAs will be presented in this section.

Fig. 3.10a shows the simulated reflection coefficients and the radiated power for the designed cylindrical DRA antennas at the  $K$ -band. The reflection coefficient is below -10 dB over the band from 20 GHz to 23 GHz. The efficiency at 21.4 GHz for the single element is 98.8 %. Fig. 3.10b presents the simulated reflection coefficients and the radiated power for the designed DRA antennas at the  $K_a$ -band. The reflection coefficient is below -10 dB over the band from 28 GHz to 30.5 GHz. The efficiency at 29.4 GHz for the single element is 95 %.

Fig. 3.11a and Fig. 3.11b present the H- and E-plane gain patterns of the designed cylindrical DRA antennas at the  $K$ - and  $K_a$ -bands, respectively. The cross-polarization levels at the boresight direction are less than 50 dB and 40 dB in both H- and E- planes

for the  $K$ - and  $K_a$ -bands, respectively.

Fig. 3.12a and Fig. 3.12b show the electric field's plots distribution inside the  $K$ - and  $K_a$ -bands DRAs, respectively. The E-field forms a loop inside the dielectric resonators. These results show the excitation of the dominant  $HEM_{11\delta}$  mode in both radiators.

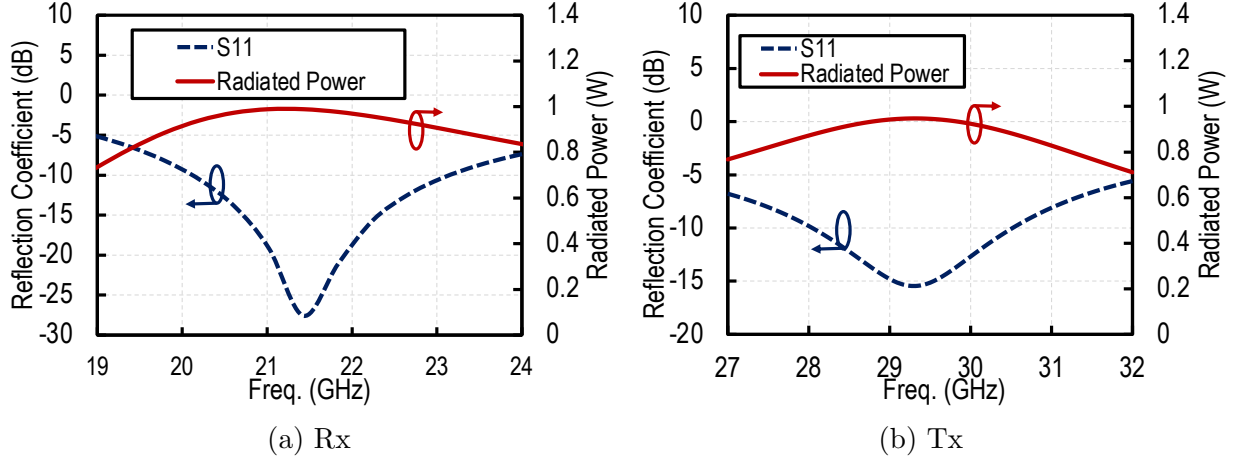


Figure 3.10: Reflection coefficient and radiated power of cylindrical DRA (a)TX (b)RX

### 3.5 Sub-array Configuration

The configuration of the sub-array (i.e., array lattice) is a principal determining factor of the radiation performance of phased array [44]. First, the antenna element location controls the occurrence of the grating lobes within the required scanning range [44]. In addition, the array lattice shape maintains the maximum number of antennas in a given radiating aperture [44]. Consequently, the required number of the Tx and Rx RF chains will be determined. Finally, the inter-element spacing is critical as it affects the mutual coupling between the elements.

Different grid lattices have been introduced in the literature. Rectangular and triangular element distributions are the most commonly used configurations for larger arrays and are analyzed for shared-aperture configurations in [44]. In [44], the number of required

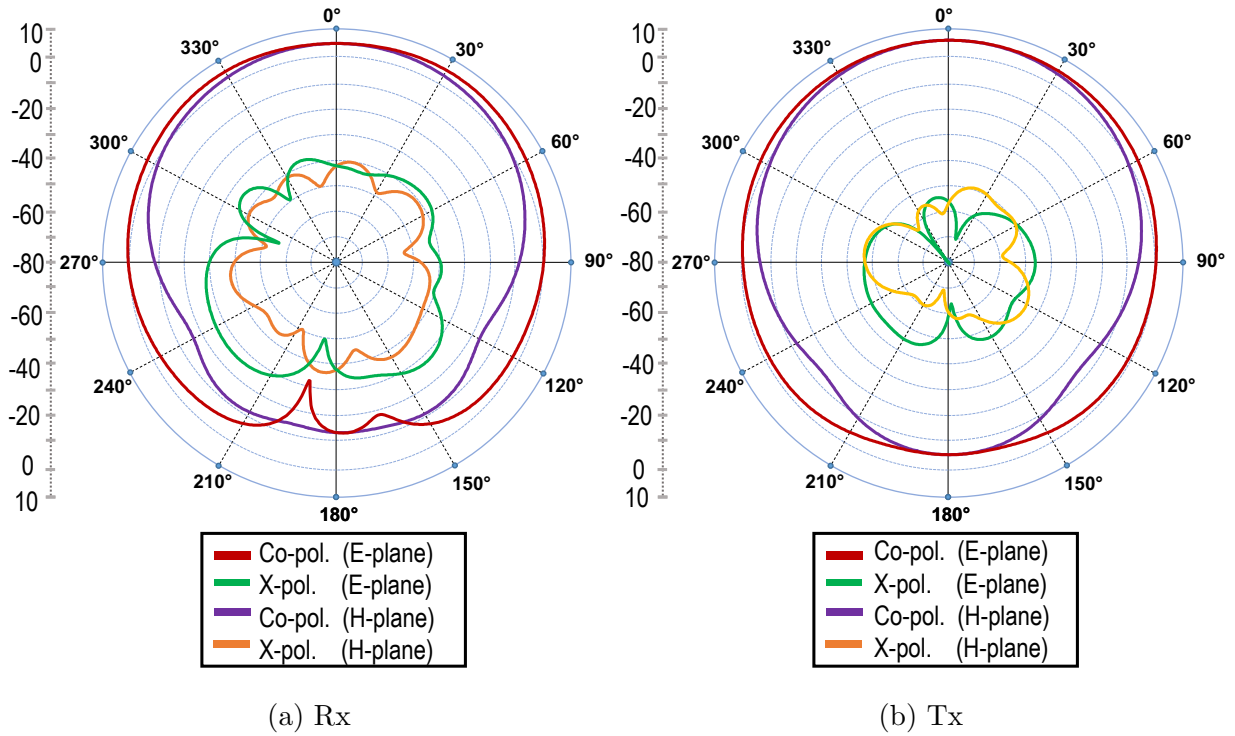


Figure 3.11: Radiation pattern gain of the cylindrical DRA

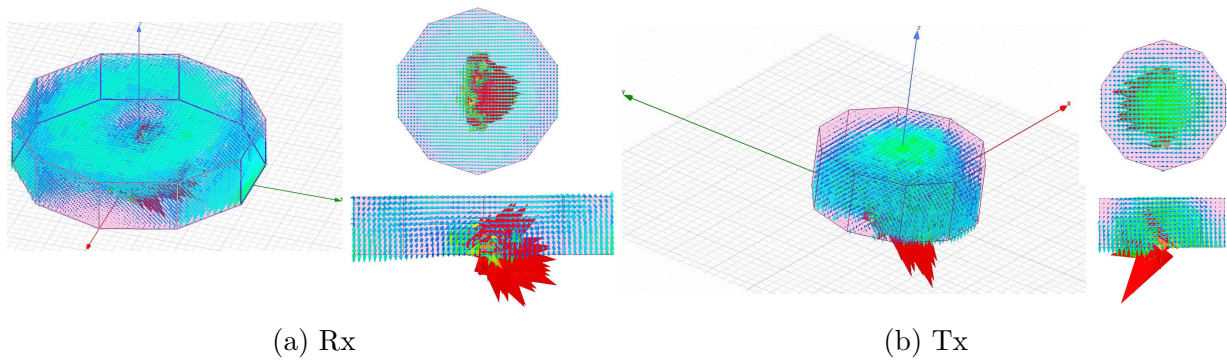


Figure 3.12: Electric Field Distribution of the cylindrical DRA

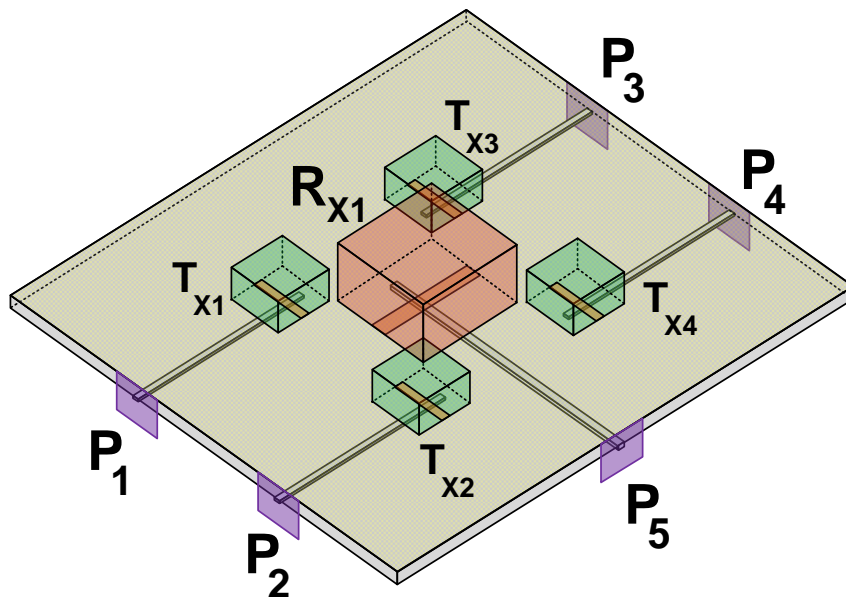


Figure 3.13:  $K$ -/ $K_a$ -band sub-array configuration

radiators is minimized by 13 % upon using a triangular lattice instead of the rectangular one [44]; however, this configuration involves the superimposition of some Tx and Rx array' elements. Consequently, a complex feeding network will be required for the superimposed elements. In addition, superimposed antennas suffer from high cross-polarization. Therefore, the rectangular lattice is more compatible with the design of the  $K$ -/ $K_a$ -band shared-aperture array to control the radiators at both bands independently. Accordingly, the  $K$ -band elements will be interlaced within the  $K_a$ -band elements.

Since the  $K$ -band elements will be interlaced within the  $K_a$ -band elements, the  $K$ -band element design is restricted to that of the  $K_a$ -band element cell in terms of the scan range. The unit cell consists of four  $K_a$ -band DRAs and one  $K$ -band DRA interlaced in the middle of the sub-array, and both the  $K$ -/ $K_a$ - DRAs are excited by the aperture-coupled feeding method as illustrated in Fig. 3.13.

### Simulation Results

This section will present the simulation results of the shared aperture  $K$ - and  $K_a$ -band sub-array lattice. Both the curves for the reflection coefficients of the DRAs ( $S_{ii}$ ) and the coupling coefficient between the Tx and Rx DRAs ( $S_{ij}$ ) are shown in Fig. 3.14. The RX

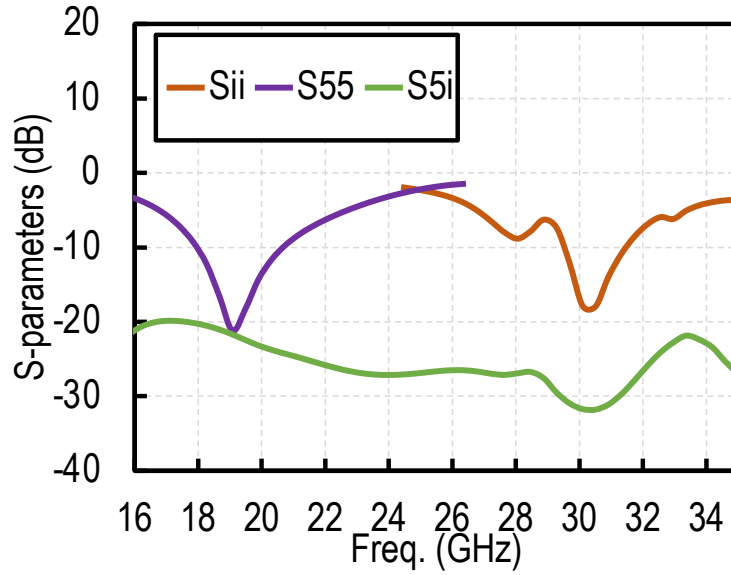


Figure 3.14: The simulated reflection/coupling coefficient and radiated power of the interleaved sub-array

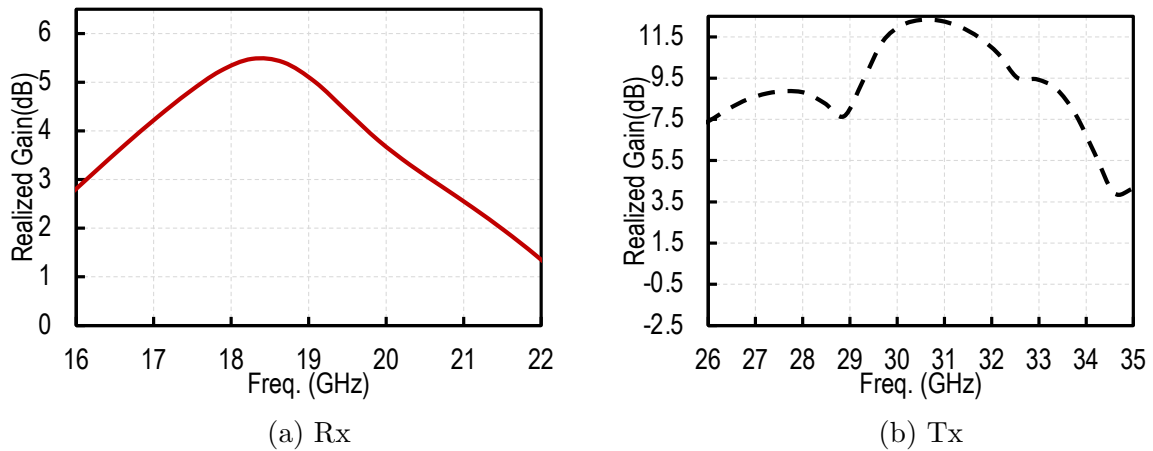


Figure 3.15: The simulated realized gain of the sub-array. a)Rx b)Tx

DRA's simulated 10-dB reflection coefficient bandwidth is at least 2.5 GHz from 18 GHz up to 20.5 GHz, with a maximum return loss of -21 dB at 19 GHz, i.e. covers almost 13%. The TX-band array's simulated 10-dB reflection coefficient bandwidth is 2 GHz, between 29.5 GHz up to 31.5 GHz, with a maximum return loss of -18 dB at 30.5 GHz, i.e. covers almost 6%. The isolation reaches 32 dB between the Tx and Rx DRAs at the Tx band. Fig. 3.15 shows the simulated realized gain for the Rx array and the Tx antenna at the  $K$ - and  $K_a$ -band, respectively. The simulated gains are 5.5 dBi at 18.2 GHz and 12.3 dBi at 30.5 GHz.

Fig. 3.16a and Fig. 3.16b depict the simulated radiation patterns of the shared aperture sub-array in the XZ- and YZ-planes, simulated at the reflection coefficient minima of the return loss patterns, at the  $K$ - and  $K_a$ -band, respectively. The cross-polarization level is lower than the simulated co-polarization level at the bore-sight direction in both planes by 50 dB at the Rx-band and 45 dB at the Tx-band. It can be noticed that symmetric patterns and almost low cross-polarization are obtained because of the symmetry.

The proposed design confirms that the proposed sub-array can simultaneously operate in the determined frequency bands with good performances, as illustrated in the simulation results, with a good reflection coefficient at the  $K$ -/ $K_a$ -bands and good cross-polarization is achieved for both the Tx- and Rx- array.

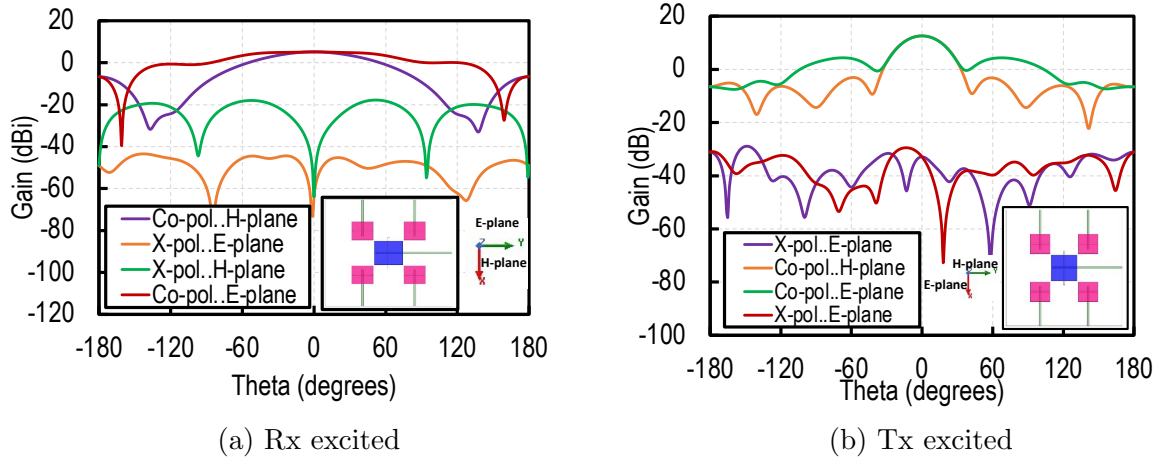


Figure 3.16: The radiation characteristics of the shared-aperture sub-array

## 3.6 Shared-Array Configuration

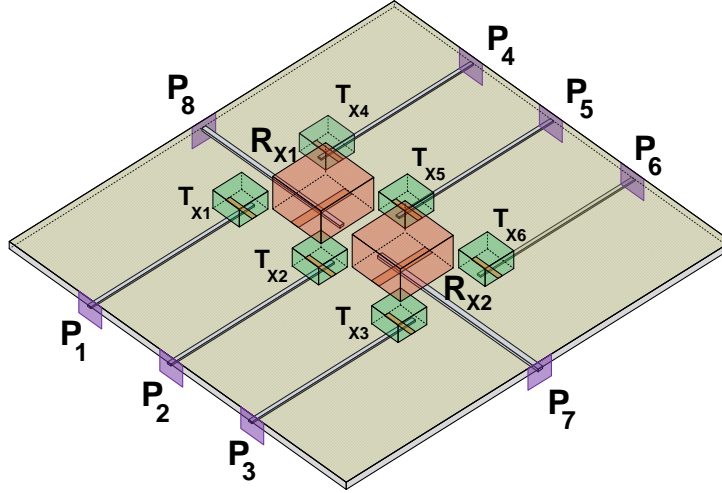


Figure 3.17: Full shared-array configuration

A larger array is designed by combining two sub-arrays as illustrated in Fig 3.17. The idea of this construction is to validate the design methodology by repeating multiple sub-arrays; two sub-arrays are combined to form a  $K$ -/ $K_a$ - band shared-aperture array with six  $K_a$ - band DRAs as the Tx-array and two  $K$ -band DRAs as the Rx-array.

### 3.6.1 Simulation Results

Both the curves for the reflection coefficients of the DRAs ( $S_{ii}$ ) and the coupling coefficient between the Tx and Rx DRAs ( $S_{ij}$ ) are shown in Fig. 3.18. The simulated 10-dB return-loss bandwidth of the Rx DRA is at least from 18.2 GHz up to 20.5 GHz, with a maximum return loss of 21 dB at 19 GHz (i.e., covers almost 12%). The simulated 10-dB return-loss bandwidth of the Tx DRA is between 29.5 GHz up to 31.8 GHz, with a maximum return loss of 16 dB at 30.3 GHz ( i.e., covers almost 7.5%). The isolation ranges from 29 dB to 37 dB between the Rx and Tx DRAs. Fig.3.19 shows the simulated realized gain for the Tx array and the Rx array at the  $K_a$ - and  $K$ -band, respectively. The simulated gains are 9.3 dBi at 19.2 GHz and 12.2 dBi at 30.8 GHz.

Fig. 3.20b and Fig. 3.20a depict the simulated radiation patterns of the full shared array in the XZ- and YZ- planes, simulated at the reflection coefficient minima of the return

loss patterns, at the  $K_a$ - and  $K$ - band, respectively. The cross-polarization level is lower than the simulated co-polarization level at the bore-sight direction in both planes by 58 dB at both the Rx-band and the Tx-band. It can be noticed that excellent cross-polarization is obtained.

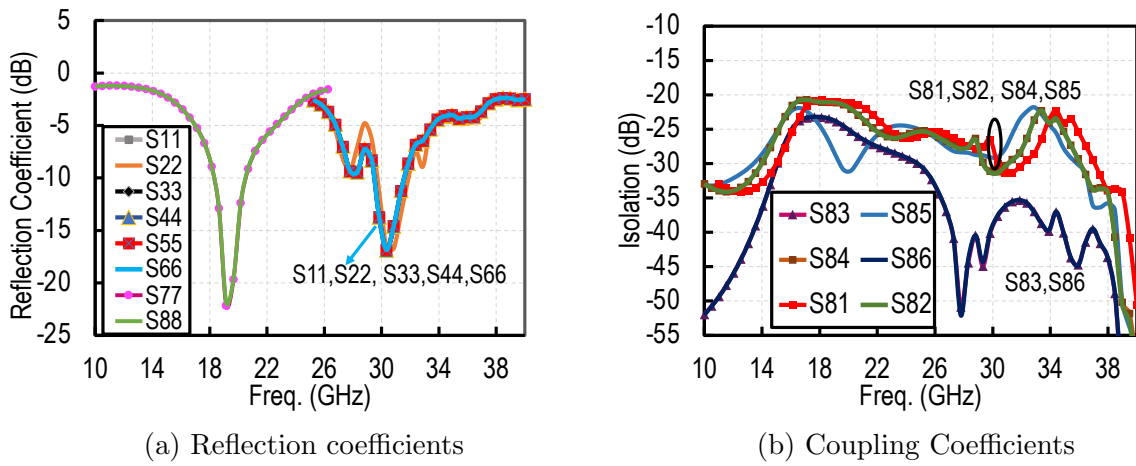


Figure 3.18: The Reflection/coupling coefficients of the shared-aperture array

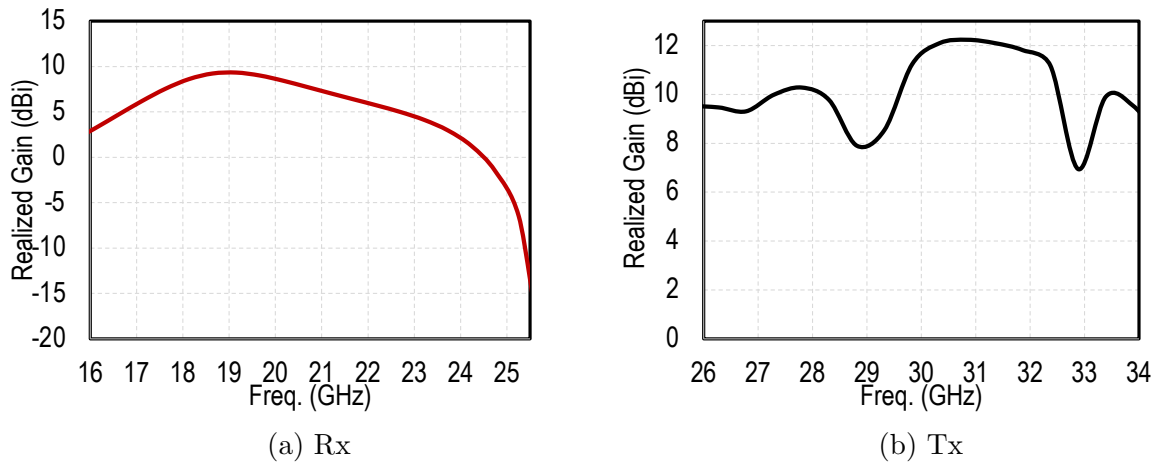


Figure 3.19: The realized gain of the shared-aperture array a)Rx b)Tx

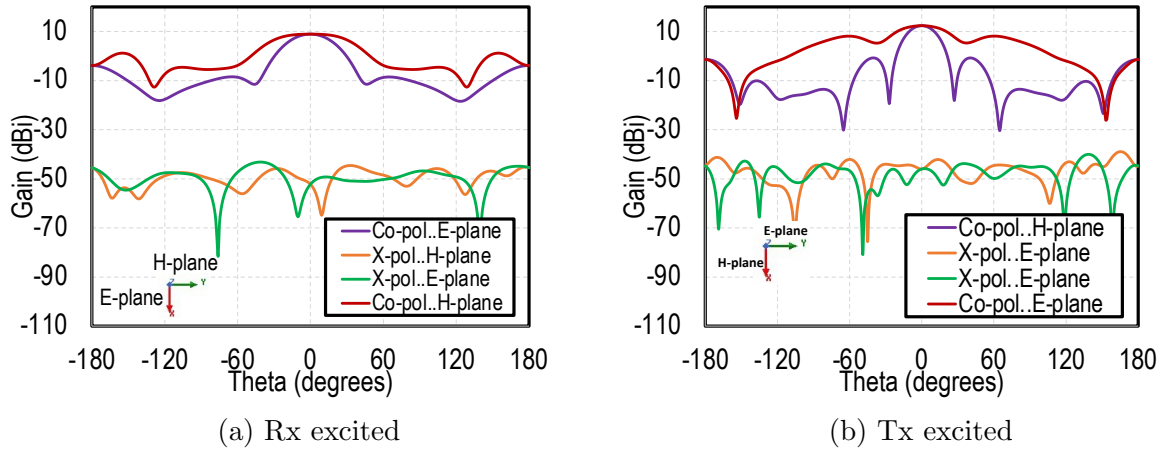


Figure 3.20: The radiation characteristics of the shared-aperture array a)Rx b)Tx

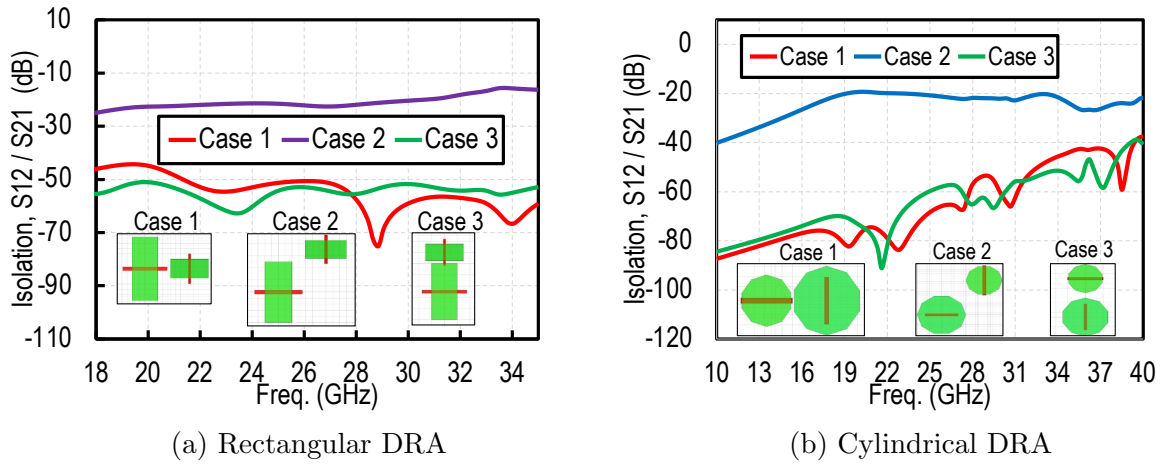


Figure 3.21: The isolation between The TX and RX DRAs

### 3.7 Isolation Analysis

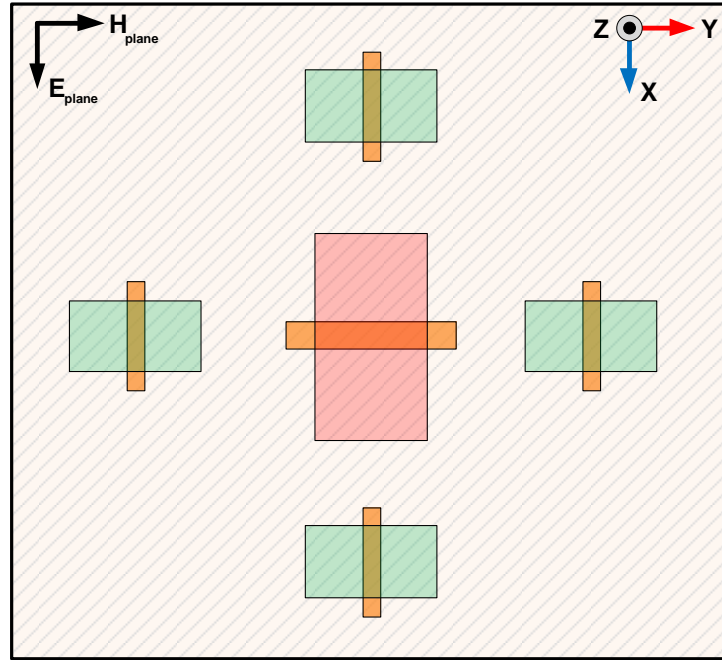
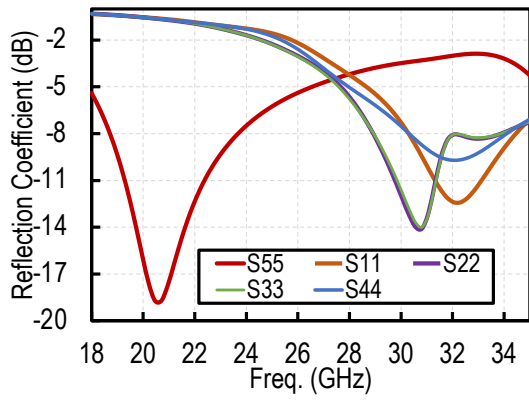


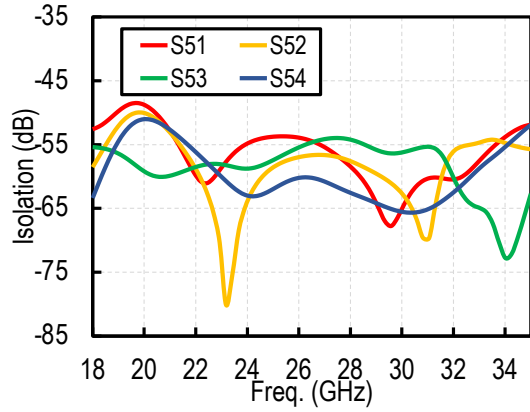
Figure 3.22: Sub-array configuration

The approach used to investigate the isolation improvement is to study the effect of the orientation of both the Tx and Rx radiators on the isolation level. This study was performed using rectangular and cylindrical DRAs, previously stated at the beginning of the chapter. The orientation of both the Tx and Rx DRAs are allowed to form a T-shaped configuration, where the Tx and Rx slots are placed perpendicular to each other in the E-plane and H-plane, respectively. The T-shaped configuration is compared to the interlaced diagonal configuration conducted earlier. A significant improvement in the isolation level was realized, compared to the previous arrangement as shown in Fig.3.21 in both planes. The enhancement in isolation level is at least 30 dB more than the value achieved in the previous configuration at the Tx-band in both the rectangular and cylindrical DRAs.

The T-shaped configuration is employed in designing a sub-array lattice with rectangular DRAs, as shown in Fig.3.22. The coupling coefficient between the Tx and Rx. DRAs

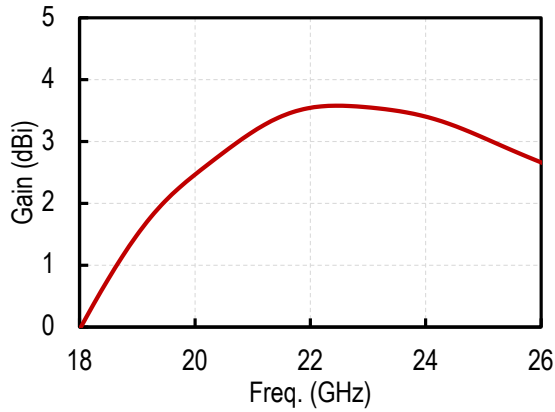


(a) Reflection coefficient

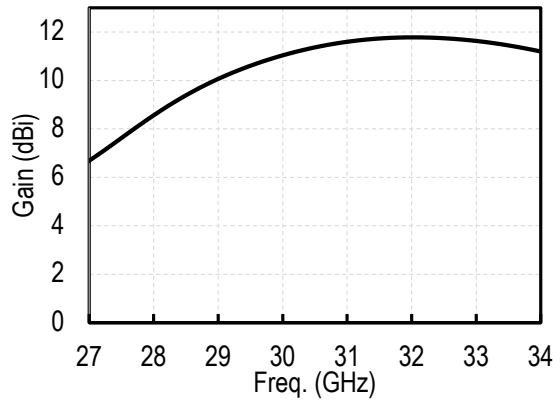


(b) Isolation between Rx and Tx

Figure 3.23: The Reflection/coupling coefficients of the shared-aperture array



(a) Rx



(b) Tx

Figure 3.24: The realized gain of the shared sub-array

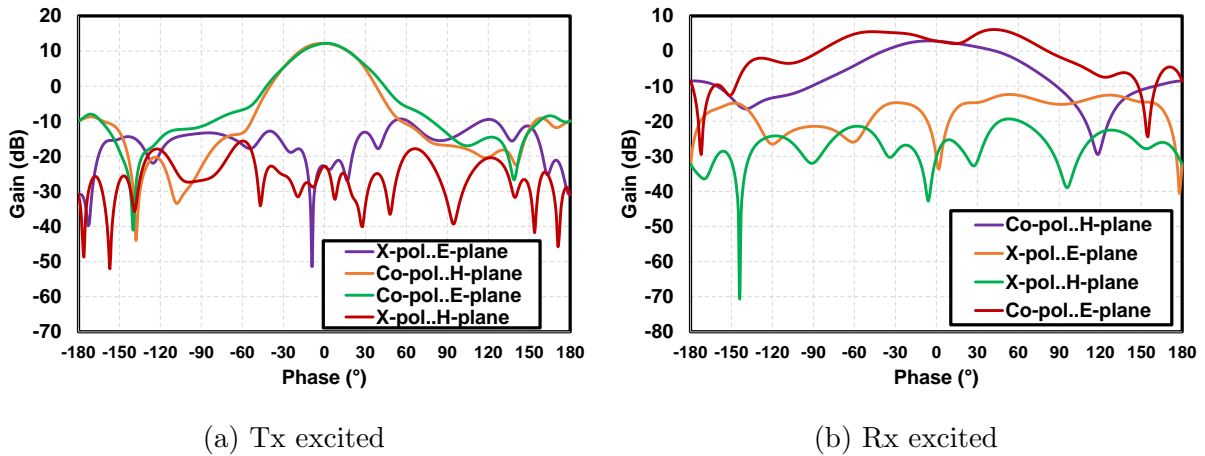


Figure 3.25: The radiation characteristics of the shared-aperture array a)Rx b)Tx

are shown in Fig.3.23b. The isolation between the Tx and Rx DRAs ( $S_{ij}$ ) is less than 50 dB at the Tx. Fig. 3.25 depicts the simulated radiation patterns of the shared sub-array in the XZ- and YZ-planes, simulated at the reflection coefficient minima of the return loss patterns, at the  $K_a$ -,  $K$ -band. The cross-polarization level is 30 dB lower than the simulated co-polarization level at the bore-sight direction in both planes. Symmetric patterns and almost low cross-polarization are obtained in the two perpendicular planes because of the symmetry.

### 3.8 Conclusion

This chapter has presented the procedure of implementing shared aperture phased array antennas for  $K$ -/ $K_a$ - band applications using DRAs. Two different configurations are addressed. A preliminary study for prototype sub-arrays is performed to validate the performances of the proposed interleaved array. A  $K$ -/ $K_a$ -band shared-aperture array with improved isolation is introduced. Several investigations will be performed to enhance the isolation between the Tx and Rx-band radiators, such as choosing a different feeding mechanism for the  $K$ -/ $K_a$ - band. Since the size of the feeding network of the Rx DRA is critical, it is crucial to choose a convenient feeding method that minimizes the footprint of the feeding network of the RX DRA. Further, the feeding method selected for both Tx DRA and Rx DRA should avoid the drawbacks of the conventional planar transmission line technologies at mm-wave bands. Moreover, implementing the chosen feeding network of

the shared aperture should maintain a low profile with minimum possible substrate layers, avoiding blind or buried vias for ease of manufacturing. Based on the stated considerations, the substrate integrated coaxial line (SICL), supporting the  $TEM$  mode, is proposed to feed the RX DRA and is presented in Chapter 4. In addition, the substrate integrated waveguide (SIW), supporting the  $TE_{10}$  mode, is selected to feed the TX DRA and is presented in Chapter 5. The implemented DRA shared aperture with the combined feeding techniques (i.e., SICL and SIW) is shown in Chapter 6.

# Chapter 4

## Substrate Integrated Coaxial Line-Integrated DRA

### 4.1 Introduction

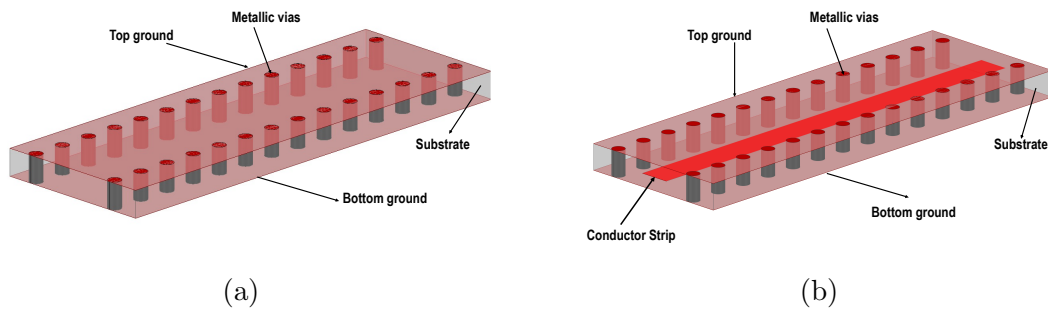


Figure 4.1: Schematic of the substrate integrated technologies: a) SIW b) SICL

The integration technologies in millimetre-wave (MM-wave) systems play a vital role in manufacturing circuits with compact, low weight, and possibly low-cost solutions for mass commercial production. Research has been devoted to developing numerous substrate integrated technologies to achieve a high level of integration with planar circuits. In this chapter, the substrate integrated coaxial line (SICL)- fed Dielectric Resonator Antenna (DRA) is proposed to reduce the footprint of the DRA in a shared-aperture configuration. The stand-alone DRA is designed to radiate in the  $K$ -band (i.e., 20 GHz). Based on

the specifications introduced in Chapter 3, the antenna operating at the  $K$ -band should provide the smallest possible physical area, present a wide-band impedance matching of 2 GHz or more, and a cross-polarization of 30 dB along with the operating band. First, the chapter summarizes the SICL technology, the different versions introduced for the SICL in the published literature, the transitions between the SICL and other technologies, and the reported SICL-integrated antennas. Secondly, the integrated design of the SICL and the DRA is presented. Then, the simulation results using the full-wave solver (HFSS) are introduced. Fabrication of the designed DRA is performed using 3D printing technology and compared with a commercial machined DRA. The measured reflection coefficients and radiation patterns are compared to the simulation results. Finally, a summary of the achieved performance will conclude the chapter.

## 4.2 Planar Transmission Lines Technologies

As mentioned in chapter 1, there is currently a tremendous need for components (passive and active) that feature wideband operation to support diverse applications in the mm-wave range. Transmission lines are the essential component of any microwave system. Thus, the basic requirements for the transmission line technology (integration technology) are to support one mode of operation over a wide bandwidth, be non-dispersive, and be highly decoupled from surrounding interference [23]. Further, the integration technology should be capable of combining multiple passive and active components [23]. Finally, low-cost manufacturing technology ensures microwave components come to the user at a low-cost [23].

Conventional planar transmission line technologies, such as microstrip lines (MS), coplanar waveguides (CPW), and strip lines (SL), are prone to dispersion and crosstalk [23], and are not convenient for higher frequency applications. Other innovative guiding technologies have been developed along with the move towards microwave and mm-wave ranges. Such structures aim to combine the advantages of the previously developed integrated circuits and the non-planar robust transmission lines (i.e., metallic waveguides and Coaxial lines). The first structure is the substrate integrated waveguide (SIW), illustrated in Fig 4.1 (a). SIW has gained the attention of researchers since Ke. Wu and al; published their first paper in [23]. SIW shares with the metallic waveguide the ability of interference rejection owing to their shielded structures. Further, SIW is implemented in a planar substrate form. Thus, it provides a high level of integration with other planar components and can be implemented using diverse manufacturing processes such as Printed Circuit Boards(PCB) and Low-Temperature Co-fired Ceramic (LTCC). Afterwards, many innovative passive and

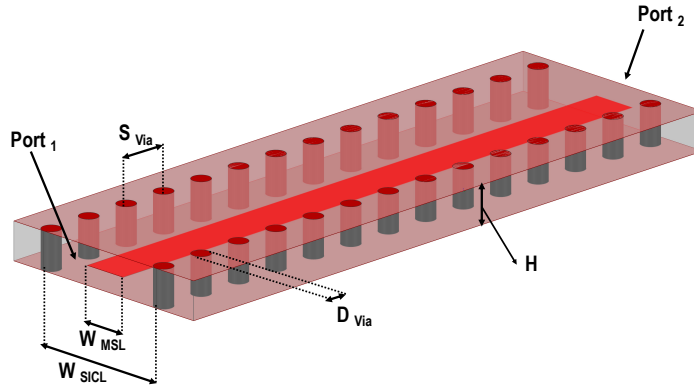


Figure 4.2: Geometry of the SICL

active components and complete systems were proposed using SIW. Continued to this development, the Substrate Integrated Coaxial Line (SICL) is a new technology that features the design of coaxial line in rectangular substrate form, illustrated in Fig 4.1 (b). In the next section, the development of the SICL will be introduced.

### 4.3 Substrate Integrated Coaxial Line

The coaxial line is the most popular transmission line that features a Transverse Electro-Magnetic (*TEM*) mode transmission, i.e. zero cut-off frequency. Accordingly, the *TEM* mode allows the development of components with wide frequency bandwidth. One of the unique features of the coaxial line is its small footprint. This feature makes it superior to waveguide in reducing the space in high dense circuits. Further, the shielding of the coaxial line is vital in minimizing crosstalk and interference, especially in high-frequency operations. Like SIWs, a coaxial line integrated into a planar substrate is proposed in [23] to allow the integration of a coaxial line with planar circuits. It is known as Substrate Integrated Coaxial Line (SICL). i.e., the SICL mitigates the planar form's coaxial line and supports the fundamental *TEM* mode propagation. The SICL consists of a printed conductor, between two layers of grounded substrates, shielded by metallized via on both sides as shown in Fig.4.1 (b).

### 4.3.1 Substrate Integrated Coaxial Line Characteristics

SICL provides a high power handling capability with low ohmic losses in substrate form. The advantages of using the SICLs are easy integration with active devices, broad bandwidth operation, low transmission loss, and small layout. Comparing the size of the SIW with the SICL, the SIW line width is controlled by the cut-off frequency of the dominant ( $TE_{10}$ ) mode. Thus, this width is larger than half of the guided wavelength ( $0.5 \times \lambda_g$ ) [73]. On the other hand, the width of the SICL is used to control the propagation of the higher-order  $TE_{10}$  mode. Thus, the SICL constitutes less space compared to the SIW. Accordingly, compact antenna structures is achieved using SICL [73, 74]. This feature is important in highly dense arrays, where the large spacing between elements can generate grating lobes.

Regarding the transmission loss of the SICL, In [75], the transmission loss of the SICL is characterized and compared with MS and grounded coplanar waveguide (GCPW). SICL has lower transmission loss compared to MS and CPW. Also, comparing SICL with SL, the loss reported of the power divider configuration is less when implemented in SICL technology than when using SL.

Moreover, a variety of processes are used to implement circuits in SICL technology such as thin film is used in [76], standard PCB process [77], multilayer liquid crystal polymer (LCP) process [73], and LTCC [78], Microelectromechanical (MEMS) technology [79].

Multiple works in literature implemented the SICL technique in diverse applications, such as cavities and filters [23, 76], antennas [73, 74, 80, 81], balun [82], ring resonators [83], and hybrid coupler [84]. In [85], SICL is also used to design feed rotary joint in broadband microwave systems.

### 4.3.2 Substrate integrated Coaxial Line-fed Antennas

The SICL is reported to feed several type of antennas such as rotman lens [86], wideband circularly polarized (CP) microstrip antenna array based on sequential rotation (SR) technique in [87], bow-tie transverse slots in [88], magnetoelectric (ME) dipole antenna [89], [75], microwave ablation antenna [90], patch antennas [77, 87], slot arrays [73, 74, 81]. However, the disadvantage of using slot/ metallic patch antennas at mm-wave frequencies are their low efficiency arised from their higher conductor loss.

On the other hand, DRAs possess several advantages, as illustrated in Chapter 3. In particular, DRAs are characterized by high efficiency and broader impedance bandwidth. To the best of my knowledge, no SICL-fed DRA is proposed in published work. SIW-fed DRAs have been reported with significant efficiency. Similar to SIW-DRA integration,

SICL will preserve the benefits of minimizing the parasitic and radiation losses at the mm-wave range. In addition, integrating DRAs with SICL will further provide wider operating bandwidth and compact footprint than SIW-fed DRAs. Therefore, the SICL-fed integrated DRA is proposed for feeding the  $K$ -band antenna.

### 4.3.3 Analysis

The SICL allows the propagation of the fundamental the  $TEM$  mode.  $TE_{10}$  mode is the first upper mode of the SICL, its cut-off frequency is calculated from the formula [23]

$$f_{TE10} = \frac{C}{2\sqrt{\epsilon_r}} \left( W_{SICL} - \frac{D_{via}^2}{0.95S_{via}} \right)^{-1} \quad (4.1)$$

where  $W_{SICL}$ ,  $D_{via}$  and  $S_{via}$  are the width of the SICL line, the diameter of the shielding vias, and the separation between the vias as illustrated in Fig.4.2.  $\epsilon_r$  is the relative dielectric permittivity of the substrate, and  $C$  is the speed of light.

Since the parameters  $D_{via}$ , and  $S_{via}$  are mainly determined by the manufacturing guidelines. Thus, the width of the SICL ( $W_{SICL}$ ) controls the unimodal bandwidth operation of the  $TEM$  mode. The ratio between the structure's height ( $H$ ) and the inner strip's width ( $W_{MSL}$ ) is responsible for controlling the characteristic impedance  $Z_0$  of the  $TEM$  mode. However, this formula doesn't take into account the conductor thickness and the process of the fabrication (i.e. MEMS, PCB) [91]. Accordingly, deviation from the theoretical value occurs depending on the actual thickness of the conductor [91].

### 4.3.4 SICL Transitions

Transitions are an essential part of the design process of any integration technology. Transitions are required to efficiently couple the power between the signal conductor and coaxial-based measurement systems. Several transitions have been reported between the SICL and other transmission lines [78, 81, 92–94]. In [92], a transition between a coplanar waveguide (CPW) and SICL is realized using a via connecting the strip conductor and the CPW. The transition between coaxial and SICL is reported in [78, 93]. In [78], LTCC technology is used to perform multiple data transmissions using the SICL array. In coaxial to SICL transitions, a metallized blind via is used to connect the signal from the middle conductor to the SICL, and ground vias are used to connect the outer conductor of the coaxial to the

ground surfaces of SICL. The transition between coaxial and grounded coplanar waveguide (GCPW) is reported in [81,94]. In [94], the change of the vertical thermal coefficient effect between copper and dielectrics is addressed as a possible cause for metal via breaks in the multilayer process. Accordingly, a three-dimensional GCPW (3D-GCPW) transition is presented in [94] to reduce the demand for machining accuracy of the vertical via manufacturing. In all the mentioned transitions, the ground vias play an essential part in providing the required shielding of the quasi-coaxial structure and maintaining stable operation.

### 4.3.5 SICL Versions

Several versions have been developed for the SICL to enhance their performance or ease manufacturing. This section introduces the following versions: the empty substrate integrated coaxial line, the mode composite transmission line, the ridge substrate integrated coaxial line, the asymmetric substrate integrated coaxial line, and the substrate integrated double strip coaxial line.

#### Empty Substrate Integrated Coaxial Line

Empty substrate integrated coaxial line (ESICL) was presented in [95,96]. The ESICL is equivalent to the SICL structure but without the dielectric substrate as demonstrated in Fig.4.3 (a) (i.e., substrate-free SICL). The ESICL has been employed in literature in filters [96–98], passive devices [84]. Further, several transitions between ESICL and other transmission line technologies are reported in [95,99]. The reported ESICL designs are featured by considerable low loss arising from removing the dielectric medium, high-quality factor, and dispersion-less. Accordingly, the power capability is increased. Though the above advantages, the ESICL is not suitable for integration with planar circuits.

#### Mode Composite Transmission Line

Mode composite transmission line (MCTL) is presented in [100] as a possible solution to reduce the footprint of multimode guiding structures, in which different types of transmission lines are combined to support different transmission modes. Typically, each mode is excited within different parts of the transmission medium. The design of the mode composite structures requires high isolation between the two ports. In [100], the guiding space is fully shared between the two different transmission modes. The MCTL supports both

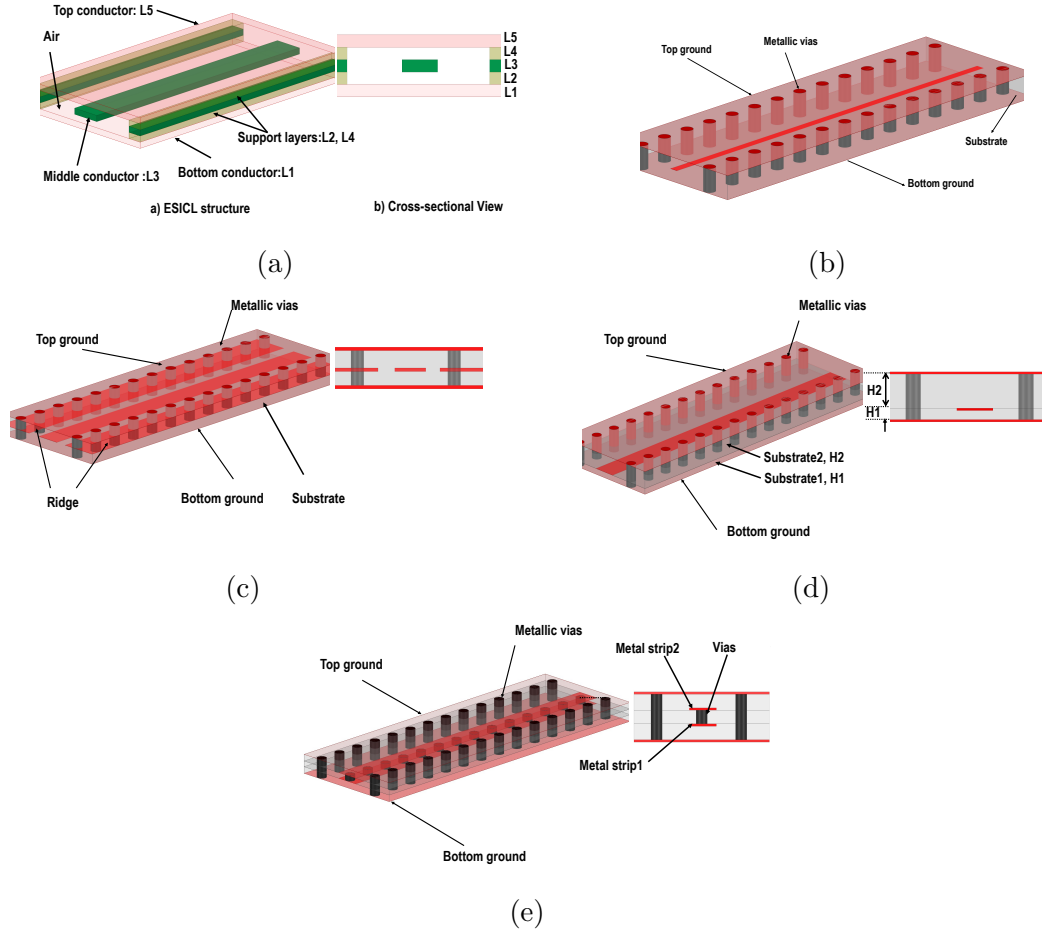


Figure 4.3: SACL modified versions a) ESICL b) MCTL c) RSICL d) ASICL e) SIDSL

the  $TEM$ - mode and  $TE_{10}$  -mode in the same guiding space as shown in Fig. 4.3 (b). Like SIW, MCTL is composed of two conducting plates, along with two rows of metalized vias, which will support the  $TE_{10}$  mode. Further, the middle conductor, embedded between the two dielectric layers, supports the  $TEM$  mode propagation. The orthogonality of both modes will allow the propagation of each one without any considerable interference. The MCTL's lateral dimensions (Width of the strip and height) are characterized by a large aspect ratio. Thus, the strip won't disturb the  $TE_{10}$  mode in the SIW guiding structure, and the field is almost uniform. At the same time, the field of the  $TEM$ -mode is concentrated around the middle strip, which resembles the stripline field distribution than the

SICL. The MCTL is useful in applications in which dual polarization is required using two different propagation modes and where the guidance space is critical as proposed in [100].

### **Ridged Substrate Integrated Coaxial Line**

In [101, 102], a Ridged Substrate Integrated Coaxial Line (RSICL) is proposed to reduce the size of the SICL. The two added ridges on both sides to the conventional SICL provide increased shielding and thus mitigate the field leakage compared to the SICL as shown in Fig. 4.3 (c) [101, 102]. The ridges introduce extra capacitance to the line. Therefore, the characteristic impedance of the RSICL is less than SICL of the same width. Accordingly, reduced size can be obtained using the RSICL, and more unimodal bandwidth is achieved. It is noted that those ridges were present in the [78] as a fabrication method of realizing the SICL. However, the effect of the ridge wasn't analyzed as part of the design process. In [17, 101], the RSICL is analyzed, and transitions between the RSICL and GCPW are introduced. Due to the introduced capacitance by the two ridges, the width of the RSICL for a specific characteristic impedance is less than its SICL equivalent. Accordingly, the unimodal TEM bandwidth is more significant in the RSICL.

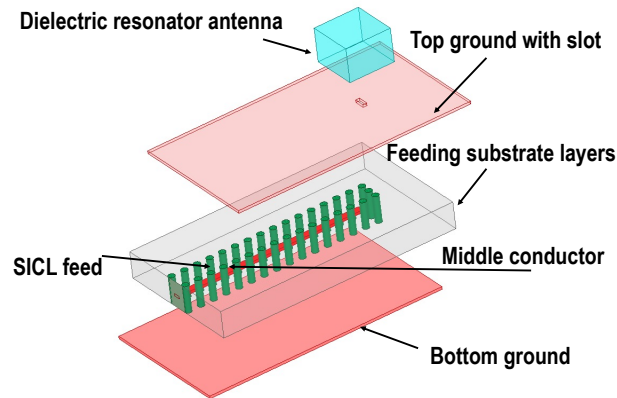
### **Asymmetric Substrate Integrated Coaxial Line**

The Asymmetric Substrate Integrated Coaxial line (ASICL) is a modified version of the SICL, where two different substrates are used as shown in Fig. 4.3 (d) [103, 104]. The ASICL also supports the dominant TEM mode over a wide frequency band. Further, the electric-field distribution of the ASICL presents a more substantial power density in the narrower substrate [104]. Accordingly, the field distribution is similar to that of microstrip line (MSL) [104].

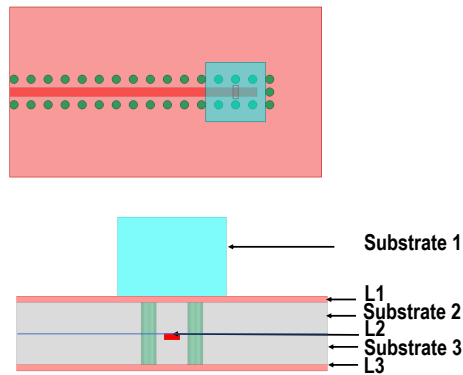
### **Substrate integrated Double-strip Coaxial Line**

The substrate integrated double-strip coaxial line (SIDSCL) was presented by [105]. The SIDSCL differs from the conventional SICL in that it is composed of two parallel signal lines instead of one, as shown in Fig. 4.3. To ensure the uniformity of the voltage and phase distribution on the two conductor strips, equally spaced buried vias connect the two signal strips together [105]. Using the SIDSCL, the authors designed a 10-dB coupler directional coupler. In the coupler's design, the connecting via-holes between strips are removed. The design is meant to provide more flexibility in the design and space-saving. However, its drawback is the need for multilayer implementation.

## 4.4 SICL-fed DRA Design



(a)



(b)

Figure 4.4: Proposed SICL-fed K-band DRA. a) Exploded view b) Cross-sectional view

The geometry of the proposed DRA antenna with a SICL feed is shown in Fig. 4.4. Three substrate layers are employed in the design. The first substrate layer represents the DRA block, integrated on the top conductor layer, whereas two substrate layers incorporate the SICL feed network. Two layers of 0.5 oz copper laminated substrates of a 10-mils thick RO 3006™, with dielectric constant ( $\epsilon_r$ ) of 6.15 and loss tangent ( $\tan\delta$ ) of 0.002 are used as the SICL-feed layers. 3D-printed commercial filament, with ( $\epsilon_r$ ) of 10, is used for the DRAs. In addition to the 3D-printed DRAs, machined DRAs implemented

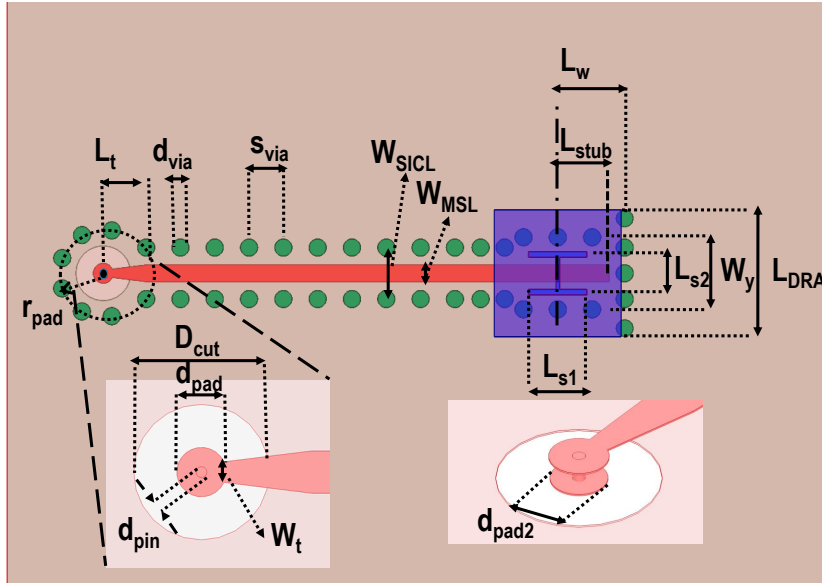


Figure 4.5: Geometry of the Proposed SICL-fed K-band DRA

from commercial substrates are used as a benchmark compared to the 3D-printed DRAs. RT/Duroid<sup>®</sup> laminates with 75-mils thickness,  $\epsilon_r$  of 10.2, and  $\tan\delta$  of 0.0023 is used for the machined *K*-band radiator.

Fig. 4.5 shows the detailed design parameters for the *K*-band DRA structure (elevation view), which consists of two parts: a square DRA and a SICL-slotted line. The square DRA of dimensions ( $L_{DRA} \times L_{DRA} \times h_{DRA}$ ) is designed to excite the fundamental mode  $TE_{111}^y$  at the *K*-band (i.e., 20 GHz). The  $h_{DRA}$  is fixed to 75 mils as of the predetermined laminate thickness. Firstly, the DRA's resonance frequency ( $f_R=20$  GHz) is evaluated using the

Table 4.1: Geometrical dimensions of the SICL-DRA antenna in (mm)

$L_{stub}$	$L_{DRA}$	$L_{s1}$	$L_{s2}$	$L_w$	$L_t$	$W_y$	$W_{MSL}$	$S_{via}$
1.5	3.7	1.7	1.1	0.11	1.03	2.1	0.5	1
$W_{SICL}$	$W_t$	$D_{cut}$	$d_{pad}$	$d_{pad2}$	$r_{pad}$	$d_{pin}$	$d_{wall}$	$d_{via}$
1.5	0.243	1.6	0.558	0.559	1.25	0.127	1.95	0.5

dielectric waveguide method (DWM) [52]. Then,  $f_R$  verification using the eigenmode solver of, ANSYS high-frequency structure simulator (HFSS) [71] is performed, which is slightly different due to the presence of the SICL along with the isolated DRA.

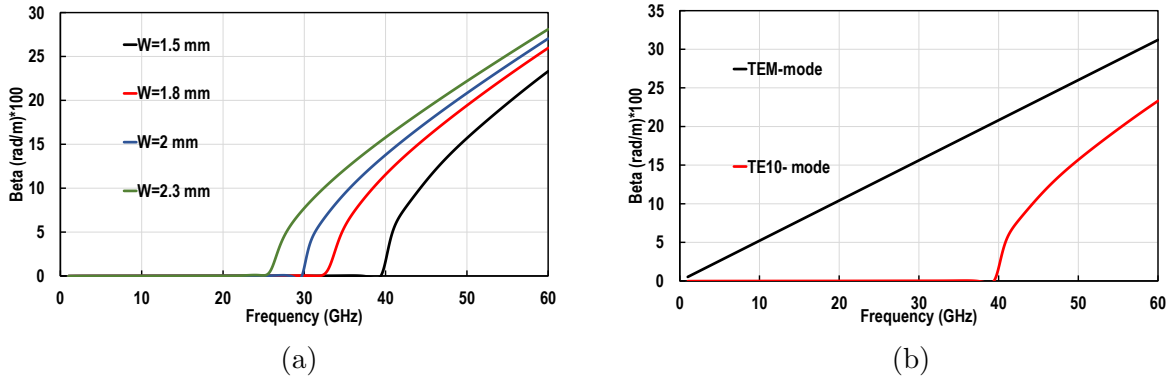


Figure 4.6: Propagation constant of the SICL-line a) higher order mode vs width b) propagating mode vs frequency

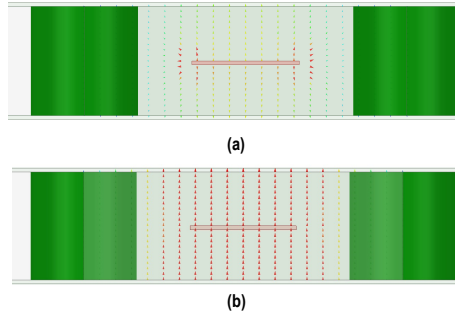


Figure 4.7: The generated SICL modes a) Fundamental: TEM mode b) Higher order mode: TE10

The DRA is aperture-fed using a slot etched on the top conductor layer ( $L1$ ) (see Fig. 4.4 (b)). The slot is excited using a SICL, designed using two 10-mils thick substrate layers. The diameter of the vias ( $d_{via}$ ), and the distance between successive vias ( $s_{via}$ ) (see Fig. 4.5) are set according to the guidelines presented in [106]. RO 3006™ substrate of ( $\epsilon_r$ ) of 6.15 is selected to minimize the width of the SICL. The unimodal operation is controlled by the width of the SICL ( $W_{SICL}$ ) (see Fig. 4.5). The dispersion curves of the higher order mode  $TE_{10}$  for different SICL' widths are presented in Fig.4.6(a). The ( $W_{SICL}$ ) is

set so the upper high order mode  $TE_{10}$  operates above 40 GHz [23], as illustrated in Fig.4.6 (b) representing the dispersion curve of both the fundamental (i.e.  $TEM$  mode) and the higher order mode (i.e.,  $TE_{10}$  mode). The corresponding E-field distribution of each mode is illustrated in Fig.4.7.

The impedance of the SICL is controlled by the ratio between the total substrates' height (20-mils) to the width of the conductor ( $W_{MSL}$ ) [23] on ( $L_2$ ) (see Fig. 4.4 (b)). Further, the impedance matching is achieved by optimizing the length of the open-circuited stub of the middle conductor ( $L_{stub}$ ) and slot length (see Fig. 4.5) to provide two radiation nulls in the reflection coefficient response. The optimized slot length is bent to form an H-shaped with two arm dimensions of ( $l_{s1}$ ,  $l_{s2}$ ) for feeding structure size reduction, as illustrated in the geometry of the SICL-DRA (see Fig. 4.5). The slot widths are initially set to one-tenth of slot lengths. Further, the width of the SICL is widened under the DRA to accommodate the optimized slot length. The variation of the reflection coefficient with the DRA's length ( $L_{DRA}$ ) and the longitudinal H-slot's length ( $L_{s1}$ ) are plotted in Fig.4.8 (a), and (b), respectively. Further, the field distribution at the first and second resonance is embedded in Fig.4.8 (a), and (b), respectively. The first resonance represents the slot-DRA's excitation using the longitudinal current passing along the SICL, as shown in the electric field distribution in Fig.4.8 (a). Thus, the DRA's length is used to tune the first resonance as depicted in Fig.4.8 (a). At the same time, the second resonance arises from the resonance of the longitudinal H-slot's length ( $L_{s1}$ ), as illustrated in the electric field distribution in Fig.4.8 (b).

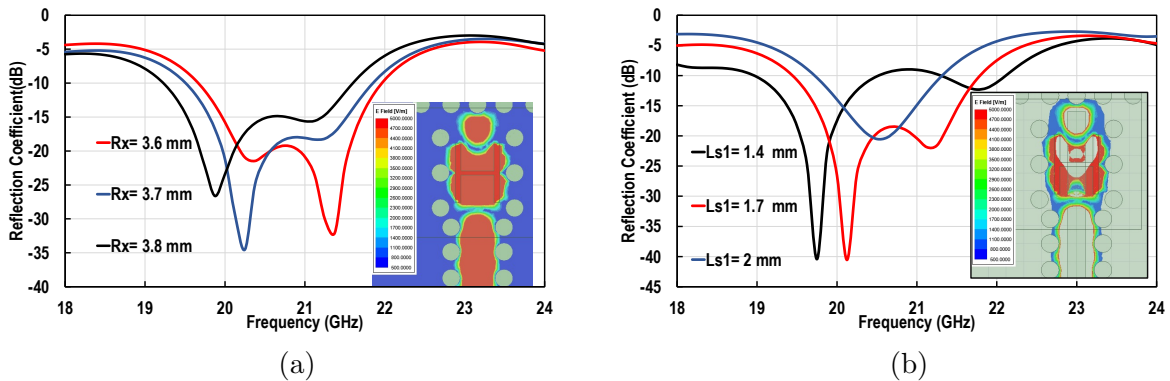


Figure 4.8: Reflection Coefficient the SICL-fed DRA versus a) DRA's length b) Slot longitudinal length

A vertical coaxial to SICL transition is designed to couple the power to the SICL for the convenience of the coaxial-based measurement systems (see Fig.4.9). The transition is

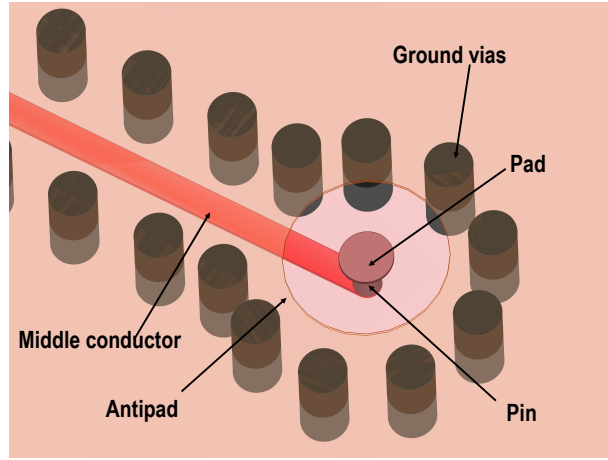


Figure 4.9: Geometry of the Coaxial to SICL Transition

designed to match a commercial mini connector from Southwest Inc. [107]. A signal blind via with diameter ( $d_{pin}$ ) (see Fig. 4.5) is connected to the inner conductor of SICL, ground metallized vias are distributed around the signal via at a radius of ( $r_{pad}$ ), and connecting the top and bottom conductor layers ( $L_1$  and  $L_3$ ) of the SICL line (see Fig. 4.4 (b)). For proper measurements, a pad of diameter ( $d_{pad2}$ ) (see Fig. 4.5) on layer ( $L_1$ ) is attached to the signal via, and a circular anti pad with diameter ( $D_{cut}$ ) is cut on the same layer. A tapered line of length ( $L_t$ ) is used to match the impedance of the SICL and the vertical coaxial signal via, and a pad of diameter ( $d_{pad}$ ) is added for proper manufacturing. Final optimized parameters are listed in Table 4.1.

A back-to-back (B2B) test structure of the transition is designed as shown in Fig. 4.10 to test the transition and characterize the transition loss. The final optimized values are stated in Table 4.2. Another model for the 3D-printed DRA is simulated as well. The model used considers the effect of the attached sheet and the electrical properties of the used filament. Fig. 4.11 (a), and Fig. 4.12 (a), and (b) show the simulated results of the B2B test structure and the  $K$ - band DRA over the band of the operation. The back-to-back structure of length 10 mm presents a very low transmission loss of 0.3 dB and a broad 10-dB return loss from 16.8 to 27.5 GHz. The antenna impedance bandwidth is from 19.5 GHz to 21.8 GHz (11 %), with a simulated peak realized gain of 5.2 dBi. Further, the difference between the simulated DRA using the Rogers/RT Duroid 6010 model and the 3D- printed model shows a slight difference between the two models. In addition, the cross-polarization level is better than 50 dB in the boresight direction in both E- and H-planes for both the machined and the 3D printed model.

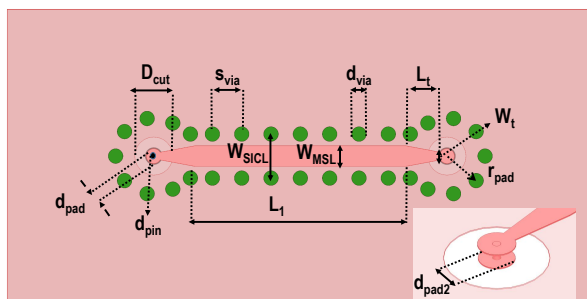


Figure 4.10: Configuration of the B2B structure of the SICL

Table 4.2: Geometrical dimensions of the SICL-B2B structure in (mm)

$L_t$	$W_{MSL}$	$W_{SICL}$	$W_t$	$D_{cut}$	$d_{pad}$
1.18	0.7	1.5	0.26	1.3	0.584
$d_{pad2}$	$r_{pad}$	$d_{pin}$	$d_t$	$d_{via}$	$S_{via}$
0.508	1.3	0.127	7.2	0.5	1

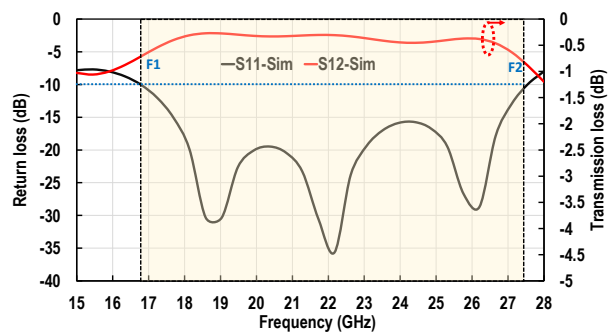
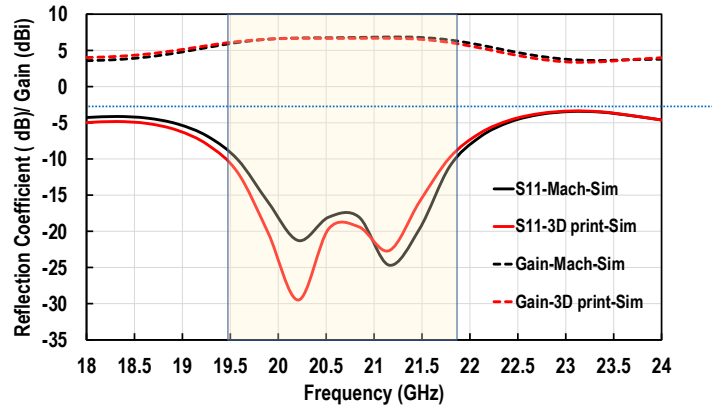
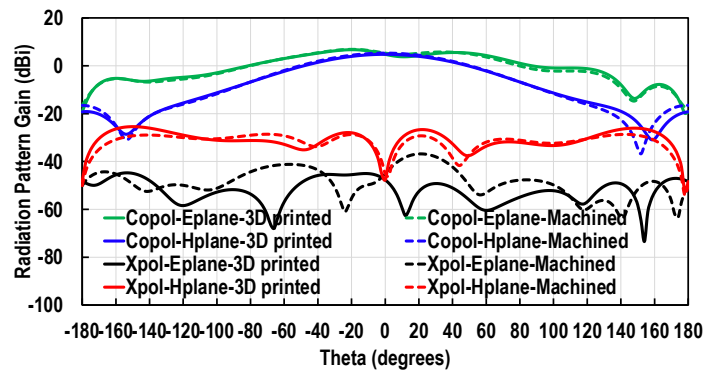


Figure 4.11: Simulation results of the B2B SICL line



(a)



(b)

Figure 4.12: Simulation results for the SICL-fed DRA. a) The S-parameters and Gain b) Radiation pattern gain

## 4.5 Simulation versus Measurement Results

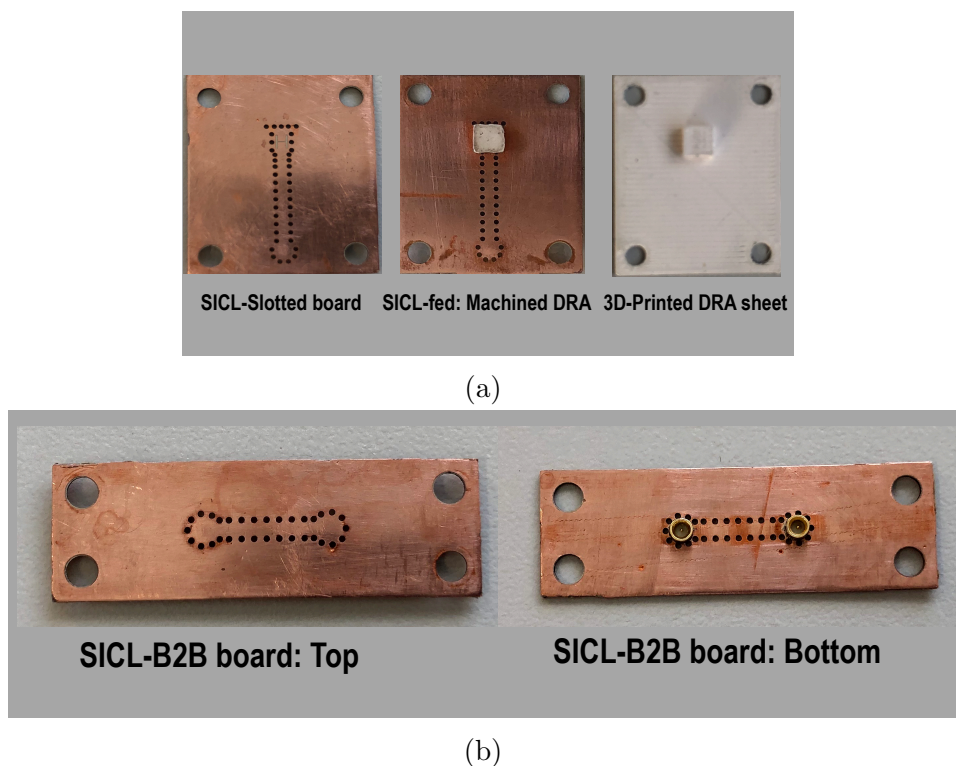


Figure 4.13: Fabricated PCB boards a)  $K$ -band antenna boards b) B2B circuit boards

A top-view photograph of the fabricated PCB and the 3D-printed DRA antenna is shown in Fig. 4.13 (a). Mini-coaxial surface mount RF connectors from southwest microwave Inc. [107] are soldered on the back of the fabricated board to feed the antenna and circuit boards. Moreover, a back-to-back (B2B) test structure of the coaxial to SICL transition is designed to characterize their transition loss (see Fig.4.13 (b)). The reflection coefficient for the antenna boards is measured using Keysight VNA to identify the measured center frequencies; then, the radiation pattern measurements are performed using the planar near-field measurement system (NSI) [108].

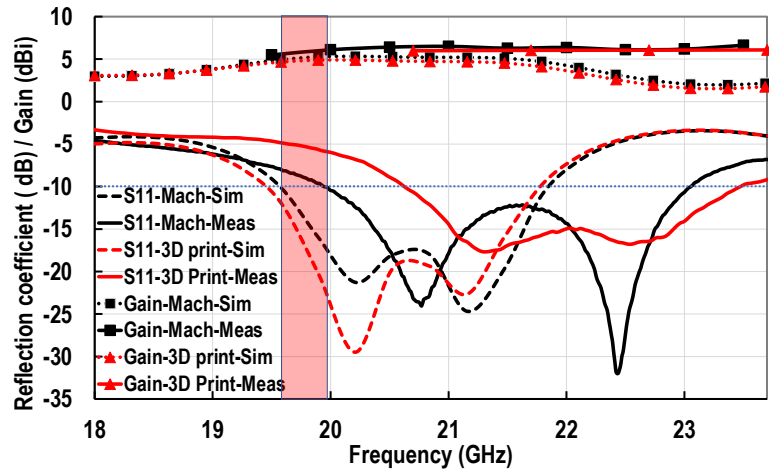


Figure 4.14: SICL fed DRA: Measured Vs simulated Reflection coefficient and Gain

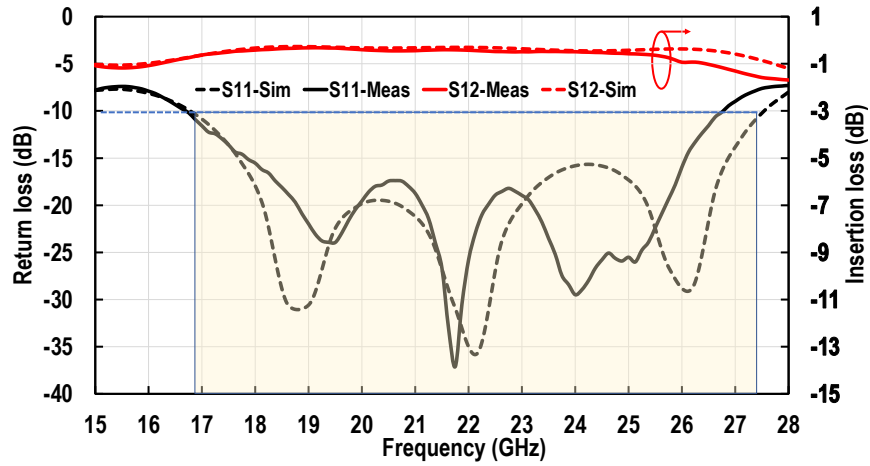


Figure 4.15: SICL-back to back transition: Measured Vs simulated Return S-parameters

### 4.5.1 S-parameters

Fig. 4.14 shows the simulation versus measurement results for the reflection coefficient of the machined and 3D-printed  $K$ -band SICL-fed DRAs over the operating frequency band. The simulated and measured reflection coefficient shows close agreement regarding the number of minima. The discrepancy in the minima resonance is associated with the change in the matching conditions. The latter originated from the dimensions' tolerance of the measured prototypes, the effect of glueing the DRAs (i.e., Machined DRAs) and the possible presence of a small air gap between the PCBs and the 3D-printed sheet (i.e., 3D-printed DRAs). The -10-dB impedance BW is 2 GHz (19.5-to-21.5 GHz), 3 GHz (19.95-to-23.04 GHz), 3 GHz (20.6-to-23.5 GHz) for the simulated, machined, and 3D-printed DRA, respectively (see Fig. 4.14). Both machined and 3D-printed DRAs frequency responses present a deviation in the operating frequency band. This deviation is mainly attributed to the following factors: the practical ( $\epsilon_r$ ) variations of the fabricated materials (i.e., substrates & 3D-printed materials), and the fabrication tolerance of the boards' dimensions provided by the manufacturer. For the verification of the transition performance, a 10-mm long B2B test structure of the designed vertical coaxial to SICL transition is measured and compared to the simulated results (see Fig. 4.15). The B2B structure shows a simulated insertion loss (IL) of 0.3 dB/cm, over a 10-dB simulated return loss (RL) bandwidth ( $|S_{11}| < -10$ dB) of 10.7 GHz from (16.8-to-27.5 GHz). Whereas the measured average (IL) is 0.44 dB/cm over the operating band (17-to-25 GHz), along with a 10-dB RL over the band (16.5-to-26.7 GHz).

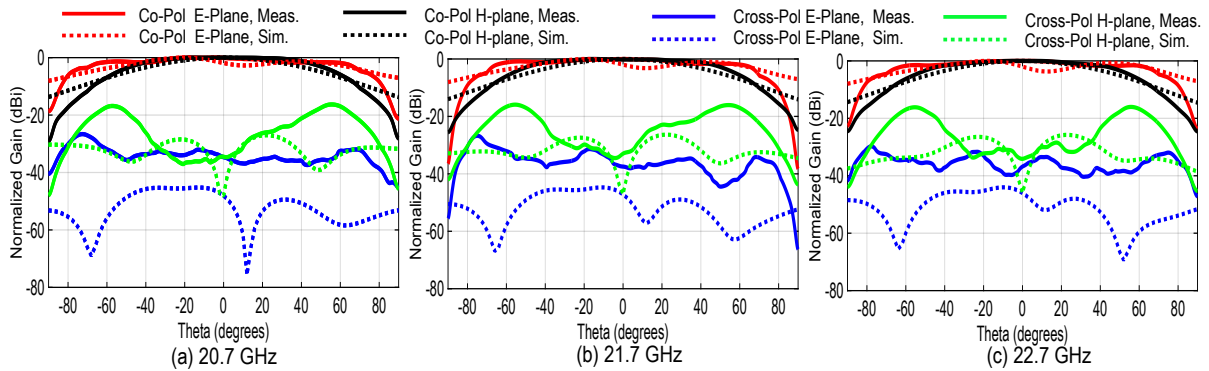


Figure 4.16: Measured vs simulated normalized radiation patterns of the 3D-printed  $K$ -band antenna

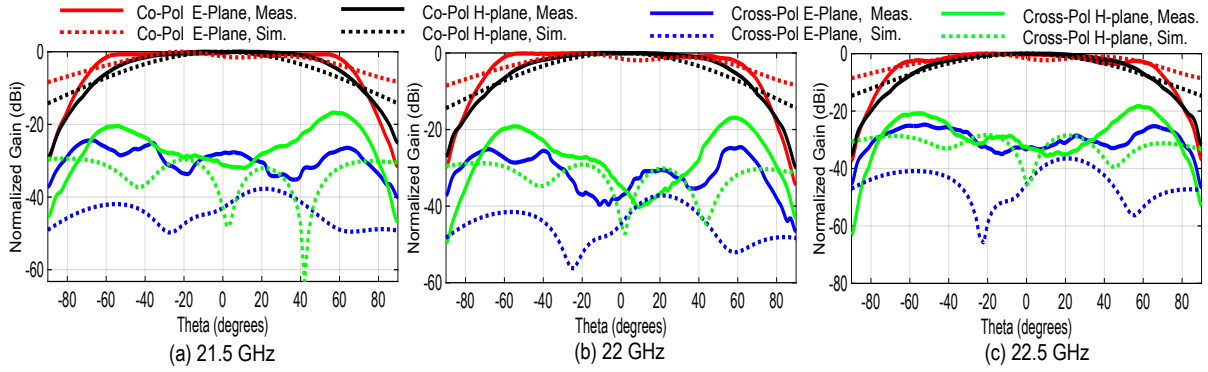


Figure 4.17: Measured vs simulated normalized radiation patterns of the machined *K*-band antenna

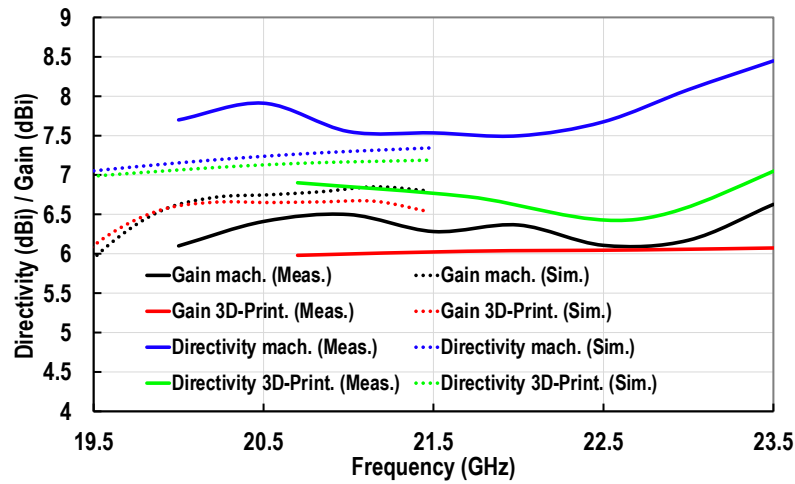


Figure 4.18: Measured vs simulated realized gain and directivity of the *K*-band DRA

## 4.5.2 Radiation Pattern Gain

The radiation pattern gain measurement was performed by the planar NSI system [108] for the antenna boards. The simulated and measured realized gains for the machined and 3D-printed  $K$ -band DRA are demonstrated over their operating bandwidth as shown in Fig. 4.14. The average simulated realized gain is 6.6 dBi for the machined  $K$ -band DRA (see Fig. 4.14), with almost similar performance for the 3D-printed versions. The measured results present an excellent agreement taking into account the possible estimation error in the near field measurement of the gain [109]. The measured normalized radiation patterns in the E- and H-plane are presented for the 3D-printed and machined DRAs at  $K$ -band in Fig. 4.16, and Fig. 4.17, respectively. For the 3D-printed SICL-fed DRA, the measured cross-polarization level is lower than -32 dB, -31 dB, -32 at 20.7 GHz, 21.7 GHz, and 22.6 GHz, respectively, at the boresight direction. For the machined SICL-fed DRA, the measured cross-polarization level is lower than -26, -33, -31 at 21.5 GHz, 22 GHz, and 22.5 GHz, respectively, at the boresight direction. Measurements across three frequencies depict stable radiation patterns for the 3D-printed and machined DRAs. Fig. 4.18 presents the measured maximum directivities and realized gains of both the machined and 3D-printed  $K$ -band DRAs. Gain measurements agree well with the simulations by considering the possible gain errors in the planar field measurements. Further, the 3D-printed DRA is presenting an average efficiency of 83 % compared to the average simulated efficiency of 85.3 %.

## 4.6 Sensitivity Analysis of Design Parameters

Full-wave simulations are performed to observe the tolerance of the antenna dimensions on the antenna performance, presented in Appendix A. The sensitivity analysis is performed by considering a possible 2 mils oversize in the design dimensions after manufacturing. Fig. A.1 illustrates the effect of the slot dimensions on the reflection coefficient characteristics. A  $2 \pm$  mils ( $\pm 0.05$  mm) variation in the width of the transverse arm of the slot ( $W_{S2}$ ) results in a + 20 % / -37 % change in the achievable impedance bandwidth. The effect of the other slot dimensions ( $L_{S1}$ ,  $L_{S2}$ ,  $W_{S1}$ ) is minimal on the reflection coefficient characteristics as shown in Fig. A.1. (a), (c), (d). Further, the variation of the SICL-coupled line dimensions, the quasi-coaxial transition, and the matching section on the reflection coefficient characteristics are presented in Fig. A.2 to Fig. A.4. respectively. The reflection coefficient is showing stable performance across all tuned parameters. Additionally, the variation of the DRA 's dimensions on the reflection coefficient characteristics is plotted

in Fig.A.5. DRA's size changes can alter the resonant frequency, but this tolerance is more prominent in machined DRAs than in 3D-printed DRAs. To conclude, the design parameters are insensitive to manufacturing tolerance.

## 4.7 Conclusion

A novel substrate integrated coaxial line (SICL)-fed Dielectric Resonator Antenna was presented in this chapter. Wideband operation is achieved by using the dual resonance effect of both the DRA and the slot coupled line. Full-wave simulations present a wideband reflection coefficient bandwidth ( i.e.,  $S_{11} < -10$  dB) of 2 GHz. The design concept of the SICL-fed DRA element is aimed to be integrated into a shared-aperture array. Thus, the selection of the feeding technology (i.e., SICL) and the design parameters targeted achieving low footprint DRA to fit in the shared-aperture configuration. The measured results agree well with the simulated ones in terms of the number of minima and realizing 3 GHz of bandwidth for both the machined and 3D-printed DRAs. The proposed SICL-integrated DRA was manufactured using 3D printing and low-cost PCB technology. To our best of knowledge, no publication targeted the integration of the SICL and the DRA. Most published work on planar SICL-fed antennas focused on slot antennas and patch antennas, with limited BW compared to the DRA.

# Chapter 5

## Substrate Integrated Waveguide DRAs

This chapter presents substrate integrated waveguide (SIW)- fed Dielectric Resonator Antenna (DRA) using two substrate layers to fulfill the target of implementing compact feed structure for shared-aperture applications. The stand-alone DRA is designed to radiate in the  $K_a$ -band (i.e., 30 GHz). Based on the specifications introduced in Chapter 3, the antenna operating at the  $K_a$ -band should share two substrate layers with the SICL-DRA, providing a wide-band impedance matching of 2 GHz or more a high cross-polarization of 35 dB across the operating band. First, the chapter summarizes the SIW technology, the different versions introduced for the SIW in published literature, transitions between SIW and other technologies, and the reported SIW-integrated antennas. Secondly, the integrated design of the SIW and the DRA is presented. Thirdly, simulation results using the full-wave solver ( HFSS) are introduced. Fabrication of the designed DRA is performed using 3D-printing technology and compared with a commercial machined DRA. The measured reflection coefficients and radiation patterns are compared to simulation results. Finally, a summary of the achieved performance will conclude the chapter.

### 5.1 Substrate Integrated Waveguide- An overview

The substrate integrated waveguide (SIW) was first proposed by Ke Wu in [22], in which the non-planar waveguide is incorporated in a planar substrate form [110]. The SIW technology introduced the advantage of uniformly integrating conventional planar transmission

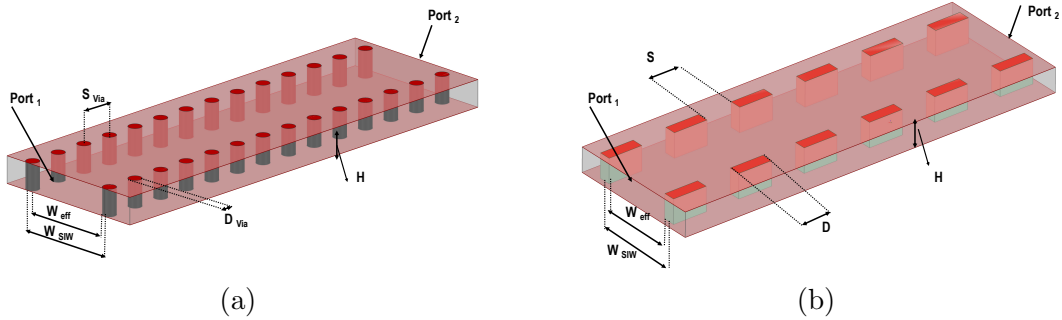


Figure 5.1: Schematic of the substrate integrated waveguide implementation: a) Circular vias b) Rectangular trench

lines (i.e., MS, CPW) with waveguide structures using the planar integrated circuits manufacturing process [110]. This technology provides not only low cost and uniform integration but also allows proper incorporation of both TEM-based and non-TEM-based systems together [110]. The lateral metallic walls in metallic waveguides are synthesized using metallized via holes, or metallic walls [110], as illustrated in Fig.5.1. Small vias with nearby separations in SIW provide a dispersion-less planar waveguide with negligible leakage effects [106]. Like the rectangular waveguide, SIW allows the propagation of the fundamental  $TE_{10}$  mode. Numerous components have been reported since then for SIW-based systems, and multiple published surveys reported those achievements [110–114]. Accordingly, this section will only highlight the main theme of SIW structures.

### 5.1.1 Substrate Integrated Waveguide Characteristics

Similar to the rectangular waveguide, SIW allows the propagation of the fundamental  $TE_{10}$  mode. The side vias only allow the propagation of the vertical current component because of the discontinuity of current in the longitudinal direction. Thus, SIW can only support  $TE_{n0}$  modes ( $n \neq 0$ ) [106].

Comparing the transmission losses in SIW with the conventional waveguides, the SIW is lossier due to the dielectric substrate's loss and the small height of the substrate [110], which can be reduced using low loss laminates. The other contributors to the transmission loss in SIW are conductor loss of the vias and metallic walls and the radiation loss from leakage between the vias [110]. The latter is almost ignored if the metallic vias' dimensions are properly selected [106, 110].

The SIW is characterized by a filter-like nature, arising from the single-mode operation

between predetermined cut-off frequencies of the fundamental (i.e.,  $TE_{10}$  mode) and the second propagating mode (typically,  $TE_{20}$  mode). This feature poses two challenges: the size of the SIW line and the bandwidth. Because of the analogue in the design procedure with a rectangular waveguide, the width of the SIW line is proportional to half of the guided wavelength ( $\lambda_g/2$ , where  $\lambda_g = \lambda_0/\sqrt{\epsilon_r}$ ). SIW is featured by low profile in comparison with the metallic waveguide. However, the width is more prominent than commonly used transmission lines, such as MS. This criterion poses a challenge in routing and integration in high-dense circuits.

The bandwidth is limited by the useful operating bandwidth between the predetermined cut-off frequencies. Therefore, the  $TE_{10}$ - mode structures' bandwidth is lower than the corresponding structures that support  $TEM$ - mode, such as MS, CPW, and SICL. Accordingly, several implementations have targeted miniaturization of the SIW's width and will be highlighted in the next section.

SIWs are fabricated using diverse techniques such as PCBs using high-frequency laminates (LTCC) techniques, in which dimensions are constrained by minimum features. Further, IC technologies have been used to perform SIW in silicon substrates [115], and other technologies are reported as thick film [116].

### 5.1.2 Analysis

The dispersion characteristics of SIW are investigated based on the similarity of  $TE_{10}$  mode field distribution between SIW and metallic waveguide [117, 118]. The gap between vias (defined by pitch size  $S_{via}$ , see Fig.5.1(a)) and the size of the metallic vias ( $d_{via}$ ) controls the radiation and the leakage of field through the vias [117, 118]. Further, the technological limitation in manufacturing controls the selection of those parameters. Initial dimensions of SIW are obtained using empirical equations in [117, 118], in which a waveguide with equivalent width ( $W_{eff}$ ) is defined and related to the SIW physical dimensions.

### 5.1.3 SIW Transitions

Transitions, the essential component for efficient integration and characterization measurement, have been reported for efficient power coupling between SIW and other transmission lines such as MS, CPW [22, 119–122]. An MS to SIW transition is one of the commonly used transitions, based on including a quarter-wave taper section between the top conductor of the SIW and the MS line [22, 119, 120]. In [121], a transition between a tapered MS

line and multisectional SIW is proposed for multilayer substrates. The transition between the MS line and SIW is performed on the same layer, providing seamless integration.

Further, CPW and GCPW to SIW transitions are proposed as more convenient transitions for higher frequency applications that require thick substrates [123]. Several designs are presented in [122, 124–127] in which multiple coupling techniques are presented in those transitions, such as vertical vias and coupling slots. Waveguide to SIW transition is performed through the intermediate transition from SIW to MS or CPW then to waveguide, or directly from waveguide to SIW by coupling using slots or probe.

Coaxial to SIW transitions are required for diverse applications, in which vertical integration is necessary or for direct compatibility with measurement instruments. Few designs have been reported for coaxial or quasi coaxial to SIW transitions [128–130]

#### 5.1.4 SIW Versions

Miniaturization of SIW- components and increasing the uni-modal operation of SIW are two main targets in achieving a compact and wideband operation for SIW-based systems. Several attempts that targeted this goal in literature are presented in this section.

##### Sub-mode SIM

Reducing the size of SIW is implemented by sectioning the SIW's broadside wall through a defined axis. The miniaturization of SIW is based on the SIW's field symmetry, and the large aspect ratio of SIW (i.e., Width to height ratio) [131]. Half-mode SIW (HMSIW), and Quarter mode SIW (QMSIW) are first implementation of this concept [131], and [132]. In HMSIW, half of the waveguide is only utilized, creating an open-sided wall and a short-circuited side of periodically-spaced vias as shown in Fig.5.2(a). The open-sided wall is equivalent to a PMC wall, eventually allowing some radiation close to cut-off frequency [131]. Additionally, the PMC wall suppresses the even order  $TE_{mo}$  modes, allowing the propagation of the second mode  $TE_{30}$  to propagate and thus increasing the uni-modal operation of the guide. Controlling the uni-modal bandwidth of HMSIW is further investigated by making use of loading the open-ended wall with electronic bandgap structures [133, 134], and lumped components [135]. Halving the width of the SIW line further reduces the transmission loss due to the reduced metallic and dielectric interface. Quarter-mode SIW (QMSIW) is presented to further reduce the SIW's width by 75 % and is used in several filters and antenna implementations. Afterwards, further miniaturization is

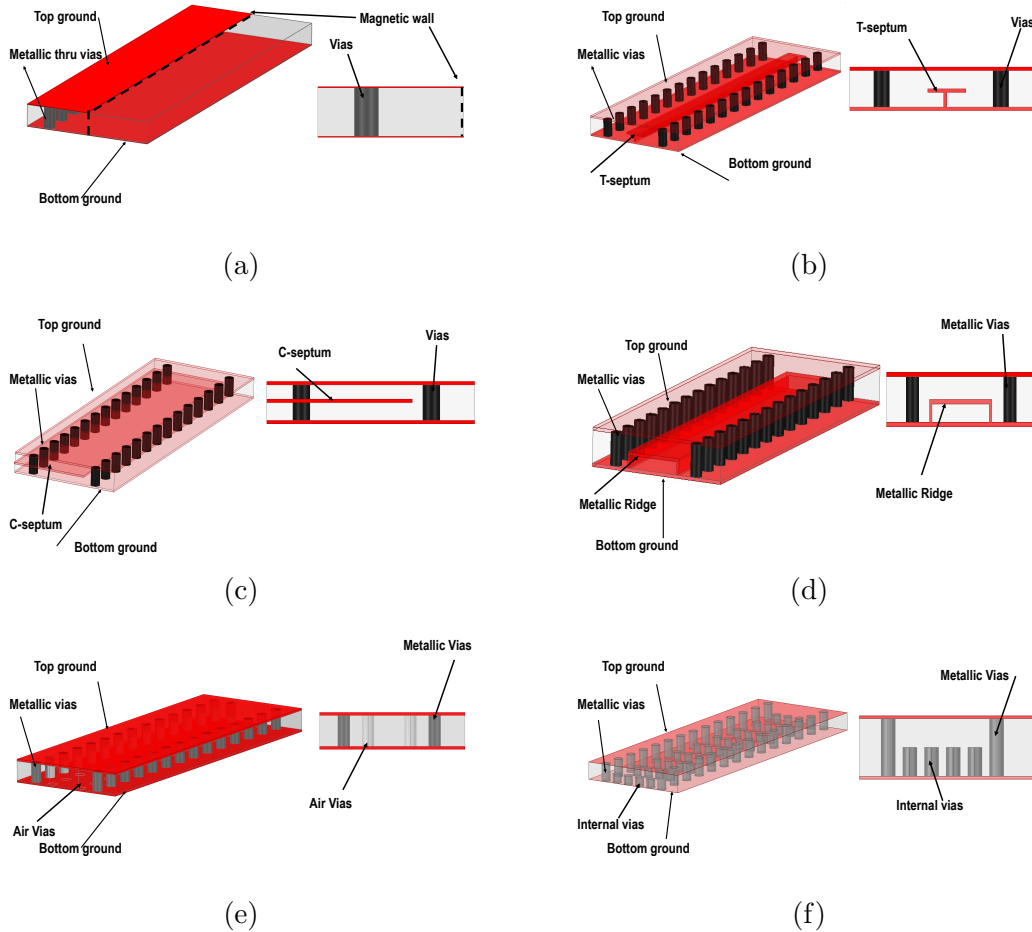


Figure 5.2: SIW modified versions a) Sub-mode SIW b) T-FSIW c) C-FSIW d) RSIW e) SISW f) Slow-wave SIW

developed, such as one-eighth-mode SIW (EMSIW). Shielding techniques have also recently been applied to the QMSIW cavity to improve radiation losses.

### Folded SIW (FSIW)

The folded substrate integrated waveguide (FSIW) [136] is a typical SIW line, in which a folded metallic septum is immersed to form either a T or C shape, halving the width of the SIW line, presented in Fig.5.2 (b),(c), respectively. Therefore, the  $TE_{10}$  is folded in two or

more substrates, maintaining the  $TE_{10}$  mode. Miniaturizing the SIW by folding has the advantage of preserving the shielding characteristics of SIW at the expense of using three or more metal layers. Accordingly, the ohmic losses are almost comparable to the SIW. Several applications incorporated FSIW, such as filters and couplers.

### **Ridge substrate integrated waveguide (Ridge SIW)**

The substrate integrated ridge waveguide (ridge SIW) is composed of a SIW line, along with a ridge implemented using a lateral row of blind vias in the middle of the waveguide [136–138], as shown in Fig.5.2(d). The ridge SIW is accordingly constructed in three metallic layers and is implemented to increase the unimodal operation of the SIW by decreasing the cut-off frequency of the fundamental  $TE_{10}$  mode. The ridge SIW's width is narrower than SIW's width for specific cut-off frequencies. However, ridge SIW presents more transmission losses due to the increased metallic losses of the ridge.

### **Substrate integrated slab waveguide (SISW)**

The substrate integrated slab waveguide [139, 140] consists of a typical SIW line, in which air vias are introduced in SIW's lateral sides, as shown in Fig.5.2(e). Air vias alter the effective dielectric constant of the substrate at the SIW's edges, which increases the unimodal operation of the SIW without changing the fundamental mode of operation.

### **Empty SIW(ESIW)**

The Empty SIW (ESIW), or hollow SIW, air-filled SIW, or dielectric-less SIW, is a SIW line hollowed from the dielectric substrate [95, 141–144] to reduce the dielectric losses in SIW and increase the quality factor of ESIW. However, the empty SIW has a drawback of larger dimensions than SIW and potentially limited bandwidth.

### **Slow wave SIW**

The slow-wave technique is incorporated with SIW to reduce the transverse and longitudinal dimensions of SIW [145, 146]. Slow-wave SIW is composed of three metallic layers, where an array of blind vias, inductive posts or iris filters are integrated with the SIW structure, as shown in Fig.5.2(f). Using the same substrate, slow-wave SIW structures are characterized by increased effective permittivity and reduced dimensions compared with

SIW. Loading SIW with reactive elements [147, 148], periodic [149, 150], and non-periodic patterns [151] is investigated as possible solution to produce extreme reduction in slow-wave SIW, while preserving its performance [147–150]

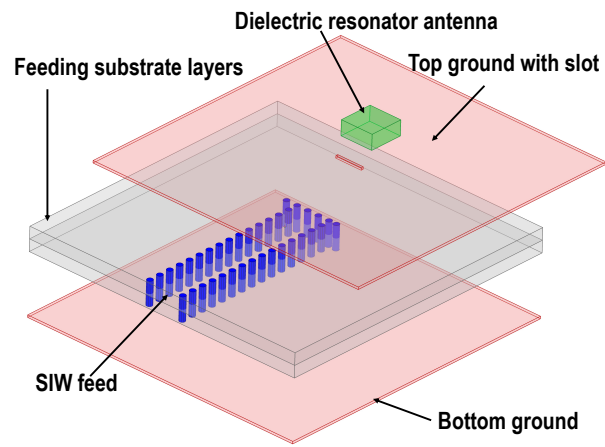
Several published works combine two or more of the mentioned techniques to improve the performance of the SIW further. One notably technique combines the slab SIW and the ridge SIW, increasing the bandwidth by altering the cut-off frequency of both the fundamental and second-order modes, respectively. Slow-wave method and sub-mode SIW is also used to form slow-wave empty SIW (SW-ESIW) [152]

## 5.2 Ka-band SIW-fed DRA Design

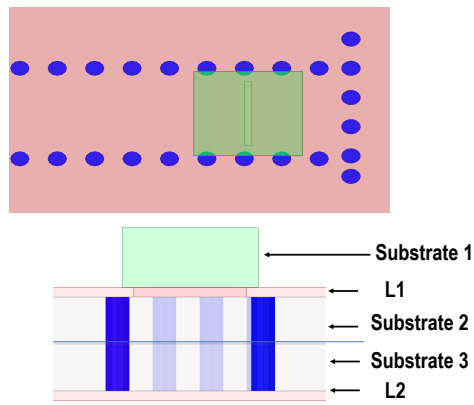
The geometry of the proposed DRA antenna, integrated with SIW feed, is shown in Fig. 5.3. The design constitutes three substrate layers. The DRA block, implemented into the first substrate, is integrated on the top conductor layer ( $L_1$ ). Whereas, two layers of 0.5 oz copper laminated substrates of a 10-mils thick RO 3006™, with dielectric constant ( $\epsilon_r$ ) of 6.15 and loss tangent ( $\tan\delta$ ) of 0.002 incorporate the SIW-feed layers. 3D-printed commercial filament, with ( $\epsilon_r$ ) of 10, is used for the DRAs. In addition to the 3D-printed DRAs, machined DRAs implemented from commercial substrates are used as a benchmark for comparison to the 3D-printed DRAs. RT/Duroid® laminates with 50-mils thickness,  $\epsilon_r$  of 10.2, and  $\tan\delta$  of 0.0023 is used for the machined  $K_a$ -band radiator.

The detailed geometrical parameters of the SIW-fed DRA are shown in the elevation view presented in Fig. 5.4. Following the same design flow mentioned in Chapter 3 and Chapter 4 for DRAs' design, the DRA is designed to excite the fundamental mode  $TE_{111}^x$  at the  $K_a$ -band (i.e., 30 GHz). It comprises of a square DRA of dimensions ( $L_{DRA} \times L_{DRA} \times h_{DRA}$ ) using a 50-mils thick Rogers/RT Duroid 6010, and aperture coupled using two-layered SIW-based slot feeding line, with width ( $W_{SIW}$ ), implemented using RO 3006™ laminates, each of 10-mils thickness.

The SIW line width ( $W_{SIW}$ ) (see Fig. 5.4) is set to 3.1 mm to enable the fundamental  $TE_{10}$  mode propagation at  $K$ -band, and the higher order mode above 36 GHz. Further, SIW line initial dimensions ( $d_{via}$ ,  $s_{via}$ ) (see Fig. 5.4) are evaluated using the analysis presented in [153] to enable unimodal operation, and to suppress the unwanted radiation. A feeding slot with dimensions of ( $L_{st} \times W_{st}$ ) is etched on the top conductor ( $L_1$ ) (see Fig. 5.4) to transfer the power from the SIW line to the DRA. The slot's dimensions and the short-circuited wall location ( $L_{Dt}$ ) (see Fig. 5.4), are the controlling dimensions to realize maximum coupling between the guiding SIW and the DRA [53]. ( $L_{Dt}$ ) is initially set to  $\lambda_g/2$ , where  $\lambda_g$  is the guided wavelength inside the SIW line [53].



(a)



(b)

Figure 5.3: Proposed SIW-fed K-band DRA. a) Exploded view b) Top and Cross-sectional views

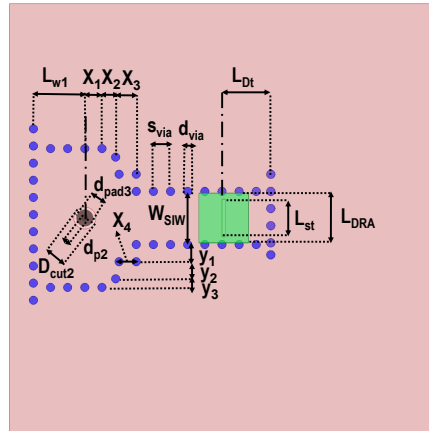


Figure 5.4: Structure of the SIW-DRA antenna.

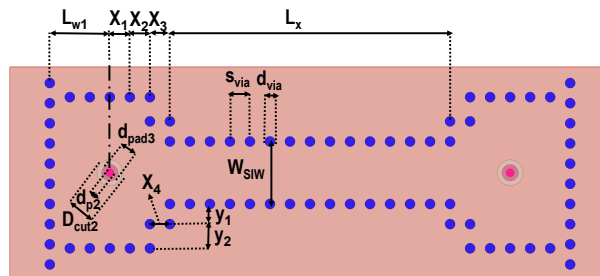


Figure 5.5: Structure of the SIW-B2B structure

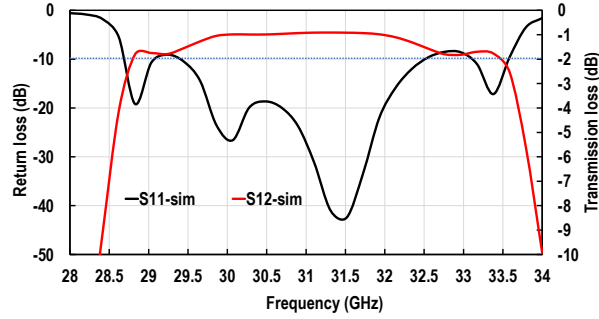
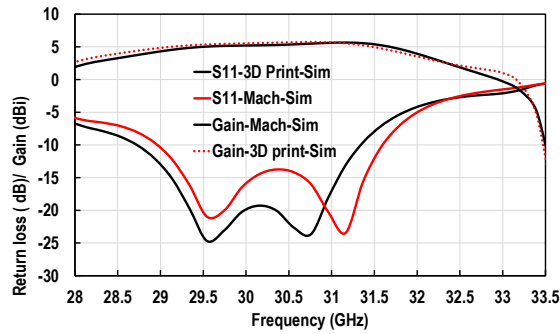
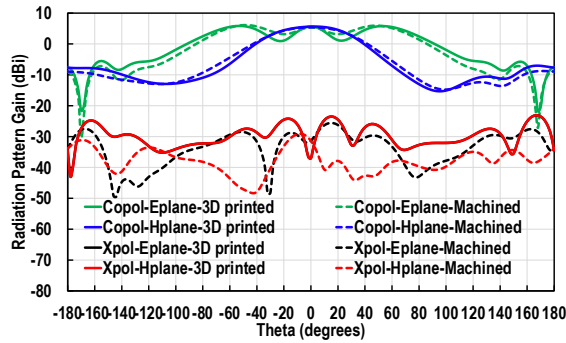


Figure 5.6: Simulation results of the B2B SIW line



(a)



(b)

Figure 5.7: Simulation results of the SIW-fed DRA: a) The S-parameters and Gain b) Radiation pattern gain

Coaxial to SIW transition is implemented for power coupling using short-circuit wall; the wall is placed at distance ( $l_{w1}$ ) from a launching metallized signal via of diameter ( $d_{p2}$ ) (see Fig. 5.4). Further, a pad/ antipad of dimensions ( $d_{pad3}$  and  $d_{cut2}$ ) are etched on ( $L_3$ ) (see Fig. 6.1 (b)) for reliable measurement to the mini connector. By optimizing ( $l_{w1}$ ,  $d_{p2}$ ,  $d_{pad3}$  and  $d_{cut2}$ ) (see Fig. 5.4), mode and impedance matching are achieved at the desired frequency. Moreover, an inductive step iris is performed at the transition to improve matching. Further, an equivalent B2B test structure of the SIW to coaxial transition, of length 20 mm is designed to test its performance as shown in Fig.5.5. Final optimized parameters of the SIW-fed DRA and the B2B test structure of the SIW to coaxial transition, are listed in Table 5.1, and Table 5.2, respectively.

Regarding the 3D-printed DRA. A model is implemented, considering the effect of the attached sheet and the electrical properties of the used filament. Simulation results of both the designed B2B test structure and the SIW-fed DRA are presented in Fig.5.6, and Fig.5.7, respectively. Both the back-to-back SIW and the SIW-fed DRA are delivering a good performance. The back-to-back structure presents a low transmission loss of 0.45 dB and a 10-dB return loss from 29.8 to 32 GHz. The SIW-fed machined DRA shows an impedance bandwidth of 2.64 GHz from 28.96 to 31.6 GHz, with a peak, realized gain of 6.2 dBi. Further, the comparison between the simulated DRA model and the 3D printed DRA shows an almost good agreement regarding the operating band. Additionally, the cross-polarization level is better than -35 dB in the boresight direction in both E- and H-planes for the machined and 3D printed DRA models.

Table 5.1: Geometrical dimensions of the SIW-DRA antenna in (mm)

$L_{st}$	$L_{DRA}$	$L_{Dt}$	$L_{w1}$	$W_{SIW}$	$D_{cut2}$	$d_{pad3}$	$d_{pin}$	$d_{via}$
2.2	2.9	2.75	3	3.1	1.29	0.97	0.381	0.5
$S_{via}$	$X_1$	$X_2$	$X_3$	$X_4$	$Y_1$	$Y_2$	$Y_3$	
1	1	0.8	1.2	1	1	1	0.5	

Table 5.2: Geometrical dimensions of the SIW-B2B structure in (mm)

$L_x$	$L_{w1}$	$W_{SIW}$	$D_{cut2}$	$d_{pad3}$	$d_{pin}$	$d_{via}$
1.4	3	3.1	1.29	0.82	0.381	0.5
$S_{via}$	$X_1$	$X_2$	$X_3$	$X_4$	$Y_1$	$Y_2$
1	1	1	1	1	1	1.2

### 5.3 Simulation versus Measurement Results

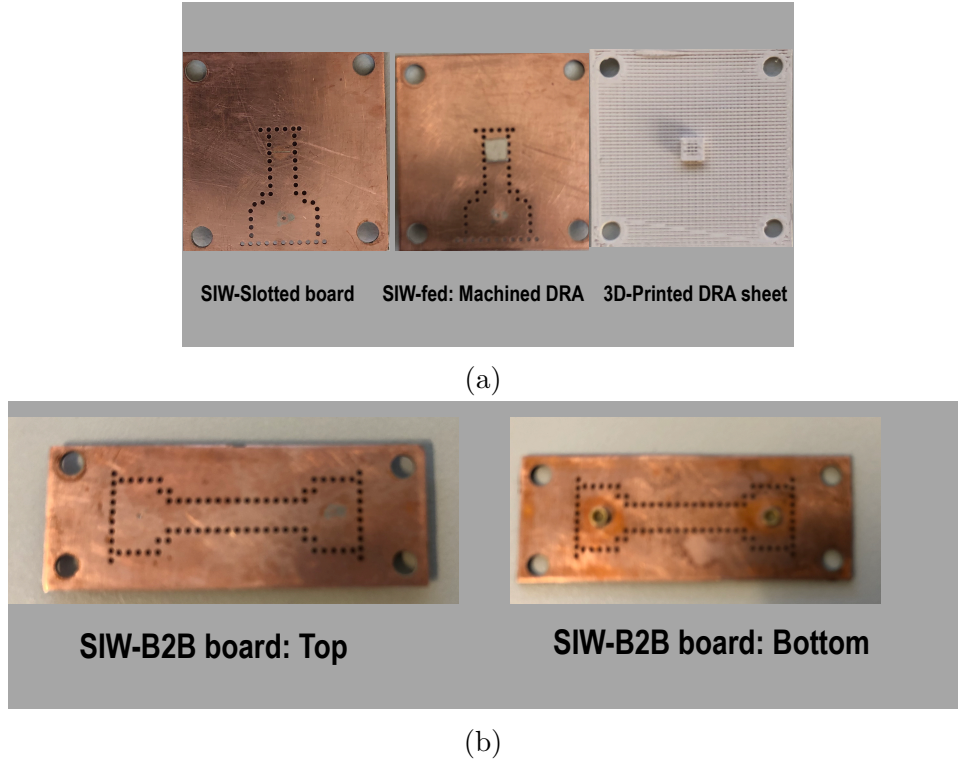


Figure 5.8: Fabricated PCB boards a)  $K_a$ -band antenna boards b) B2B circuit boards

A top-view photograph for the fabricated PCB and the 3D-printed DRA antenna are shown in Fig. 5.8 (a). Mini-coaxial surface mount RF connectors from southwest microwave Inc. [107] are soldered on the back of the fabricated board to feed the antenna and circuit boards. Moreover, the designed B2B test structure of the coaxial to SIW transition to characterize their transition loss is shown in Fig.5.8 (b). The reflection coefficient for the antenna boards is measured using Keysight VNA to identify the measured center frequencies; then, the radiation pattern measurements are performed using the planar near-field measurement system (NSI) [108].

### 5.3.1 S-parameters

The simulation versus measurement results for the reflection coefficient of the machined and 3D-printed  $K_a$ -band SIW-fed DRAs are illustrated in Fig. 5.9. The simulated and measured reflection coefficient of the machined DRA show close agreement in terms of the number of minima. The -10-dB impedance BW is 2.6 GHz (29-to-31.6 GHz), 2.2 GHz (30.5-to-32.7 GHz), and 2.3 GHz (30.7-to-33 GHz) for the simulated, machined, and 3D-printed DRAs, respectively. A greater frequency offset occurs with SIW-fed DRAs than with the presented SICL-fed machined and 3D-printed DRA.

The B2B 20-mm long test structure of the designed vertical coaxial to SIW transition is measured to capture the effect of the measured frequency offset. The measured IL and RL are compared to their simulated counterparts as shown in Fig. 5.10 (a) and Fig. 5.10 (b), respectively. The SIW transition experiences a measured average (IL) of 0.6 dB/cm over the operating band from (31-to-32.8 GHz) versus an average simulated IL of 0.45 dB/cm over the operating band from (29.8-to-32 GHz). The measured 10-dB RL bandwidth is 4.4 GHz over the band from (30.5-to-34.9 GHz) versus a simulated bandwidth of 3.7 GHz from (28.8-to-32.5 GHz).

A sensitivity analysis is performed to diagnose the frequency offset for the SIW-B2B test structures. The deviation is caused by the bonding thickness tolerance between the two substrate layers. A 5- $\mu\text{m}$  thick adhesive layer is used for bonding the two substrate layers, which isn't sufficient to ensure complete lamination of the two layers. Fig. 5.11 shows the simulated IL due to different air gap thicknesses (created by incomplete lamination). A 10- $\mu\text{m}$  thick air gap caused a deviation in the operating band by 6.7 % due to the change in the effective  $\epsilon_r$  of the whole stack up.

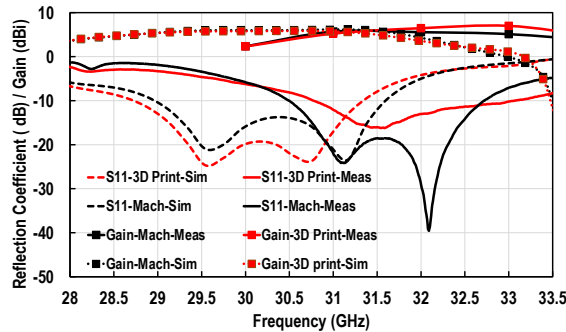
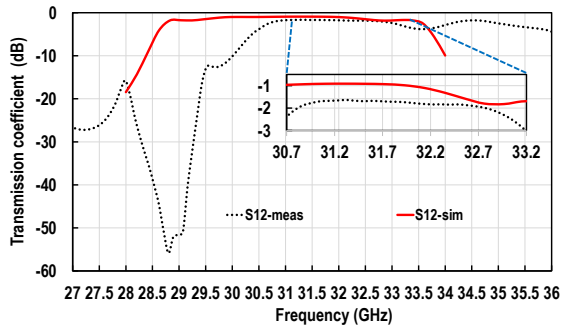
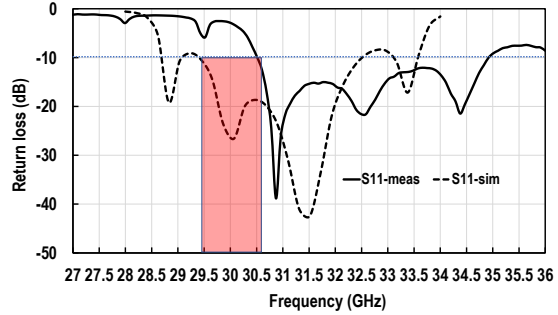


Figure 5.9: SIW-fed DRA: Measured Vs simulated reflection coefficient and gain



(a)



(b)

Figure 5.10: SIW-back to back transition: Measured Vs simulated S-parameters

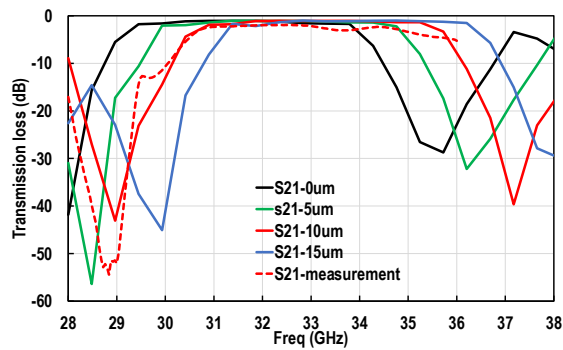


Figure 5.11: Parametric analysis of gap effect on the SIW-back to back transition

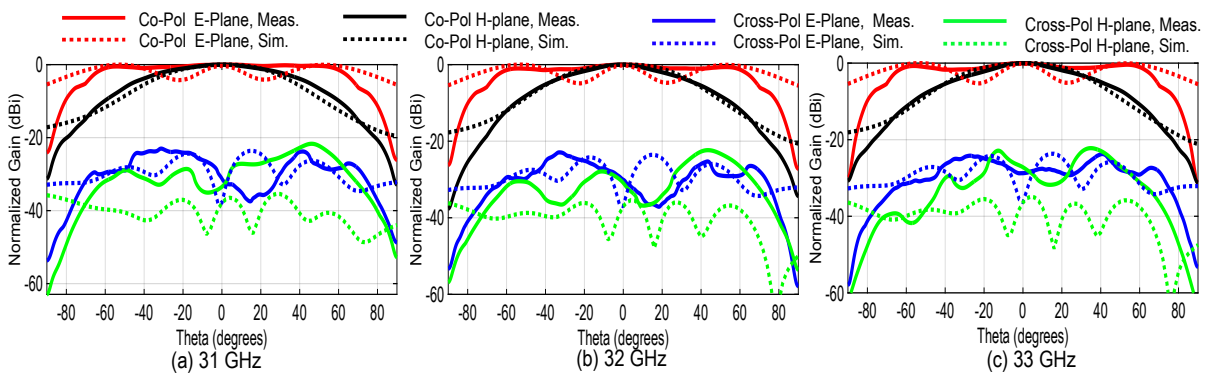


Figure 5.12: Measured vs simulated normalized radiation patterns for the 3D-printed Ka-band antenna

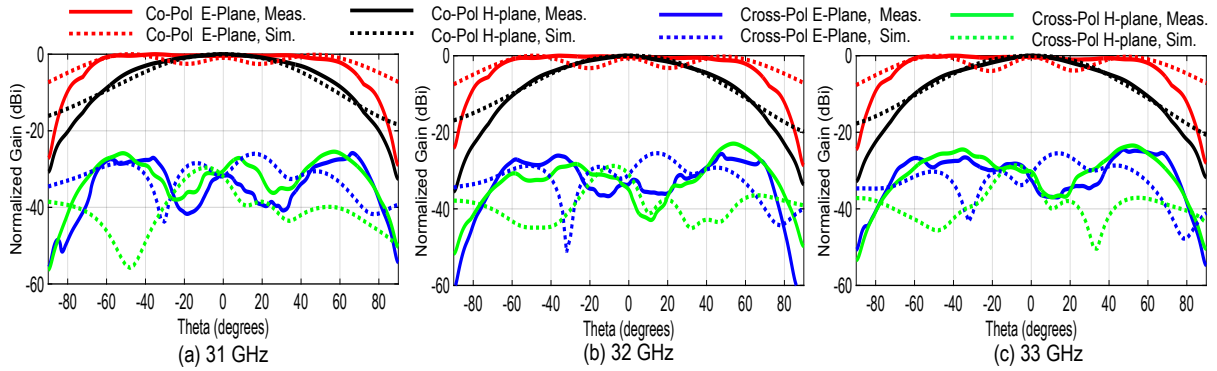


Figure 5.13: Measured vs simulated normalized radiation patterns for the machined Ka-band antenna

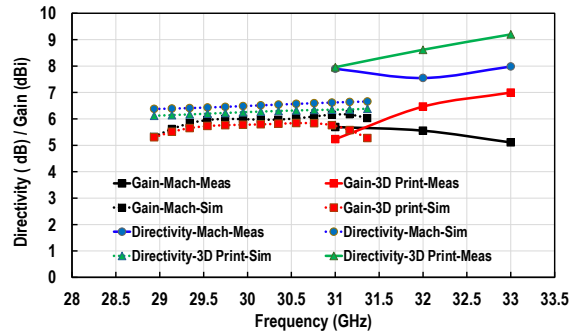


Figure 5.14: Measured vs simulated realized gain and directivity of the  $K_a$ -band DRAs

### 5.3.2 Radiation Pattern Gain

The simulated and measured realized gains for the machined and 3D-printed  $K_a$ -band DRA are demonstrated over their operating bandwidth as shown in Fig. 5.9. The average simulated realized gain is 5.9 dBi for the  $K_a$ -band machined DRA (see Fig. 5.9), with almost similar performance for their 3D-printed versions. The measured results present an excellent agreement taking into account the possible estimation error in the near field measurement of the gain [109]. The measured normalized radiation patterns in the E- and H-plane are presented for the 3D-printed and machined DRAs at  $K_a$ -band DRA) in Fig. 5.12 and Fig. 5.13, respectively. Measurements across three different frequencies depict stable radiation patterns. Besides, the measured co-polarization level is at least 30 dB more than the cross-polarization level in the boresight direction. For the 3D printed SIW-fed DRA, the measured cross-polarization level is lower than -32.5 dB, -30 dB, -27.5 dB at 31 GHz, 32 GHz, and 33 GHz, respectively, at the boresight direction. For the machined SIW-fed DRA, the measured cross-polarization level is lower than -25 dB, -33 dB, and -31.2 dB at 30 GHz, 32 GHz, and 33 GHz, respectively, at the boresight direction. Fig. 5.14 presents the maximum realized gains and directivities of the  $K_a$ -band DRA. The effect of imperfect lamination decreased the realized efficiencies as compared to the simulations.

## 5.4 Sensitivity Analysis of Design Parameters

Full-wave simulations are performed to observe the tolerance of the antenna dimensions on the antenna performance, presented in Appendix B. The sensitivity analysis is performed by considering a possible 2 mils oversize in the design dimensions after manufacturing. The effect of the slot dimensions ( $L_{St}$ ,  $W_{Slot}$ ) on the reflection coefficient characteristics are plotted in Fig. B.1, showing a minimal effect on the reflection coefficient characteristics. Further, the variation of the quasi-coaxial SIW transition parameters is plotted in Fig. B.2, from which a change in the pad and pin diameters can cause a slight change in response while preserving the achieved bandwidth. The effects of the short circuit walls of both the DRA and the transition and the iris width are demonstrated in Fig. B.3. The reflection coefficients show stable performance for all tuned parameters. Additionally, the variation of the DRA's dimensions on the reflection coefficient characteristics is plotted in Fig. B.4. Change in DRA's dimensions can alter the resonant frequency, but this tolerance is more prominent in machined DRAs than in 3D-printed DRAs. To conclude, the design parameters are insensitive to manufacturing tolerance.

## 5.5 Conclusion

A substrate integrated waveguide (SIW)-fed Dielectric Resonator Antenna was presented in this Chapter. The SIW line is performed in two substrate layers. Full-wave simulations present a reflection coefficient bandwidth ( i.e.,  $S_{11} < -10$  dB) of 2.6 GHz . The design concept of the SIW-fed DRA element in two substrate layers is aimed to be integrated into a shared-aperture array. The proposed SIW-integrated DRA was manufactured using 3D printing and low-cost PCB technology. The measured results agree well with the simulated ones regarding the number of nulls. The operating bandwidth is slightly affected due to manufacturing tolerance.

# Chapter 6

## *K*-/*K<sub>a</sub>*-bands Shared-Aperture Array

This chapter presents a *K*-/*K<sub>a</sub>*-bands shared-aperture array with high isolation between both bands using DRAs, that can be further scaled for phased array applications. The scope of the design is to develop a shared-aperture that can independently operate at both bands (i.e. *K*-/ *K<sub>a</sub>*-) with satisfactory isolation. Moreover, several considerations are maintained to provide low profile implementation, a compact footprint for the Rx feed network, and ease of manufacturing. Based on the required specifications for mm-wave applications, DRAs are selected for shared-aperture implementation. The minimum specified isolation to fulfill full-duplex operation is 50 *dB*. Further, DRAs should provide a minimum of 2 GHz of operating bandwidth, and a cross-polarization level of more than 25 dB. The proposed shared-aperture design procedure is outlined as follows. Firstly, the DRAs' configuration and design principles are presented. Secondly, the *K*- and *K<sub>a</sub>*-bands DRAs introduced in Chapter 4 and Chapter 5 are integrated into a shared-aperture configuration, and optimized to fulfill the design goals. The concept of the proposed shared-feed network is summarized. Afterwards, a summary of the *K<sub>a</sub>*-band combiner network's design procedure is then outlined. Thirdly, the 3D-printed material characterization and fabrication are highlighted, followed by the simulation and measurement results. Finally, a comparison between the state-of-art shared-aperture array will conclude the chapter.

### 6.1 Introduction

The recently growing demand for high data rates and low-cost communication systems has pushed towards highly integrated multifunctional, low profile, and cost-effective wireless

transceivers in the millimetre-wave (mm-wave) band. In this context, the SATCOM phased array system operating at  $K$ -/ $K_a$ -bands provides a much larger bandwidth, higher antenna gain, and substantially reduced antenna size [15], as highlighted in Chapter 1. Despite the advances of integration in RF integrated circuits (ICs), the transmit and receive antennas are split into separate boards, which inherently hinder the possibility of low-cost solutions for mass production. Thanks to the shared-aperture antenna concept, where two or more radiators, operating at different frequency bands, can be placed on the same physical aperture [4, 38, 41, 44, 45, 48, 154–156]. This allows to efficiently utilize the aperture space and reduce the system’s overall cost and volume. Accordingly, shared-aperture arrays have recently become an attractive topic in wireless applications, which require simultaneous operation at multi-frequency bands such as satellite communication, and radar applications [44].

Aperture sharing can be configured in different forms: interlaced [4, 32, 34, 48], stacked [156–158], and perforated [4, 36, 38, 39]. Perforated structure enables fitting of high-band radiators within perforations in the low-band radiators [36]. Thus, it is suitable for radiators with a large frequency ratio. Stacked configuration suffers from higher cross-polarization, and complex feeding mechanism [44]. However, interlaced configuration offers design flexibility by independently placing the radiators in the aperture of the array [4]. Achieving high isolation between channels and independently controlling the performance of the radiators are common challenges in the design of shared-aperture arrays. Further, the frequency ratio between the radiators presents a constraint in achieving the required specifications. Few designs have been reported for mm-wave shared-aperture array, specifically at  $K$ - and  $K_a$ -bands, with sufficient isolation, good radiation characteristics, and compatibility with planar arrays’ integration as elaborated in Chapter 2. Accordingly, dielectric resonator antennas (DRAs) are proposed in a shared-aperture interlaced configuration.

DRAs are considered wideband, highly efficient radiators for mm-wave systems due to their ease of integration with planar circuits, absence of conductor loss compared to metallic radiators, and most importantly, their design flexibility [52, 53] as discussed in Chapter 3. Despite the reported advantages of DRAs, little practical work has been reported due to the difficulty of machining and proper alignment of the DRAs. A template has been suggested in [159–161] for accurate placement of DRAs. However, this method is not efficient in large DRA array implementations. Further, mm-wave DRA machining is challenging due to its miniature dimensions. 3D-printing technology is promising for microwave dielectric applications [162, 163] as it enables the design of unique dielectric antenna shapes with accurate dimensions. Accordingly, 3D-printed DRAs in shared-aperture array configuration are presented in this thesis. Preliminary analysis for using DRA in shared-aperture configuration is presented in Chapter 3.

Table 6.1: Target specification for shared-aperture array

	$K$ -band	$K_a$ -band
Polarization	Linear	Linear
Bandwidth	2 GHz	2 GHz
Isolation	>50 dB	> 50 dB
Cross-polarization level	>25 dB	>25 dB

Several strategies are implemented in this work to achieve high isolation between the DRAs operating at  $K$ - and  $K_a$ -bands and maintain sufficient operating bandwidth and low cross-polarization level. Firstly, the relative alignment of radiators is based on the field distribution that enables reduced coupling at both bands. Secondly, the substrate integrated technologies: substrate integrated waveguide (SIW) and substrate integrated coaxial line (SICL) are incorporated as feeding networks for the  $K_a$ - and  $K$ -band radiators, respectively. Thus, the corresponding supported modes (i.e.,  $TE_{10}$ , and  $TEM$ ) further improve the isolation between both bands. Besides, orthogonal polarization between the DRAs maintains sufficient cross-polarization and optimum isolation between both bands. Lastly, the SIW and SICL networks are implemented in three metallic layers only, where the SIW network shares two substrate layers with the SICL line. Thus, the fabrication process enables low-profile implementation by removing buried vias. The standalone antenna designs (i.e., SICL-fed  $K$ - band DRA and SIW-fed  $K_a$ -band DRA) are presented in Chapter 4 and Chapter 5.

## 6.2 Shared-aperture Array Configuration

The desired design specification for the shared-aperture array is presented in Table 6.1. 48-dB isolation for shared-aperture of full-duplex SATCOM transmit/receive channels is required to satisfy the required system of merit for satellite communication (G/T), where G is antenna gain, and T is the equivalent noise temperature [48]. The target operating bandwidth of the array is 2 GHz ( $K_a$ -band) and 2 GHz ( $K$ -band) for the transmit and receive modes, respectively, based on the expected achievable performance of the DRAs in mm-wave frequencies. In this section, the configuration of the proposed sub-array and its principle of operation are presented.

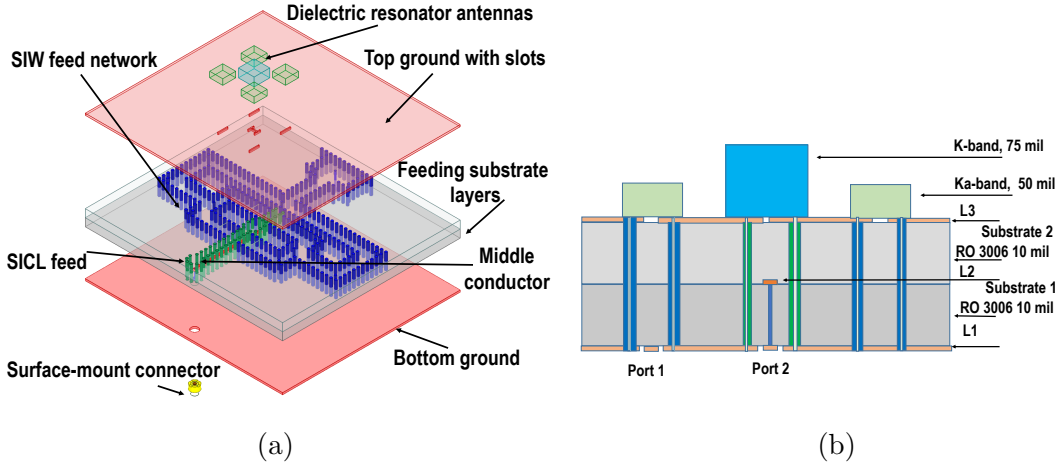


Figure 6.1: Proposed shared-aperture DRA sub-array. (a) Exploded view (b) Cross-sectional view

### 6.2.1 Sub-Array Configuration

The 3D geometry of the proposed shared-aperture sub-array is presented in Fig. 6.1 (a). The stackup used in the design is composed of three-conductor layers (see Fig. 6.1 (b)). Two layers of 0.5 oz copper laminated substrates of a 10-mils thick RO 3006™, with dielectric constant ( $\epsilon_r$ ) of 6.15 and loss tangent ( $\tan\delta$ ) of 0.002 are used as the substrate layers. Featuring high ( $\epsilon_r$ ), the adopted substrate enables compact implementation of feeding structures. A very thin epoxy layer bonds the two layers. 3D-printed commercial filament, with ( $\epsilon_r$ ) of 10, is used for the DRAs. In addition to the 3D-printed DRAs, machined DRAs implemented from commercial substrates are used as a benchmark for comparison to the 3D-printed DRAs. Thus, the DRA design parameter (i.e., height) is selected to compare the standard laminates' thickness options. RT/Duroid® laminates with 50-mils/ 75-mils thickness,  $\epsilon_r$  of 10.2, and  $\tan\delta$  of 0.0023 are used for the machined  $K_a$ -/  $K$ -band radiators, respectively. The sub-array is composed of one  $K$ -band element interlaced within four  $K_a$ -band radiators. The separation between the  $K_a$ -band elements is limited to  $0.7 \lambda$  to accurately fit the  $K$ -band element and its associated feeding network.

### 6.2.2 Principle of Operation

The  $K$ - and  $K_a$ -band elements are vertically and horizontally polarized to excite the fundamental  $TE_{111}^y$ , and  $TE_{111}^x$  modes, respectively. The effect of relative location and orientation

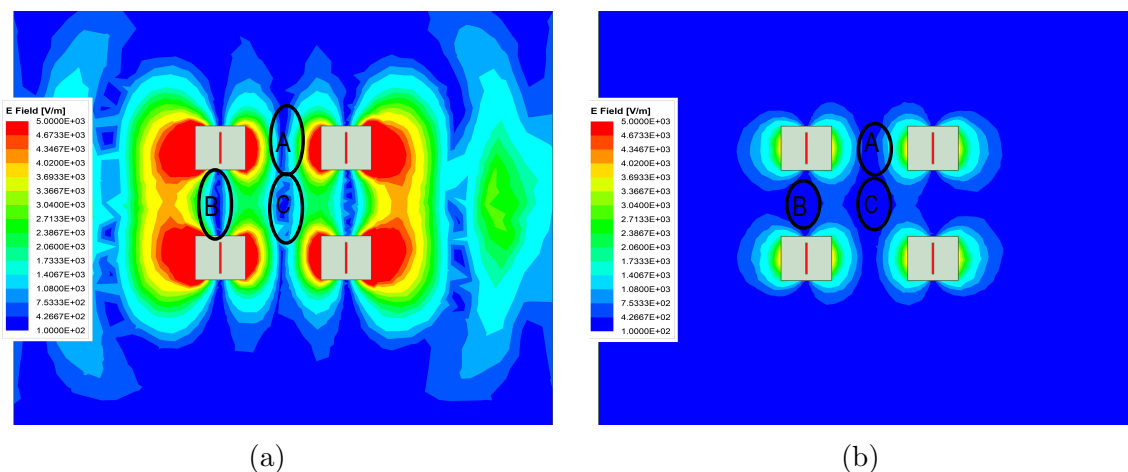


Figure 6.2: Electric field distribution when  $K_a$  band DRAs excited a) 30 GHz b) 20 GHz

of the radiators operating at  $K$ - and  $K_a$ -bands on their isolation have been investigated in Chapter 3. Another approach is presented in this section based on mapping E-field distribution to expand on the analysis of the relative location of the DRAs. In the design of the shared-aperture, high isolation is required to mitigate the receiver desensitization by the large transmitter power [48]. The  $K$ -band element should be placed in a weak field region with respect to the E-field distribution of the  $K_a$ -band array to minimize the coupling between them. Thus, the isolation between the elements is improved. Fig. 6.2 (a and b) represents the E-field distribution for the  $2 \times 2$   $K_a$  sub-array, when the four radiators are simultaneously excited at the fundamental  $TE_{111}^x$ , at both 30 GHz and 20 GHz, respectively. Comparing the three potential regions (A, B, C), region A is typically avoided as the electric field intensity of the  $K_a$ -band radiators is vital. However, both regions B, C provide the optimum relative positions, where the electric field of the  $K_a$ -band is at its minimum intensity. Along the H-plane of the  $K_a$ -band radiators, Region B provides the maximum isolation between radiators, but with a higher cross-polarization level than region C, which provides a balanced trade-off between isolation and cross-polarization level. Further, the selection of region C simplifies the feed network design.

### 6.2.3 Integration Feeding Technologies

The two shielded feeding structures (SIW/ SICL) are incorporated for the ( $K_a$ -/  $K$ -) DRAs. Among the different reported feeding techniques used with DRAs, aperture coupling is promising in the mm-wave range for ease of fabrication [53]. In addition, SIW

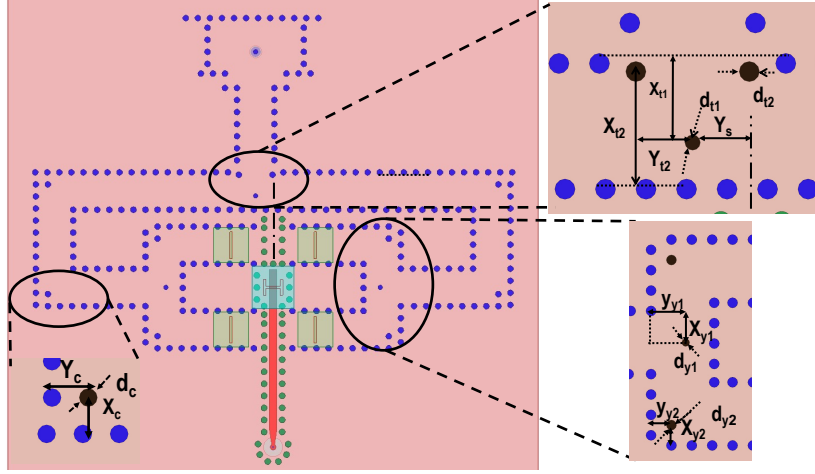


Figure 6.3: Geometry of the proposed shared-aperture

technology is capable of providing high radiation efficiency with DRA integration while reducing crosstalk and interference from adjacent lines due to their shielded structure [53]. Alike the SIW, the SICL, introduced in [23] as the planar coaxial line, is composed of two rows of conducting vias embedded in two grounded substrate layers, in addition to a middle conductor that provides the  $TEM$  mode for the SICL. Thus, the two shielded feeding structures (SIW, SICL) are selected to support two orthogonal modes of operation ( $TE_{10}$  and  $TEM$ ), which accordingly improves the isolation. Further, SICL features a compact footprint in comparison with the SIW line. Therefore, the SICL is used to design the  $K$ -band antenna to reduce the feeding network size, as mentioned in the design goal for  $K$ -band DRA in Chapter 4. The SIW is used to feed the  $K_a$ -band to provide an extra isolation element as the SIW line operates after a predetermined cut-off frequency. Thus, this strategy prevents the  $TE_{10}$  mode propagation in the  $K$ -band. Further, the concept of SIW walls sharing with the SICL line is introduced, enabling space utilization for shared-aperture arrays. The designed  $K$ -band SICL fed DRA and the  $K_a$ -band SIW fed DRA are presented in Chapter 4 and Chapter 5.

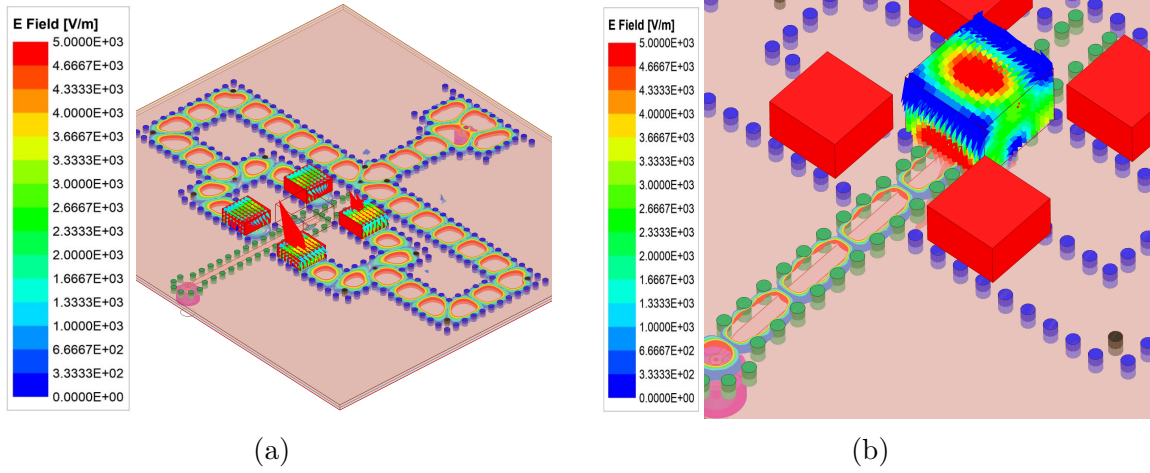


Figure 6.4: Field distribution in the shared-aperture sub-array (a)  $K_a$ -band array excited, with  $K$ -band match-loaded (b)  $K$ -band excited, with  $K_a$ -band match-loaded

### 6.3 $K_a$ -band Feeding Network and Shared-aperture Configuration

The configuration of the shared-aperture sub-array is shown in Fig. 6.3. The sub-array consists of four SIW-fed  $K_a$ -band DRAs and a SICL-fed  $K$ -band DRA interlaced in the center. Both the SIW and the SICL-feed share two layers of the substrates. The design parameters of both antennas are optimized to achieve impedance matching bandwidth of 2 GHz and isolation (ISO) better than 50 dB between both bands. Further, an improved shared feeding structure is introduced, where the SIW short-circuited wall is shared with the SICL line as shown in Fig. 6.3. The four short-circuited SIW sections are combined to form a  $2 \times 2$  sub-array feeding network. The feed network comprises T- and Y-junctions connected via two corner junctions. Matching vias are embedded in each junction to provide equal power splitting and suppress discontinuities reflections. To achieve the proper phase requirement for the  $K_a$ -band antennas ( $180^\circ$ ), different path lengths of the SIW are incorporated in the two branches. Balanced branches with impedance matching characteristics ( $S_{11} < -15\text{dB}$ ) for each section are implemented by varying the diameter and location of the matching vias. Then, the  $180^\circ$  compensation is achieved by changing the relative path lengths of the SIW lines in the two branches (i.e., optimizing  $Y_s$ ). The parameters of the feed network are listed in Table 6.2.

Table 6.2: Geometrical dimensions of the shared-aperture feeding network in (mm)

$d_c$	$d_{y2}$	$d_{t2}$	$d_{y1}$	$d_{t1}$	$X_c$	$Y_c$	$X_{y2}$	$Y_{y2}$	$X_{t2}$	$X_{t1}$	$X_{y1}$	$Y_{y1}$	$Y_{t2}$	$Y_s$
0.5	0.5	0.5	0.381	0.381	1	1	1	1	2.9	1.95	1.55	1.7	1.4	1.45

### 6.3.1 Shared-aperture Simulation Results

Full-wave simulations are performed to verify the proposed design. The E-field distributions for two cases: 1)  $K_a$ -band array excited ( $K$ -band DRA match loaded), and 2)  $K$ -band DRA excited ( $K_a$ -band array match loaded) are presented in Fig. 6.4 (a) and (b), respectively. The E-field distribution of the DRAs presents the dominant radiating mode of both the  $K_a$ - and  $K$ -band, along with the field distribution of both  $TE_{10}$  and  $TEM$  methods in the SIW feed network and the SICL line, respectively. It can be deduced that the DRAs are operating efficiently at their corresponding bands, with sufficient isolation between both operating modes. For the 3D-printed DRA, a thin 3D-printed sheet is designed and attached to the DRA for accurate alignment. The attached sheet's electromagnetic (EM) effect is captured in a separate 3D-printed DRA model based on the associated filament electrical properties.

#### Near-field simulation results

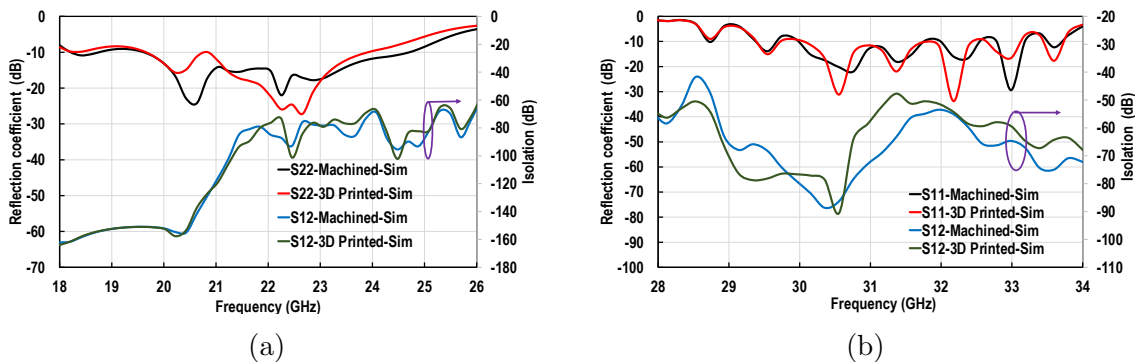


Figure 6.5: Simulated S-parameters of the shared-aperture sub-array:(a)  $K$ -band (b)  $K_a$ -band

The reflection coefficient (i.e., S11) and the isolation (ISO) (i.e., S12) for the 3D-printed and machined DRA models, at  $K$ - and  $K_a$ -bands are plotted in Fig. 6.5 (a) and (b), respectively. The simulated  $K$ -band machined antenna has a -10-dB impedance

bandwidth (BW) (i.e.,  $S_{11} < -10$  dB) of 5.1 GHz from 19.6-to-24.7 GHz (see Fig. 6.5 (a)). The 3D-printed model presents a -10-dB impedance BW of 4.27 GHz from 19.65-to-23.92 GHz. The average simulated ISO between the two ports over the operating frequency band at the  $K$ -band is better than 80 dB, for the machined and the 3D-printed DRA, with a worst-case value for the ISO at 24 GHz of 68.8 dB for the machined DRA, and 67.4 dB for the 3D-printed DRA. At the  $K_a$ -band, the reflection coefficient has slight peaks above the -10 dB level due to feeding network size. The simulated -8-dB impedance BW (i.e.,  $S_{11} < -8$  dB) is 4 GHz from 29.3-to-33.3 GHz, and the -10-dB impedance BW within frequency ranges: 29.9-to-31.76 GHz, 31.99-to-32.56 GHz, and 32.78-to-33.2 GHz for the  $K_a$ -band machined array (see Fig. 6.5 (b)). The 3D-printed array presents a -8-dB impedance BW of 3.88 GHz from 29.32-to-33.2 GHz and a -10-dB impedance BW within frequency ranges: 30.02-to-32.52 GHz, 32.62-to-33.13 GHz, and 33.44-to-33.73 GHz. At the  $K_a$ -band, the average ISO between the two ports is better than 50 dB for machined and 3D-printed sub-arrays, with a worst-case value for the ISO of 53.7 dB at 32 GHz for the machined DRAs, and 47.6 dB at 31.37 GHz for the 3D-printed DRA. The high ISO at the  $K$ -band is due to the filtering nature of the SIW line. Thus, there is no propagation for the  $TE_{10}$  mode at the  $K$ -band. Further, the proper location of the DRAs and the orthogonal polarization contributed to the isolation achieved at the  $K_a$ -band.

## Far-field simulation results

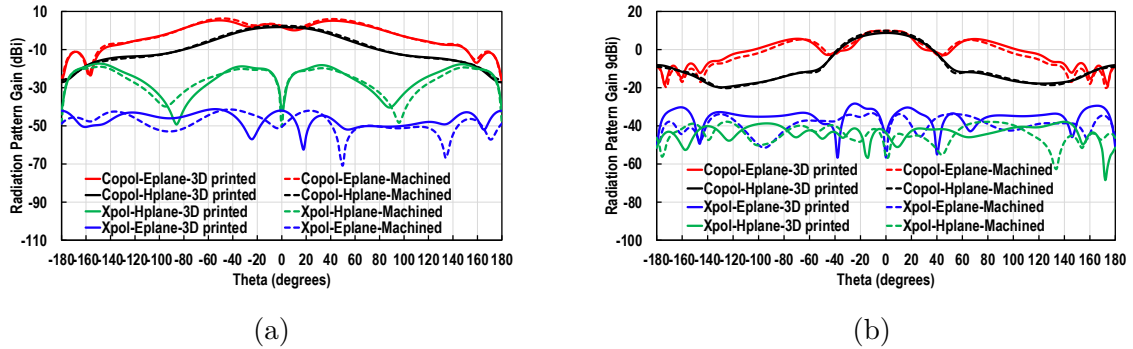


Figure 6.6: Simulated radiation pattern gains of the shared-aperture sub-array a)  $K$ -band, b)  $K_a$ -band

The simulated radiation pattern gains for 3d-printed and machined shared-aperture array, at the  $K$ - and  $K_a$ -band are depicted in Fig. 6.6 (a) and Fig. 6.6 (b), respectively. At the  $K$ -band, the simulated peak gains are 6.3 dBi, and 5.3 dBi in E-plane for the machined

and 3D-printed DRA, respectively (see Fig. 6.6(a)). The cross-polarization level at the  $K$ -band is better than 50 dB and 40 dB at boresight direction in both E- and H-planes for the machined and the 3D-printed DRA, respectively. At the  $K_a$ -band array, the simulated peak gains of the TX array (i.e., 30 GHz) for the shared-aperture are 9.9 dBi, and 9.6 dBi for the machined and 3D-printed DRAs, respectively (see Fig. 6.6 (b)). The  $0.7\text{-}\lambda$  separation between elements, along with the small aperture size ( $2\times 2$ ), results in a sidelobe level (SLL) of 4.5 dB. The SLL can be significantly improved by increasing the number of radiators in the aperture, which can be extended in future work. Further, the cross-polarization level at the  $K_a$ -band is better than 60 dB and 50 dB in the boresight direction in both E- and H-planes for machined and 3D-printed DRAs, respectively.

## 6.4 Fabrication and Material Characterization

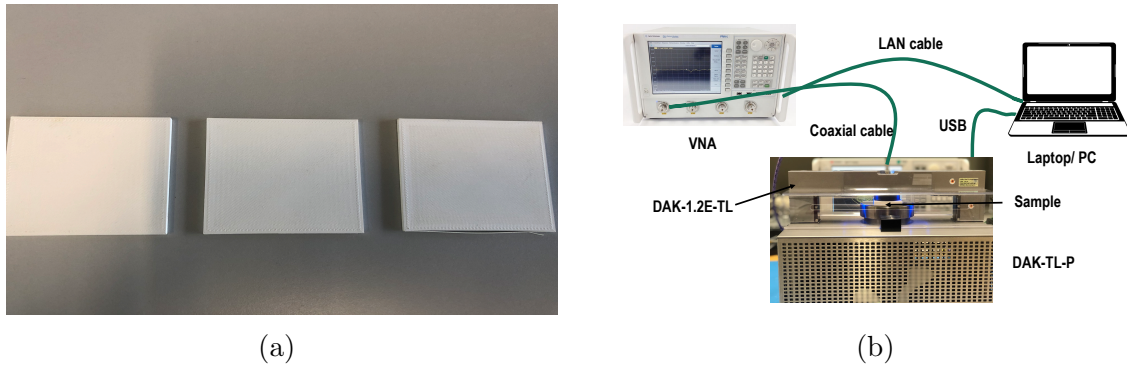


Figure 6.7: 3D-printing characterization. a) 3D-printed samples b) DAK-TL setup

The shared-aperture sub-array is fabricated using the standard low-cost Printed Circuit Board (PCB) technology and measured to verify the proposed structure. Two 10-mils double-sided RO 3006™ substrates (see Section 6.2.1), are used for the combined (SIW/SICL) structure (see Fig. 6.1 (b)). The PCB boards consist of three metal layers stack-up. The fabrication multistep process involves drilling both substrates, plating vias using the sputtering method with argon, masking and etching copper layers, attaching both substrates using epoxy glue, and alignment of both layers. For the DRA blocks, a detailed description is presented below for the implementation using machined laminates and 3D-printed materials.

### 6.4.1 Machining DRAs

The predetermined laminates (see Section 6.2.1); two-sided 50-mils and 75-mils of RT/Duroid<sup>®</sup> 6010, are used for the machined  $K_a$ - and  $K$ -band DRAs implementation, respectively (see Fig.6.1 (b)). The copper layer is etched leaving a dielectric sheet, then DRA blocks are diced according to the designed dimensions and bonded using non-conductive glue to the PCBs.

### 6.4.2 3D-printing DRAs and Material Characterization

The commercial 3D-printed machine (Raise3D PRO 2) is used to print the DRAs along with an attached sheet used for alignment, which is described in Section 6.3. The final designed DRA and sheet are exported from the full-wave simulation software to the 3D-printing software, ideamaker. The adopted ABS-based filaments are 3D-printed using the fused deposition method (FDM). The material profile is loaded, and the infill percentage that maps the required ( $\epsilon_r$ ) is assigned.

The permittivity of the 3D-printed material varies with the actual infill percentage of the material due to the inevitable presence of air voids. Thus, ABS materials are initially characterized to obtain the required ( $\epsilon_r$ ) for optimal design. Preperm<sup>®</sup> ABS1000 filament from *Premix*, with an  $\epsilon_r$  of 10, and a  $\tan\delta$  of 0.003, is used to verify the actual infill achievable versus the 100% nominal infill setting. Several square samples, (50-mm long and 2-mm high), with different printing profiles, are 3D-printed for characterization purposes (see Fig. 6.7 (a)). The permittivity and loss tangent of the 3D-printed samples are measured using the commercial coaxial probe-based system (DAK-TL) from SPEAG [164], a fully automated software-controlled system based on the open-ended coaxial probe (OCP) characterization technique [165, 166]. A vector network analyzer (VNA) is used to measure the reflection coefficient (S11) at the open end of the coaxial probe (see Fig. 6.7 (b) for the measurement setup). Measurement is performed for ( $\epsilon_r$ ) over a wide frequency range from 5 GHz to 50 GHz. The average maximum achievable permittivity using ABS1000 filament is 8.3. The exact measured permittivity is 8.33 at 20 GHz and 8.19 at 30 GHz. The average value agrees well with the results reported by [167], where a model is used to predict the actual permittivity by knowing the sample's weight and volume. Based on this analysis, a filament with a higher  $\epsilon_r$ , Preperm<sup>®</sup> ABS1200, is selected to achieve an actual permittivity of 9.9 with 100% nominal infill setting. For the  $\tan\delta$  measurement, the measured value from the manufacturer is used in the calculation as the tolerance indicated for the commercial OCP-based system is not suitable for accurate measurement of low-loss materials.

## 6.5 Simulation versus Measurement Results

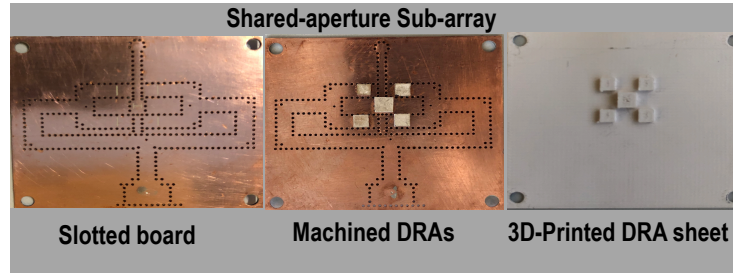


Figure 6.8: Fabricated PCB boards and 3D-printed sheets of the  $K$ -/ $K_a$ -shared-aperture

A top-view photograph of the fabricated prototypes and the 3D-printed antenna sheets is shown in Fig. 6.8. Mini-coaxial surface mount RF connectors from southwest microwave Inc. [107] are soldered on the back of the fabricated board to feed the antenna and circuit boards. Moreover, a back-to-back (B2B) test structure of the coaxial to SIW transition and the coaxial to SICL transition is designed to characterize their transition loss. The reflection coefficient for the antenna boards is measured using Keysight VNA to identify the measured center frequencies. The radiation pattern measurements are performed using the planar near-field measurement system (NSI) [108].

### 6.5.1 S-parameters

The measured reflection coefficient and ISO at both  $K$ - and  $K_a$ -band of the proposed 3D-printed and machined shared-aperture sub-array are presented in Fig. 6.10 and Fig. 6.9, respectively. At the  $K$ -band, the machined and 3D-printed DRA in the shared-aperture configuration covers a measured -10-dB impedance BW of 5 GHz (19.5-to-24.5 GHz) and 5.5 GHz (21-to-26.5 GHz) compared to a simulated -10-dB impedance BW of 5.1 GHz (19.6-to-24.7 GHz) and 4.27 GHz (19.65-to-23.92 GHz) (see Fig. 6.10 (a) and Fig. 6.9 (a)). Further, both measured and simulated average ISO between the two ports at the  $K$ -band are better than 80-dB for the machined DRA configuration, with a worst-case measured ISO of 72.9 dB at 23 GHz (see Fig. 6.10 (a)). For the 3D-printed  $K$ -band DRA, the measured ISO between the two ports achieves better than 80-dB over (21-to-24 GHz) and 50-dB over (24-to-26 GHz), with a worst-case measured ISO of 41.6 dB at 24.9 GHz (see Fig. 6.9 (a)). This reduced ISO is attributed to the measured frequency offset. At the  $K_a$ -band, the frequency deviation caused by the incomplete lamination affected the impedance matching of the  $K_a$ -band sub-array. By comparing the minima locations of both

the simulated and measured reflection coefficient, and the gain-bandwidth curves, we could define the bandwidth of the machined and 3D-printed DRA in the shared configuration as 2.4 GHz (30.7-to-33.4 GHz) and 2.3 GHz (31-to-33.3 GHz) corresponding to the -8-dB impedance BW of 4 GHz (29.3-to-33.3 GHz) and 3.88 GHz (29.32-to-33.2 GHz) for the simulated results of the machined and 3D-printed model, respectively (see Fig. 6.10 (b) and Fig. 6.9 (b)). Further, the measured average ISO between the two ports at the  $K_a$ -band is better than 49 dB over (30.7-to-33.4 GHz) and 42 dB over (31-to-32.8 GHz) for both machined and 3D-printed sub-arrays, respectively.

To conclude, the high isolation achieved is attributed to the implemented methodology for feeding the  $K$ -/  $K_a$ -band radiators. The filtering nature of SIW allowed the propagation of TE<sub>10</sub> mode at  $K_a$ -band while suppressing the propagation at  $K$ -band (i.e., before cutoff frequency). Further, the orthogonality of the modes of the selected feeding technologies (i.e., SIW supporting the TE<sub>10</sub> and SICL supporting the TEM) improved the isolation at the  $K_a$  band. Although, there is no coupling between the Tx and Rx DRAs as illustrated by the isolation measurement between the Tx and Rx DRAs. However, the Rx DRA is inevitably located in the near field region of the Tx sub-array due to its size. Therefore, the Rx DRA is perturbed by the near field of the Tx sub-array allowing an increase in bandwidth as compared to the standalone. Using higher ( $\epsilon_r$ ) for the Rx DRA will allow its implementation with minimum footprint. Thus, the performance of the Rx DRA in shared-aperture will identically resemble the standalone one in terms of operating BW.

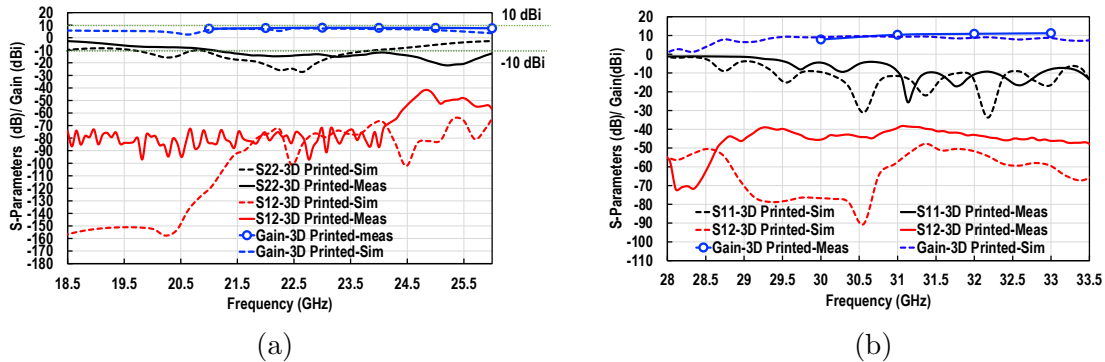


Figure 6.9: Measured vs simulated reflection coefficient and gain of the shared-aperture 3D-printed sub-array a)  $K$ -band b)  $K_a$ -band

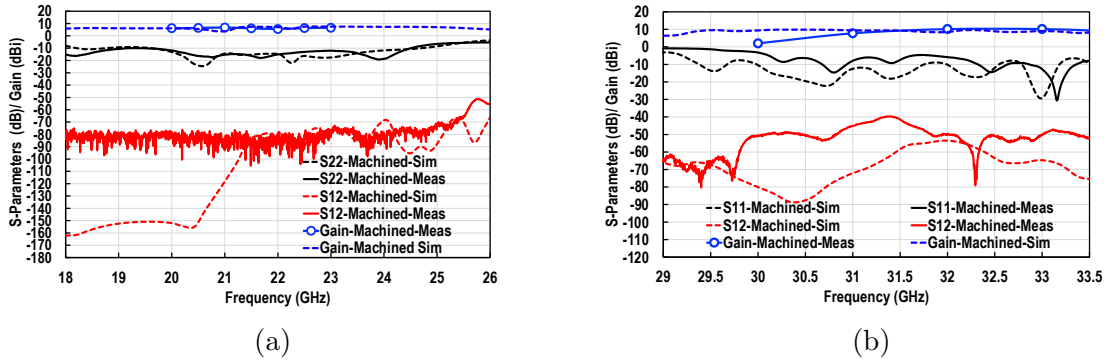


Figure 6.10: Measured vs simulated reflection coefficient and gain of the shared-aperture machined sub-array a)  $K$ -band b)  $K_a$ -band

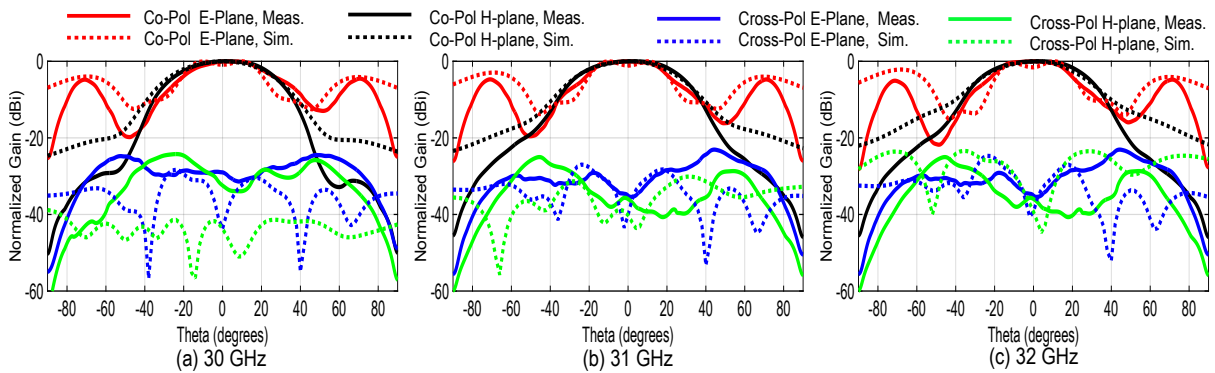


Figure 6.11: Measured vs simulated normalized radiation patterns of the 3D-printed  $K_a$ -band sub-array in shared-aperture configuration

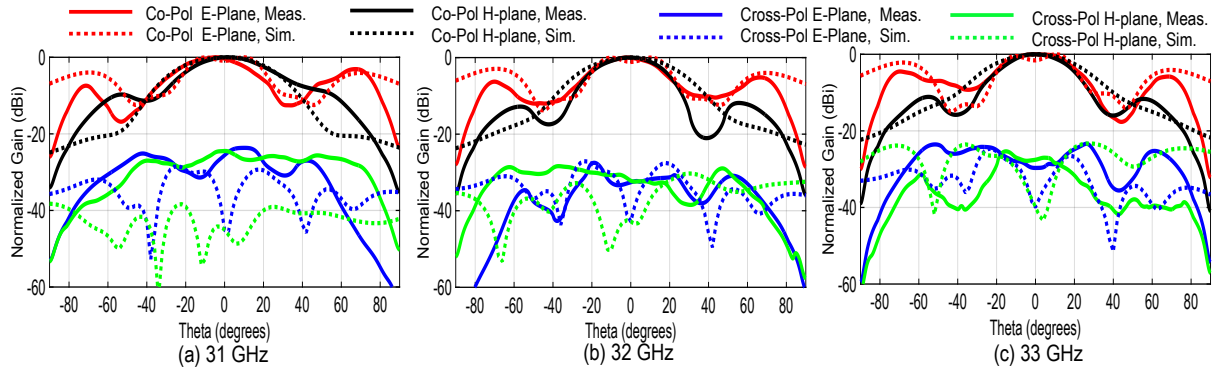


Figure 6.12: Measured vs simulated normalized radiation patterns of the machined  $K_\alpha$ -band sub-array in shared-aperture configuration

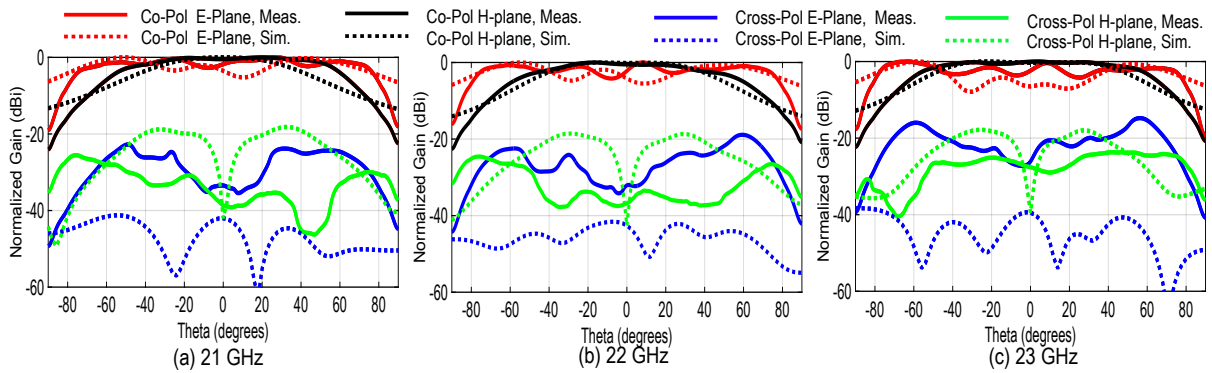


Figure 6.13: Measured vs simulated normalized radiation patterns of the 3D-printed  $K$ -band antenna in shared-aperture configuration

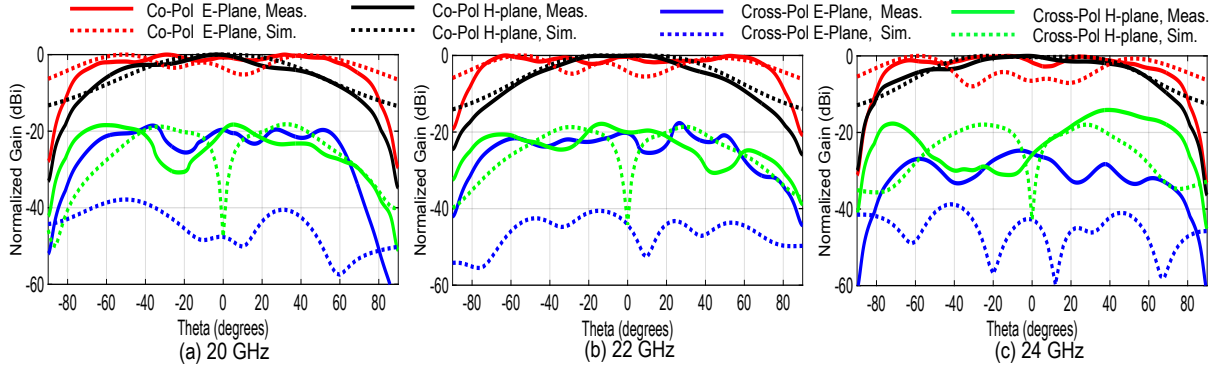


Figure 6.14: Measured vs simulated normalized radiation patterns of the machined  $K$ -band antenna in shared-aperture configuration

## 6.5.2 Radiation Patterns and Gain Measurements

When the  $K$ -/ $K_a$ - shared-array configuration is excited at  $K_a$ -band (i.e.,  $K$ -band is matched), the measured normalized radiation patterns in the E- and H-plane, are demonstrated in Fig. 6.11 and Fig. 6.12 for the 3D-printed and machined arrays, respectively. Measurements agree well with the simulations presented in Fig. 6.6. The arrays exhibit an excellent cross-polarization level of at least 30 dB. The machined sub-array pattern is slightly distorted at some frequencies. This is probably due to the bonding effect tolerance illustrated in Chapter 5. Fig. 6.13 and Fig. 6.14 represent the measured normalized radiation pattern in both E- and H-plane for the 3D-printed and machined DRAs when the  $K$ -/ $K_a$ - shared-array configuration is excited at  $K$ -band (i.e.,  $K_a$ -band is matched). The cross-polarization level is better than 26 dB and 17 dB for the 3D-printed and machined DRAs. Ripples in the E-plane of the  $K$ -band DRAs are attributed to both the scattering from the  $K_a$ -band DRAs and the diffraction from the finite ground plane effect.

Furthermore, the maximum directivity and realized gain of the shared-aperture in both frequency modes of operation ( $K_a$ -/  $K$ - bands) are measured using the standard gain antenna calibration method. The simulated and measured realized gains for the machined and 3D-printed shared-aperture array (excited at  $K_a$ -, excited at  $K$ -) are demonstrated over their operating bandwidth as shown in Fig. 6.10, and Fig. 6.9. For the  $K$ -band DRA in shared-aperture configuration, the simulated average realized gains are 6.6 dBi, and 6.3 dBi for the machined and 3D-printed DRA (see Fig. 6.10 (a) and Fig. 6.9 (a)), respectively. For the  $K_a$ -band shared-aperture sub-array, the simulated average realized gains are 9.2 dBi, and 8.9 dBi for the machined and 3D-printed DRAs, respectively. The

measured results present a good agreement taking into account the possible estimation error in the near field measurement of the gain [109]. Further, the maximum directivities along with the maximum realized gains are measured for both the  $K$ -band and  $K_a$ -band radiators. A summary of the average simulated and measured gains, directivities and radiation efficiencies are listed in the table 6.3. An almost good agreement between the measured and simulated gains and directivities is achieved. A 0.5 to 1 dB increase in some measurements is noticed as compared to the simulations ones. This is caused by the calibration tolerance of the planar NF system for low-gain antenna measurements. Moreover, the 3D-printed DRAs are mainly presenting higher directivity as compared to the machined ones. This phenomenon could be present by the non-uniform nature of the 3D-printed DRAs, which is not addressed in this work. The low efficiency of the  $K_a$ -band sub-array is caused by the feed circuit losses ( conductor and dielectric losses).

Table 6.3: Average Simulated vs Measured Shared-aperture Antenna Parameters

	Gain (dBi)	Directivity (dBi)	Efficiency (%)
Machined $K$ -band DRA (Sim.)	6.6	7.3	84
Machined $K$ -band DRA (Meas.)	6.3	7.7	73
Machined $K_a$ -band DRAs sub-array (Sim.)	9.2	11.6	57
Machined $K_a$ -band DRAs sub-array (Meas.)	9.3	12.7	46
3D-printed $K$ -band DRA (Sim.)	6.3	7.1	82.7
3D-printed $K$ -band DRA (Meas.)	7.7	8	93
3D-printed $K_a$ -band DRAs sub-array (Sim.)	8.9	11.64	56.6
3D-printed $K_a$ -band DRAs sub-array (Meas.)	10	13	52.4

## 6.6 Comparison with Recent Literature

Table 6.4 lists a comparison between different shared-aperture arrays operating at mm-wave ranges with small frequency ratios (1.5 to 2), particularly at the  $K$ -/ $K_a$ -band. The metallic structures presented in [156, 168] are bulky and not easily integrated with PCBs, which is necessary for the use of several applications. Recently, a similar topology for integration is published in [88]. However, the series-fed combination is unsuitable for modular designs and wideband applications, significantly when antenna aperture increases. Compared with the other mm-wave shared-aperture techniques, the presented work exhibits superior isolation, excellent broadband operation, and low cross-polarization, mainly attributed to the use of

Table 6.4: Performance Comparison with Recent Literature

Ref.	BW (GHz) at $K^-$	BW (GHz) at $K_a^-$	ISO (dB)	X- level(dB)	Profile	No. of layers	Comment
[48] <sup>1,3</sup>	-	-	<-50	-	-	-	narrow BW (few MHz) <sup>6</sup>
[44] <sup>1,3</sup>	1.7	1.68	-	-20	> 1.5 mm	$\geq 3$	narrow BW complex feeding structure
[156] <sup>1,3</sup>	1.7	1.9	<-80, <-50	-40	> 5.5 mm	3	bulky, heavy not integrable
[168] <sup>1,3</sup>	2	2	-	-40	> 4 mm	2	bulky, heavy not integrable
[88] <sup>1,3</sup>	2.8	6	<-60, <-50	-25	1.73 mm	4	series-fed, Not suitable for modular applications
[40] <sup>2,3</sup>	3	1.5	<-70, <-30	-25	40 mm	-	3Dimensional, bulky not integrable, complex
This work:Mach. <sup>1,3</sup>	5	2.4	<-80, <-49	-20, -32 <sup>4</sup>	0.508 mm <sup>5</sup>	3	low profile Good bandwidth, isolation
This work:3D-Print <sup>1,3</sup>	5.5	2.3	<-80, <-42	-30, -34 <sup>4</sup>	0.508 mm <sup>5</sup>	3	low profile Good bandwidth, isolation

<sup>1</sup> The operating bands are  $K^-$ ,  $K_a^-$ , <sup>2</sup> The operating bands are  $K_u^-$ ,  $K_a^-$ , <sup>3</sup> Polarization is linear for both bands, <sup>4</sup> Computed at mid frequency, <sup>5</sup> Stack-up height without DRAs, <sup>6</sup> Estimated from plots

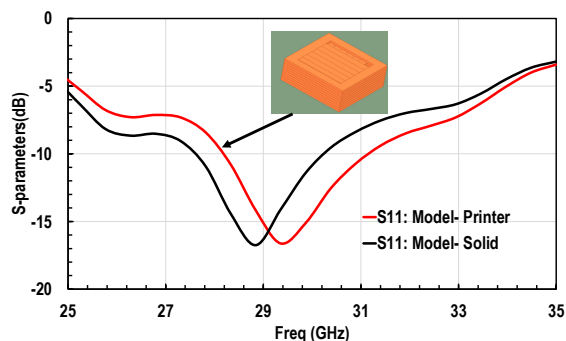


Figure 6.15: Simulated S-parameters for solid model vs 3D-Printed model

two feeding structures that support two modes. Further, the design provides a low-cost solution using PCB and 3D-printing technology. Besides, our approach provides a low profile, lightweight, and design flexibility in implementation. This configuration can be easily modified to achieve a modular design to support large order phased arrays.

## 6.7 Comment on Characterization

The material characterization is performed based on the OCP method. This method is tolerant to tiny air gaps as stated in [165, 169, 170]. This tolerance is noticeable when a high  $\epsilon_r$  material is used [165]. Further, the calibration process predicts the expected value of the air gap caused by the surface roughness of the probe only [165]. Due to the nature of the 3D-printed samples, the top side of the model has a higher degree of surface roughness beyond the recommended maximum value of  $0.4 \mu\text{m}$  stated in [165]. Thus, the non-flat surface could have caused a deviation in the measurement of the  $\epsilon_r$  of the sample [170]. Further, the accuracy of 3D-printing small objects is subject to the material's mechanical properties and the 3D-printer capabilities. Thus, some gaps in printing can occur between the infill and the 3D-printed wall around the perimeter of the model. A model for the 3D-printed DRA is designed and simulated using HFSS to diagnose the effect of those gaps. As shown in Fig. 6.15, a 5.4% decrease in the filling of the DRA can introduce a 0.6-GHz frequency shift. This justifies the deviation between the 3D-printed and machined DRA. This offset can be corrected using a filament with higher  $\epsilon_r$ . Accordingly, it can provide more margin in varying the effective  $\epsilon_r$  by changing the infill percentage.

## 6.8 Conclusion

A shared-aperture array of 3D-printed Dielectric Resonator Antennas (DRAs) has been proposed in the  $K$ -, and  $K_a$ -band for full-duplex SatCom applications. With the combination of two feeding technologies and orthogonal polarization for the DRAs, state-of-the-art isolation between the antennas of more than 80-dB and 50-dB at  $K$ - and  $K_a$ -bands is achieved, respectively. With the attached 3D-printed sheet for the DRAs, the antennas are fabricated and aligned accurately to the PCBs. The presented shared-aperture array provides a modular, low-cost solution for mm-wave applications.

# Chapter 7

## Contributions and Future Work

This chapter summarizes the contributions of the Ph.D. thesis project to standalone antenna designs as well as the shared-aperture array design. Furthermore, recommendations for future research in these areas are proposed.

### 7.1 Contribution

Implementing phased array systems using separate platforms for each frequency band is costly and consumes a large footprint. System miniaturization using ultrawideband arrays and multiband radiators suffers from high profile and complex integration. On the other hand, shared-aperture arrays are developed implementation for multifunctional arrays, in which multiple radiators share the same aperture. However, it has been deduced that not all implemented architectures are suitable for mm-wave applications. In addition, the state-of-art shared-aperture arrays utilize 3-Dimensional bulky structures to achieve the required specifications. Therefore, they are also not ideal for modular, scalable phased arrays. Moreover, few designs targeted  $K$ -/ $K_a$ -bands shared-aperture array with acceptable isolation and sufficient bandwidth.

Therefore, this dissertation has focused on analyzing, designing, and validating a shared-aperture array suitable for scalable modular phased-antenna-array for SatCom applications. The main building components designed to fulfill the work include: 1) a substrate-integrated coaxial line fed  $K$ -band DRA, 2) a substrate-integrated waveguide fed  $K_a$ -band DRA, 3) a shared-aperture array comprised of one cell of  $2 \times 2$   $K_a$ -band DRA, and one  $K$ -band DRA. All antenna prototypes are implemented using PCB technology, three-metallic

layer stack-up, and minimal blind vias. DRAs are fabricated using 3D-printing technology, which is promising in leveraging the DRA's usage in mm-wave bands. Further, to the author's best knowledge, no shared aperture arrays have been reported with DRAs in the reported literature.

Chapter 3 presents the analysis of the proposed shared-aperture DRA array. The effect of integrating DRAs operating at  $K$ -/  $K_a$ -bands in shared configuration is investigated, based on specified evaluating parameters. Both square and cylindrical-shaped DRAs are used in this analysis, in which the design procedure is highlighted. Further, a preliminary analysis based on the orientation and position of the DRAs in the lattice structure is presented. DRAs are considered excellent radiator choices for shared-aperture arrays based on the simulated results.

In chapter 4, a novel substrate integrated coaxial line (SICL) fed- DRA was proposed. The proposed antenna is aperture-coupled using an H-shaped slot on the top conductor layer, generating a linearly-polarized radiation pattern. A wideband SICL line was utilized to excite the aperture slot, minimizing the corresponding feeding circuit, with a shielded TEM mode line. Therefore, the proposed antenna constitutes a minimum footprint. While integration in shared-aperture configuration reduces spurious radiation and coupling within the substrate. The proposed antenna realizes excellent impedance bandwidth of more than 2 GHz while maintaining excellent cross-polarization of more than 30 dB over the whole bandwidth. Further, the proposed antenna's design parameters experience almost no sensitivity for the PCB fabrication tolerances. The 3D-printed DRA is further compared to machined DRA, designed using standard commercial laminates. The 3D-printed DRA is shifted in the frequency domain, mainly due to the characterization of the 3D-printed material. The feeding line occupies an area of 1.5 mm, which is considered a good achievement compared to the size of feeding circuits for radiators at the same band. Further, to the author's best knowledge, no SICL-fed DRA- is published in the reported literature.

In chapter 5, a substrate integrated waveguide (SIW)- fed DRA was designed. The SIW is not implemented using the traditional one-layered substrate. However, two substrate layers are incorporated in the design, minimizing blind vias when integrating the design in a shared-aperture configuration. The proposed antenna is aperture-coupled using a rectangular-shaped slot on the top conductor, generating a linearly-polarized radiation pattern. The shielded SIW line was utilized to excite the aperture slot, allowing the propagation of  $TE_{10}$  mode. The proposed antenna showed excellent impedance bandwidth of more than 2 GHz and excellent cross-polarization of more than 30 dB. Further, the proposed antenna's parameters experienced low sensitivity for the PCB tolerances. The measured DRA response is shifted in the frequency domain due to fabrication tolerance in the bonding material.

Finally, Chapter 6 presented the proposed  $K$ -/ $K_a$ -bands shared-aperture array, which features high isolation using 3D-printed dielectric resonator antennas (DRAs). Combining two feeding technologies and orthogonal polarization for the DRAs, state-of-the-art isolation between the antennas of more than 80-dB and 50-dB at  $K$ - and  $K_a$ -bands is achieved, respectively. With the attached 3D-printed sheet for the DRAs, the antennas are fabricated and aligned accurately to the PCBs. The presented shared-aperture array provides a modular, low-cost solution for mm-wave applications.

## 7.2 Future Work

Section 7.1, summarized the contributions of the Ph.D. work, the vision in this thesis is to develop a sub-array, capable of further expansion to a modular, scalable phased array for mm-wave applications. Based on the designed and fabricated measurement results, several potential development areas are identified as opportunities for enhancing the proposed concepts and are summarized in this section.

Firstly, the SICL-fed DRA standalone antenna introduced in this research presented a good performance while achieving a small footprint. The goal of this stage of the work was restricted in the design of the DRA by the available laminate thickness. After verifying the potential of using 3D-printed DRAs, DRA design could be optimized to achieve any required performance, such as minimized footprint. Moreover, the different reported versions for SICL could be explored to provide more flexibility in routing more extensive feeding networks.

The SIW-fed DRA antenna, implemented in two substrate layers, presented excellent performance. Though, the proposed implementation introduced in this research showed a good impedance reflection coefficient bandwidth and reduced manufacturing complexity. However, the sensitivity to the bonding material should be further corrected by changing the fabrication process.

Thirdly, the research goal of this Ph.D. is to explore the shared-aperture using two different feeding mechanisms, SIW and TEM, with the most straightforward technological implementation. It is worth exploring the effect of miniaturized SIWs to reduce the feeding network's footprint further. Further, larger-scale modular scalar shared aperture DRA is considered an extension of this work.

Fourthly, the characterization of 3D-printed materials was performed using commercial characterization devices. Based on the reported results, we believe that developing a char-

acterization device for miniaturized 3D-printed structures is another important research direction for accurately predetermining the electrical properties of the 3D-printed DRAs.

## 7.3 List of Publications

This section lists the academic publications based on the Ph.D. contributions stated in Section 7.1.

Submitted/ Accepted publications:

1. Heba El-Sawaf, Wael M. Abdel-Wahab, and Safieddin Safavi Naeini, "A  $K$ -/ $K_a$ -Shared-Aperture DRA Array with High Isolation," *2019 IEEE International Symposium on Antennas and Propagation and USNC-URSI Radio Science Meeting*, (Published)
2. Heba El-Sawaf, Wael M. Abdel-Wahab, Naimeh Ghafarian, Ardeshir Palizban, Ahmad Ehsandar, and Safieddin Safavi Naeini, "A 3D-Printed DRA Shared-Aperture Array for Low-Cost Millimeter-Wave Applications," *2022 IEEE Transactions on Antennas and Propagations*, (Submitted, Under review Jan 5, 2022).
3. Heba El-Sawaf, Wael M. Abdel-Wahab, and Safieddin Safavi Naeini, "Mm-wave 3D-printed DRAs for Cost-effective Emerging 5G- and SatCom Applications," *2022 IEEE International Symposium on Antennas and Propagation and USNC-URSI Radio Science Meeting*, (Submitted)

Other contributed publications:

1. Abdel-Wahab, W.M.; Al-Saedi, H.; Raeiszadeh, M.; Alian, E.; Chen, G.; Ehsandar, A.; Ghafarian, N.; El-Sawaf, H.; Palizban, A.; Nezhad-Ahmadi, M.R.; Safavi-Naeini, S, "A Modular Architecture for Low Cost Phased Array Antenna System for Ka-Band Mobile Satellite Communication," *IET Conference Proceedings*, 2018, p. 19 (5 pp.)-19 (5 pp.).
2. W. M. A. Wahab, H. El-Sawaf, H. Al-Saedi, S. Gigoyan and S. Safavi-Naeini, "Broadband CP SIW-Integrated DRA Array with Wideband Axial-Ratio for Millimeter-Wave System Applications," *2018 18th International Symposium on Antenna Technology and Applied Electromagnetics (ANTEM)*, 2018, pp. 1-3.
3. W. M. Abdel-Wahab et al., "Affordable Large Scale Active-Phased Array Antenna for Ka-Band Mobile SATCOM Applications," *2019 13th European Conference on Antennas and Propagation (EuCAP)*, 2019, pp. 1-4.
4. H. El-Sawaf, W. M. Abdel-Wahab, H. Al-Saedi and S. Safavi-Naeini, "SIW Center-Fed Series Rectangular DRA Arrays," *2020 IEEE International Symposium on*

*Antennas and Propagation and North American Radio Science Meeting*, 2020, pp. 217-218.

5. H. El-Sawaf, W. M. Abdel-Wahab, S. Safavi-Naeini and H. Al-Saedi, "CP Gain Enhancement of MM-Wave SIW-Integrated DRA Array Antenna," *2021 IEEE International Symposium on Antennas and Propagation and USNC-URSI Radio Science Meeting (APS/URSI)*, 2021, pp. 1159-1160.

Publications in preparation :

1. letter paper on the SICL-fed DRA
2. Conference/letter paper on the shared-feeding network.

# References

- [1] V. Joroughi, L. K. Alminde, and E. Cruz, “5g satellite communications services through constellation of leo satellites,” in *Ad-Hoc, Mobile, and Wireless Networks*, M. R. Palattella, S. Scanzio, and S. Coleri Ergen, Eds. Cham: Springer International Publishing, 2019, pp. 543–548.
- [2] A. Abbaspour-Tamijani and K. Sarabandi, “An Affordable Millimeter-Wave Beam-Steerable Antenna Using Interleaved Planar Subarrays,” *IEEE Transactions on Antennas and Propagation*, vol. 51, no. 9, pp. 2193–2202, 2003.
- [3] G. Gao, Y. Zhang, A. Li, J. Zhao, and H. Cheng, “Shared-aperture ku/ka bands microstrip array feeds for parabolic cylindrical reflector.” *IEEE*, 5 2010, pp. 1028–1030.
- [4] C.-X. Mao, S. Gao, Q. Luo, T. Rommel, and Q.-X. Chu, “Low-cost x/ku/ka-band dual-polarized array with shared aperture,” *IEEE Transactions on Antennas and Propagation*, vol. 65, pp. 3520–3527, 7 2017.
- [5] D. Fei, J. Wang, T. Zhang, G. Liang, and L. He, “A shared-aperture dual circularly polarized antenna array for satellite communication.” *IEEE*, 10 2016, pp. 1–4.
- [6] J. F. Zhang, Y. J. Cheng, Y. R. Ding, and C. X. Bai, “A dual-band shared-aperture antenna with large frequency ratio, high aperture reuse efficiency, and high channel isolation,” *IEEE Transactions on Antennas and Propagation*, vol. 67, no. 2, pp. 853–860, 2019.
- [7] S. Rangan, T. S. Rappaport, and E. Erkip, “Millimeter-wave cellular wireless networks: Potentials and challenges,” *Proceedings of the Ieee*, vol. 102, pp. 366–385, 2014.
- [8] “[https://www.iea.org/reports/data-centres-and-data-transmission-networks.](https://www.iea.org/reports/data-centres-and-data-transmission-networks)”

- [9] “<https://www.eetasia.com/millimeter-wave-technology-the-turbo-of-the-information-age/>.”
- [10] L. Boero, R. Bruschi, F. Davoli, M. Marchese, and F. Patrone, “Satellite networking integration in the 5g ecosystem: Research trends and open challenges,” *IEEE Network*, vol. 32, no. 5, pp. 9–15, 2018.
- [11] K. Liolis, A. Geurtz, R. Sperber, D. Schulz, S. Watts, G. Poziopoulou, B. Evans, N. Wang, O. Vidal, B. Tiomela Jou, M. Fitch, S. Diaz Sendra, P. Sayyad Khodashenas, and N. Chuberre, “Use cases and scenarios of 5g integrated satellite-terrestrial networks for enhanced mobile broadband: The sat5g approach,” *International Journal of Satellite Communications and Networking*, vol. 37, no. 2, pp. 91–112, 2019.
- [12] B. R. Elbert, *The Satellite Communication Applications Handbook*, ser. Artech House space technology and applications library. Artech House, 2004.
- [13] O. Kodheli, E. Lagunas, N. Maturo, S. K. Sharma, B. Shankar, J. F. M. Montoya, J. C. M. Duncan, D. Spano, S. Chatzinotas, S. Kisseleff, J. Querol, L. Lei, T. X. Vu, and G. Goussetis, “Satellite communications in the new space era: A survey and future challenges,” *IEEE Communications Surveys Tutorials*, vol. 23, no. 1, pp. 70–109, 2021.
- [14] M. Giordani and M. Zorzi, “Satellite communication at millimeter waves: a key enabler of the 6g era,” in *2020 International Conference on Computing, Networking and Communications (ICNC)*, 2020, pp. 383–388.
- [15] F. Tabarani, L. Boccia, T. Purtova, A. Shamsafar, H. Schumacher, and G. Amendola, “0.25- $\mu$  bimos system-on-chip for k-/ka-band satellite communication transmit–receive active phased arrays,” *IEEE Transactions on Microwave Theory and Techniques*, vol. 66, pp. 2325–2339, 5 2018.
- [16] C. Wang, E. Li, and D. F. Sievenpiper, “Surface-wave coupling and antenna properties in two dimensions,” *IEEE Transactions on Antennas and Propagation*, vol. 65, pp. 5052–5060, 2017.
- [17] Leong See Chuan, Sun Ru-Tian, and Yip Peng Hon, “Ka band satellite communications design analysis and optimisation,” *DSTA Horizons*, pp. 70–78, 2015.

- [18] J. Helander, K. Zhao, Z. Ying, and D. Sjöberg, “Performance analysis of millimeter-wave phased array antennas in cellular handsets,” *IEEE Antennas and Wireless Propagation Letters*, vol. 15, pp. 504–507, 2016.
- [19] R. McMorrow, D. Corman, and A. Crofts, “All silicon mmw planar active antennas: The convergence of technology, applications, and architecture.” *IEEE*, 11 2017, pp. 1–4.
- [20] S. Keyrouz and D. Caratelli, “Dielectric resonator antennas: Basic concepts, design guidelines, and recent developments at millimeter-wave frequencies,” 2016.
- [21] A. Belenguer, A. L. Borja, H. Esteban, and V. E. Boria, “High-performance coplanar waveguide to empty substrate integrated coaxial line transition,” *IEEE Transactions on Microwave Theory and Techniques*, vol. 63, pp. 4027–4034, 2015.
- [22] D. Deslandes and K. Wu, “Integrated microstrip and rectangular waveguide in planar form,” *IEEE Microwave and Wireless Components Letters*, vol. 11, no. 2, pp. 68–70, 2001.
- [23] F. Gatti, M. Bozzi, L. Perreggini, K. Wu, and R. G. Bosisio, “A novel substrate integrated coaxial line (sicl) for wide-band applications,” 2006, pp. 1614–1617, iD: 1.
- [24] J. S. Silva, M. Garcia-Vigueras, T. Debogovic, J. R. Costa, C. A. Fernandes, and J. R. Mosig, “Stereolithography-based antennas for satellite communications in ka-band,” 2017.
- [25] I. Gibson, D. W. Rosen, and B. Stucker, *Additive manufacturing technologies: Rapid prototyping to direct digital manufacturing*, 2010.
- [26] T. A. Axness, R. V. Coffman, B. A. Kopp, and K. W. O’Haver, “Shared aperture technology development,” *Johns Hopkins APL Technical Digest (Applied Physics Laboratory)*, vol. 17, pp. 285–293, 1996.
- [27] K. Naishadham, R. Li, L. Yang, T. Wu, W. Hunsicker, and M. Tentzeris, “A shared-aperture dual-band planar array with self-similar printed folded dipoles,” *IEEE Transactions on Antennas and Propagation*, vol. 61, pp. 606–613, 2013.
- [28] J. K. Hsiao, “Analysis of interleaved arrays of waveguide elements,” *IEEE Transactions on Antennas and Propagation*, vol. 19, pp. 729–735, 1971.

- [29] Kuan Lee, J. Clark, Ruey Chu, Nam Wong, and R. Tang, "A dual band phased array using interleaved waveguides and dipoles printed on high dielectric substrate," in *1984 Antennas and Propagation Society International Symposium*, vol. 22. Institute of Electrical and Electronics Engineers, pp. 886–889.
- [30] Ruey-Shi Chu, Kuan Min Lee, and A. Wang, "Multiband phased-array antenna with interleaved tapered-elements and waveguide radiators," in *IEEE Antennas and Propagation Society International Symposium. 1996 Digest*, vol. 3. IEEE, pp. 1616–1619.
- [31] R. Pokuls, J. Uher, and D. M. Pozar, "Dual-frequency and dual-polarization microstrip antennas for sar applications," *IEEE Transactions on Antennas and Propagation*, vol. 46, pp. 1289–1296, 1998.
- [32] H. Schippers, J. Verpoorte, P. Jorna, A. Hulzinga, A. Thain, G. Peres, and H. van Gemeren, "Development of dual-frequency airborne satcom antenna with optical beamforming." IEEE, 3 2009, pp. 1–16.
- [33] X. Qu, S. S. Zhong, Y. M. Zhang, and W. Wang, "Design of an s/x dual-band dual-polarised microstrip antenna array for sar applications," *IET Microwaves, Antennas and Propagation*, vol. 1, p. 513, 2007.
- [34] Y. Cui, R. Li, and P. Wang, "Novel dual-broadband planar antenna and its array for 2g/3g/lte base stations," *IEEE Transactions on Antennas and Propagation*, vol. 61, pp. 1132–1139, 3 2013.
- [35] Shanhong He and Jidong Xie, "Analysis and Design of a Novel Dual-Band Array Antenna With a Low Profile for 2400/5800-MHz WLAN Systems," *IEEE Transactions on Antennas and Propagation*, vol. 58, no. 2, pp. 391–396, feb 2010.
- [36] L. Shafai, W. Chamma, G. Seguin, and N. Sultan, "Dual-band dual-polarized microstrip antennas for sar applications." IEEE, pp. 1866–1869.
- [37] A. Vallecchi, G. Gentili, and M. Calamia, "Dual-band dual polarization microstrip antenna," in *IEEE Antennas and Propagation Society International Symposium. Digest. Held in conjunction with: USNC/CNC/URSI North American Radio Sci. Meeting (Cat. No.03CH37450)*, vol. 4. IEEE, pp. 134–137.
- [38] D. Pozar and S. Targonski, "A shared-aperture dual-band dual-polarized microstrip array," *IEEE Transactions on Antennas and Propagation*, vol. 49, pp. 150–157, 2001.

- [39] L. Shafai, “Bandwidth and polarization characteristics of perforated patch antennas.” IEE, 1997, pp. v1–43–v1–43.
- [40] Y. R. Ding and Y. J. Cheng, “Ku/ka dual-band dual-polarized shared-aperture beam-scanning antenna array with high isolation,” *IEEE Transactions on Antennas and Propagation*, vol. 67, pp. 2413–2422, 4 2019.
- [41] C.-X. Mao, S. Gao, Y. Wang, Q. Luo, and Q.-X. Chu, “A shared-aperture dual-band dual-polarized filtering-antenna-array with improved frequency response,” *IEEE Transactions on Antennas and Propagation*, vol. 65, pp. 1836–1844, 4 2017.
- [42] K. Woelders and J. Granholm, “Cross-polarization and sidelobe suppression in dual linear polarization antenna arrays,” *IEEE Transactions on Antennas and Propagation*, vol. 45, pp. 1727–1740, 1997.
- [43] N. A. Aboserwal, J. L. Salazar, and C. Fulton, “Current polarization impact on cross-polarization definitions for practical antenna elements,” 2017.
- [44] A. I. Sandhu, E. Arnieri, G. Amendola, L. Boccia, E. Meniconi, and V. Ziegler, “Radiating elements for shared aperture tx/rx phased arrays at k/ka band,” *IEEE Transactions on Antennas and Propagation*, vol. 64, pp. 2270–2282, 6 2016.
- [45] J.-D. Zhang, W. Wu, and D.-G. Fang, “Dual-band and dual-circularly polarized shared-aperture array antennas with single-layer substrate,” *IEEE Transactions on Antennas and Propagation*, vol. 64, pp. 109–116, 1 2016.
- [46] C.-X. Mao, S. Gao, C. Tienda, T. Rommel, A. Patyuchenko, M. Younis, L. Boccia, E. Arnieri, S. Glisic, U. Yodprasit, P. Penkala, M. Krstic, F. Qin, O. Schrape, A. Koczor, G. Amendola, and V. Petrovic, “X/Ka-Band Dual-Polarized Digital Beamforming Synthetic Aperture Radar,” *IEEE Transactions on Microwave Theory and Techniques*, vol. 65, no. 11, pp. 4400–4407, nov 2017.
- [47] C.-X. Mao, S. Gao, Y. Wang, Q.-X. Chu, and X.-X. Yang, “Dual-band circularly polarized shared-aperture array for  $c$  -/  $x$  -band satellite communications,” *IEEE Transactions on Antennas and Propagation*, vol. 65, no. 10, pp. 5171–5178, 2017.
- [48] A. Zamanifekri, C. Lu, H. J. Visser, P. Sanders, M. K. Matters-Kammerer, M. Geurts, P. G. M. Baltus, and A. B. Smolders, “An active ka-band shared-aperture antenna with 50 db isolation for satellite communication,” *IEEE Antennas and Wireless Propagation Letters*, vol. 16, pp. 2042–2045, 2017.

- [49] M. Shirazi, J. Huang, T. Li, and X. Gong, “A switchable-frequency slot-ring antenna element for designing a reconfigurable array,” 2017.
- [50] J. D. Zhang, L. Zhu, N. W. Liu, and W. Wu, “Dual-band and dual-circularly polarized single-layer microstrip array based on multiresonant modes,” *IEEE Transactions on Antennas and Propagation*, vol. 65, no. 3, pp. 1428–1433, 2017.
- [51] C.-L. Cho, H.-L. Kao, L.-C. Chang, Y.-H. Wu, and H.-C. Chiu, “Inkjet-printed multilayer bandpass filter using liquid crystal polymer system-on-package technology,” *IEEE Transactions on Components, Packaging and Manufacturing Technology*, vol. 6, 2016.
- [52] R. K. Mongia and A. Ittipiboon, “Theoretical and experimental investigations on rectangular dielectric resonator antennas,” *IEEE Transactions on Antennas and Propagation*, vol. 45, pp. 1348–1356, 1997.
- [53] W. Wahab, “Low cost planar waveguide technology-based dielectric resonator antenna (dra) for millimeter-wave applications: Analysis, design, and fabrication,” *IEEE Transactions on Antennas and Propagation*, vol. 58, pp. 2499–2507, 2010.
- [54] Q. Lai, G. Almpanis, C. Fumeaux, H. Benedickter, and R. Vahldieck, “Comparison of the radiation efficiency for the dielectric resonator antenna and the microstrip antenna at ka band,” *IEEE Transactions on Antennas and Propagation*, vol. 56, pp. 3589–3592, 2008.
- [55] M. R. Nezhad-Ahmadi, M. Fakharzadeh, B. Biglarbegian, and S. Safavi-Naeini, “High-efficiency on-chip dielectric resonator antenna for mm-wave transceivers,” *IEEE Transactions on Antennas and Propagation*, vol. 58, no. 10, pp. 3388–3392, 2010.
- [56] A. Perron, T. A. Denidni, and A.-R. Sebak, “High-gain hybrid dielectric resonator antenna for millimeter-wave applications: Design and implementation,” *IEEE Transactions on Antennas and Propagation*, vol. 57, pp. 2882–2892, 2009.
- [57] Q. Lai, C. Fumeaux, W. Hong, and R. Vahldieck, “60 ghz aperture-coupled dielectric resonator antennas fed by a half-mode substrate integrated waveguide,” *IEEE Transactions on Antennas and Propagation*, vol. 58, pp. 1856–1864, 2010.
- [58] J. A. Byford, M. I. M. Ghazali, S. Karuppuswami, B. L. Wright, and P. Chahal, “Demonstration of rf and microwave passive circuits through 3-d printing and selective metalization,” *IEEE Transactions on Components, Packaging and Manufacturing Technology*, vol. 7, pp. 463–471, 2017.

- [59] S. A. Long, M. W. McAllister, and L. C. Shen, "The resonant cylindrical dielectric cavity antenna," *IEEE Transactions on Antennas and Propagation*, vol. 31, pp. 406–412, 1983.
- [60] A. Petosa and A. Ittipiboon, "Dielectric resonator antennas: A historical review and the current state of the art," *IEEE Antennas Propag. Mag.*, vol. 52, pp. 91–116, 2010.
- [61] A. Petosa, *Dielectric Resonator Antenna Handbook*, ser. Artech House antennas and propagation library. Artech House, 2007.
- [62] S. K. K. Dash, T. Khan, and A. De, "Dielectric resonator antennas: An application oriented survey," 2017.
- [63] K. M. Luk and K. W. Leung, *Dielectric Resonator Antennas*, ser. Antennas S. Research Studies Press, 2003.
- [64] K. W. Leung, K. M. Luk, K. Y. A. Lai, and D. Lin, "Theory and experiment of an aperture-coupled hemispherical dielectric resonator antenna," *IEEE Transactions on Antennas and Propagation*, vol. 43, pp. 1192–1198, 1995.
- [65] L. Z. Thamae and Z. Wu, "Broadband bowtie dielectric resonator antenna," *IEEE Transactions on Antennas and Propagation*, vol. 58, pp. 3707–3710, 2010.
- [66] Y. M. Pan and S. Y. Zheng, "A low-profile stacked dielectric resonator antenna with high-gain and wide bandwidth," *IEEE Antennas and Wireless Propagation Letters*, vol. 15, pp. 68–71, 2016.
- [67] R. Chair, A. A. Kishk, K. F. Lee, and C. E. Smith, "Wideband flipped staired pyramid dielectric resonator antennas," *Electronics Letters*, vol. 40, pp. 608–610, 2004.
- [68] J. T. H. St. Martin, Y. M. M. Antar, A. A. Kishk, A. Ittipiboon, and M. Cuhaci, "Dielectric resonator antenna using aperture coupling," *Electronics Letters*, vol. 26, no. 24, pp. 5–6, 1990.
- [69] Z. C. Hao, W. Hong, A. Chen, J. Chen, and K. Wu, "Siw fed dielectric resonator antennas (siw-dra)," 2006, pp. 202–205.
- [70] W. M. Abdel-Wahab, D. Busuioc, and S. Safavi-Naeini, "Millimeter-wave high radiation efficiency planar waveguide series-fed dielectric resonator antenna (DRA)

- array: Analysis, design, and measurements,” *IEEE Transactions on Antennas and Propagation*, vol. 59, no. 8, pp. 2834–2843, 2011.
- [71] “<https://www.ansys.com/products/electronics/ansys-hfss>.”
- [72] R. K. Mongia and P. Bhartia, “Dielectric resonator antennas - a review and general design relations for resonant frequency and bandwidth,” *International journal of microwave and millimeter-wave computer-aided engineering*, vol. 4, pp. 230–247, 1994.
- [73] B. Liu, K. Xing, L. Wu, Z. Guo, X. Wei, Y. Ma, and R. Zhao, “A novel slot array antenna with a substrate-integrated coaxial line technique,” *IEEE Antennas and Wireless Propagation Letters*, vol. 16, pp. 1743–1746, 2017.
- [74] B. Liu, R. Zhao, Y. Ma, Z. Guo, X. Wei, W. Xing, and Y. Wang, “A 45° linearly polarized slot array antenna with substrate integrated coaxial line technique,” *IEEE antennas and wireless propagation letters*, vol. 17, pp. 339–342, 2018.
- [75] J. Yin, Q. Wu, C. Yu, H. Wang, and W. Hong, “Broadband endfire magnetoelectric dipole antenna array using sicl feeding network for 5g millimeter-wave applications,” *IEEE transactions on antennas and propagation*, vol. 67, pp. 4895–4900, 2019.
- [76] P. Chu, W. Hong, L. Dai, H. Tang, Z. Hao, J. Chen, and K. Wu, “Wide Stop-band Bandpass Filter Implemented With Spur Stepped Impedance Resonator and Substrate Integrated Coaxial Line Technology,” *IEEE Microwave and Wireless Components Letters*, vol. 24, no. 4, pp. 218–220, 2014.
- [77] T. Zhang, Y. Zhang, W. Hong, and K. Wu, “Wideband millimeter-wave siw cavity backed patch antenna fed by substrate integrated coaxial line.” *IEEE*, 2015, pp. 1–4.
- [78] Y. Shao, X.-C. Li, L.-S. Wu, and J.-F. Mao, “A Wideband Millimeter-Wave Substrate Integrated Coaxial Line Array for High-Speed Data Transmission,” *IEEE Transactions on Microwave Theory and Techniques*, vol. 65, no. 8, pp. 2789–2800, 2017.
- [79] K. Dong, X. Li, K. Ning, Y. Shao, and J. Mao, “Design of substrate integrated coaxial line under silicon-based mems process,” in *2019 IEEE MTT-S International Wireless Symposium (IWS)*, 2019, pp. 1–3.
- [80] K. Xing, B. Liu, Z. Guo, X. Wei, R. Zhao, and Y. Ma, “Backlobe and sidelobe suppression of a q-band patch antenna array by using substrate integrated coaxial

- line feeding technique,” *IEEE antennas and wireless propagation letters*, vol. 16, pp. 3043–3046, 2017.
- [81] B. Liu, Y. Ma, R. R. Zhao, W. Q. Xing, and Z. J. Guo, “A novel substrate-integrated coaxial line transverse slot array antenna,” *IEEE transactions on antennas and propagation*, vol. 67, pp. 6187–6192, 2019.
- [82] F. Zhu, W. Hong, J.-X. Chen, and K. Wu, “Ultra-Wideband Single and Dual Baluns Based on Substrate Integrated Coaxial Line Technology,” *IEEE Transactions on Microwave Theory and Techniques*, vol. 60, no. 10, pp. 3062–3070, 2012.
- [83] H. Ranasinghe and A. Gunawardena, “A novel substrate integrated coaxial line ring resonator design and performance evaluation,” in *2019 14th Conference on Industrial and Information Systems (ICIIS)*, 2019, pp. 5–10.
- [84] J. M. Merello, V. Nova, C. Bachiller, J. R. Sánchez, A. Belenguer, and V. E. Boria Esbert, “Miniaturization of power divider and 90° hybrid directional coupler for c-band applications using empty substrate-integrated coaxial lines,” *IEEE Transactions on Microwave Theory and Techniques*, vol. 66, no. 6, pp. 3055–3062, 2018.
- [85] L. Zhao, J. Shi, and K. Xu, “Broadband Coaxial Rotary Joint With Simple Substrate Integrated Waveguide Feeder,” *IEEE Access*, vol. 7, pp. 139 499–139 503, 2019.
- [86] Y. Yu, H. Luyen, and N. Behdad, “A Wideband Millimeter-Wave Rotman Lens Multibeam Array Using Substrate Integrated Coaxial Line (SICL) Technology,” *IEEE Transactions on Antennas and Propagation*, vol. 69, no. 11, pp. 7532–7542, 2021.
- [87] Y.-H. Yang, S.-G. Zhou, B.-H. Sun, and X.-Z. Gao, “Design of Wideband Circularly Polarized Antenna Array Excited by Substrate Integrated Coaxial Line for Millimeter-Wave Applications,” *IEEE Transactions on Antennas and Propagation*, vol. 69, no. 12, pp. 8943–8948, 2021.
- [88] Z.-J. Guo, Z.-C. Hao, H.-Y. Yin, D.-M. Sun, and G. Q. Luo, “Planar shared-aperture array antenna with a high isolation for millimeter-wave low earth orbit satellite communication system,” *IEEE Transactions on Antennas and Propagation*, vol. 69, pp. 7582–7592, 11 2021.
- [89] X. Dai, A. Li, and K. M. Luk, “A Wideband Compact Magnetolectric Dipole Antenna Fed by SICL for Millimeter Wave Applications,” *IEEE Transactions on Antennas and Propagation*, vol. 69, no. 9, pp. 5278–5285, 2021.

- [90] Z. Wen, X. Q. Lin, C. Li, J. Guo, and Y. L. Fan, “A Microwave Ablation Antenna Based on Substrate-Integrated Coaxial Line,” *IEEE Antennas and Wireless Propagation Letters*, vol. 20, no. 5, pp. 713–717, 2021.
- [91] K.-Y. Dong, X.-C. Li, K. Ning, and J.-F. Mao, “Formula Derivation of Characteristic Impedance of Substrate Integrated Coaxial Line,” in *2019 International Conference on Microwave and Millimeter Wave Technology (ICMMT)*, 2019, pp. 1–3.
- [92] X. Wei, X.-C. Li, N. Wang, Y. Shao, and J.-F. Mao, “A wide band millimeter-wave substrate integrated coaxial line (sicl) for high speed data transmission,” in *2015 Asia-Pacific Microwave Conference (APMC)*, vol. 3, 2015, pp. 1–3.
- [93] Y.-H. Yang, B.-H. Sun, G.-X. Zhang, and L. Shen, “Tfsiw-excited dual-polarized array antenna with 30° beam-pointing for millimeter-wave applications,” *IEEE transactions on antennas and propagation*, vol. 67, pp. 5740–5745, 2019.
- [94] S. Yang, Z. Yu, and J. Zhou, “A Low-Loss Broadband Planar Transition From Ground Coplanar Waveguide to Substrate-Integrated Coaxial Line,” *IEEE Microwave and Wireless Components Letters*, vol. 31, no. 11, pp. 1191–1194, 2021.
- [95] A. Belenguer, H. Esteban, and V. E. Boria, “Novel Empty Substrate Integrated Waveguide for High-Performance Microwave Integrated Circuits,” *IEEE Transactions on Microwave Theory and Techniques*, vol. 62, no. 4, pp. 832–839, 2014.
- [96] A. L. Borja, A. Belenguer, H. Esteban González, and V. E. Boria, “Design Procedure of Continuous Profile Stopband Filters Implemented With Empty Substrate Integrated Coaxial Lines,” *IEEE Transactions on Microwave Theory and Techniques*, vol. 68, no. 4, pp. 1520–1528, 2020.
- [97] A. L. Borja, A. Belenguer, H. Esteban, and V. E. Boria, “Design and Performance of a High-  $Q$  Narrow Bandwidth Bandpass Filter in Empty Substrate Integrated Coaxial Line at  $K_u$  -Band,” *IEEE Microwave and Wireless Components Letters*, vol. 27, no. 11, pp. 977–979, 2017.
- [98] L. Martinez, J. A. Martinez, A. L. Borja, H. Esteban, V. E. Boria, and A. Belenguer, “Compact Bandpass Filter in Empty Substrate Integrated Coaxial Line,” in *2018 48th European Microwave Conference (EuMC)*, 2018, pp. 162–165.
- [99] F. Quiles, Á. Belenguer, J. Á. Martínez, V. Nova, H. Esteban, and V. Boria, “Compact Microstrip to Empty Substrate-Integrated Coaxial Line Transition,” *IEEE Microwave and Wireless Components Letters*, vol. 28, no. 12, pp. 1080–1082, 2018.

- [100] K. Sun, B. Wang, T. Yang, S. Liu, Y. Chen, Y. Zhao, and D. Yang, “Dual-polarized Millimeter Wave End-fire Array Based on Substrate Integrated Mode-Composite Transmission Line,” *IEEE Transactions on Antennas and Propagation*, p. 1, 2021.
- [101] K. Ning, X.-C. Li, H. Zhang, and J. Mao, “Ridged Substrate Integrated Coaxial Line for Wideband Millimeter-Wave Transmission,” *IEEE Transactions on Microwave Theory and Techniques*, vol. 69, no. 6, pp. 2981–2988, 2021.
- [102] K. Ning, X.-C. Li, and J. Mao, “A Compact Ridged Substrate Integrated Coaxial Line,” in *2020 IEEE MTT-S International Wireless Symposium (IWS)*, 2020, pp. 1–3.
- [103] A. Li and K.-M. Luk, “Millimeter-Wave End-Fire Magneto-Electric Dipole Antenna and Arrays With Asymmetrical Substrate Integrated Coaxial Line Feed,” *IEEE Open Journal of Antennas and Propagation*, vol. 2, pp. 62–71, 2021.
- [104] A. Li and K.-m. Luk, “Ultra-Wideband Endfire Long-Slot-Excited Phased Array for Millimeter-Wave Applications,” *IEEE Transactions on Antennas and Propagation*, vol. 69, no. 6, pp. 3284–3293, 2021.
- [105] G.-W. Su, Y.-L. Shen, W. Hong, and M.-H. Ho, “Wide-Band Directional Coupler Design Using the Substrate Integrated Double-Strip Coaxial Line,” in *2019 IEEE Asia-Pacific Microwave Conference (APMC)*, 2019, pp. 1011–1013.
- [106] F. Xu and K. Wu, “Guided-wave and leakage characteristics of substrate integrated waveguide,” *IEEE Transactions on Microwave Theory and Techniques*, vol. 53, no. 1, pp. 66–73, 2005.
- [107] “<https://mpd.southwestmicrowave.com>.”
- [108] “<https://www.nsi-mi.com/products/system-solutions/near-field-systems>.”
- [109] M. Baggett, “Practical gain measurements”
- [110] K. Wu, M. Bozzi, and N. J. G. Fonseca, “Substrate integrated transmission lines: Review and applications,” *IEEE Journal of Microwaves*, vol. 1, no. 1, pp. 345–363, 2021.
- [111] A. Iqbal, J. J. Tiang, S. K. Wong, M. Alibakhshikenari, F. Falcone, and E. Limiti, “Miniaturization trends in substrate integrated waveguide (siw) filters: A review,” *IEEE Access*, vol. 8, pp. 223 287–223 305, 2020.

- [112] X.-P. Chen and K. Wu, "Substrate integrated waveguide filters: Design techniques and structure innovations," *IEEE Microwave Magazine*, vol. 15, no. 6, pp. 121–133, 2014.
- [113] Y. Cao, Y. Cai, L. Wang, Z. Qian, and L. Zhu, "A review of substrate integrated waveguide end-fire antennas," *IEEE Access*, vol. 6, pp. 66 243–66 253, 2018.
- [114] N. Nguyen-Trong and C. Fumeaux, "Half-mode substrate-integrated waveguides and their applications for antenna technology: A review of the possibilities for antenna design," *IEEE Antennas and Propagation Magazine*, vol. 60, no. 6, pp. 20–31, 2018.
- [115] G. Gentile, R. Dekker, P. de Graaf, M. Spirito, M. J. Pelk, L. C. N. de Vreede, and B. Rejaei Salmassi, "Silicon filled integrated waveguides," *IEEE Microwave and Wireless Components Letters*, vol. 20, no. 10, pp. 536–538, 2010.
- [116] D. Stephens, P. Young, and I. Robertson, "Millimeter-wave substrate integrated waveguides and filters in photoimageable thick-film technology," *IEEE Transactions on Microwave Theory and Techniques*, vol. 53, no. 12, pp. 3832–3838, 2005.
- [117] Y. Cassivi, L. Perregrini, P. Arcioni, M. Bressan, K. Wu, and G. Conciauro, "Dispersion characteristics of substrate integrated rectangular waveguide," *IEEE Microwave and Wireless Components Letters*, vol. 12, no. 9, pp. 333–335, 2002.
- [118] D. Deslandes and K. Wu, "Accurate modeling, wave mechanisms, and design considerations of a substrate integrated waveguide," *IEEE Transactions on Microwave Theory and Techniques*, vol. 54, no. 6, pp. 2516–2526, 2006.
- [119] D. Deslandes, "Design equations for tapered microstrip-to-substrate integrated waveguide transitions," in *2010 IEEE MTT-S International Microwave Symposium*, 2010, pp. 704–707.
- [120] Z. Kordiboroujeni and J. Bornemann, "New wideband transition from microstrip line to substrate integrated waveguide," *IEEE Transactions on Microwave Theory and Techniques*, vol. 62, no. 12, pp. 2983–2989, 2014.
- [121] Y. Ding and K. Wu, "Substrate integrated waveguide-to-microstrip transition in multilayer substrate," *IEEE Transactions on Microwave Theory and Techniques*, vol. 55, no. 12, pp. 2839–2844, 2007.
- [122] D. Deslandes and K. Wu, "Analysis and design of current probe transition from grounded coplanar to substrate integrated rectangular waveguides," *IEEE Transactions on Microwave Theory and Techniques*, vol. 53, no. 8, pp. 2487–2494, 2005.

- [123] A. Patrovsky, M. Daigle, and K. Wu, “Millimeter-wave wideband transition from cpw to substrate integrated waveguide on electrically thick high-permittivity substrates,” in *2007 European Microwave Conference*, 2007, pp. 138–141.
- [124] S. Lee, S. Jung, and H.-Y. Lee, “Ultra-wideband cpw-to-substrate integrated waveguide transition using an elevated-cpw section,” *IEEE Microwave and Wireless Components Letters*, vol. 18, no. 11, pp. 746–748, 2008.
- [125] D. Deslandes and K. Wu, “Integrated transition of coplanar to rectangular waveguides,” in *2001 IEEE MTT-S International Microwave Symposium Digest (Cat. No.01CH37157)*, vol. 2, 2001, pp. 619–622 vol.2.
- [126] T. J. Coenen, D. J. Bekers, J. L. Tauritz, and F. E. van Vliet, “Design and measurement of metallic post-wall waveguide components,” in *2009 IEEE MTT-S International Microwave Symposium Digest*, 2009, pp. 261–264.
- [127] X.-P. Chen and K. Wu, “Low-loss ultra-wideband transition between conductor-backed coplanar waveguide and substrate integrated waveguide,” in *2009 IEEE MTT-S International Microwave Symposium Digest*, 2009, pp. 349–352.
- [128] S. Ebadi, N. Landy, M. Perque, T. Driscoll, and D. Smith, “Wideband coaxial to substrate-integrated waveguide transition in a multilayer reconfigurable antenna configuration,” in *2014 IEEE Antennas and Propagation Society International Symposium (APSURSI)*, 2014, pp. 454–455.
- [129] W. M. Abdel-Wahab, H. Al-Saedi, A. Palizban, A. Ehsandar, and S. Safavi-Naeini, “Siw-to-mini-coaxial vertical transition for low profile mm-wave pcb-to-pcb assembly,” in *2019 IEEE International Symposium on Antennas and Propagation and USNC-URSI Radio Science Meeting*, 2019, pp. 961–962.
- [130] A. A. Khan and M. K. Mandal, “A compact broadband direct coaxial line to siw transition,” *IEEE Microwave and Wireless Components Letters*, vol. 26, no. 11, pp. 894–896, 2016.
- [131] J. Xu, W. Hong, H. Tang, Z. Kuai, and K. Wu, “Half-mode substrate integrated waveguide (hmsiw) leaky-wave antenna for millimeter-wave applications,” *IEEE Antennas and Wireless Propagation Letters*, vol. 7, pp. 85–88, 2008.
- [132] M. Li, Q. Ji, C. Chen, W. Chen, and H. Zhang, “A triple-mode bandpass filter with controllable bandwidth using qmsiw cavity,” *IEEE Microwave and Wireless Components Letters*, vol. 28, no. 8, pp. 654–656, 2018.

- [133] C. Zhong, J. Xu, Z. Yu, M. Wang, and J. Li, “Half mode substrate integrated waveguide broadband bandpass filter using photonic band gap structures,” in *2008 International Conference on Microwave and Millimeter Wave Technology*, vol. 1, 2008, pp. 22–24.
- [134] L.-S. Wu, X.-L. Zhou, W.-Y. Yin, C.-T. Liu, L. Zhou, J.-F. Mao, and H.-L. Peng, “A new type of periodically loaded half-mode substrate integrated waveguide and its applications,” *IEEE Transactions on Microwave Theory and Techniques*, vol. 58, no. 4, pp. 882–893, 2010.
- [135] N. Nguyen-Trong, T. Kaufmann, L. Hall, and C. Fumeaux, “Analysis and design of a reconfigurable antenna based on half-mode substrate-integrated cavity,” *IEEE Transactions on Antennas and Propagation*, vol. 63, no. 8, pp. 3345–3353, 2015.
- [136] L.-S. Wu, X.-L. Zhou, and W.-Y. Yin, “Evanescent-mode bandpass filters using folded and ridge substrate integrated waveguides (siws),” *IEEE Microwave and Wireless Components Letters*, vol. 19, no. 3, pp. 161–163, 2009.
- [137] A. R. Mallahzadeh and S. Esfandiarpour, “Wideband h-plane horn antenna based on ridge substrate integrated waveguide (rsiw),” *IEEE Antennas and Wireless Propagation Letters*, vol. 11, pp. 85–88, 2012.
- [138] S. Moscato, R. Moro, M. Pasian, M. Bozzi, and L. Perregrini, “Two-material ridge substrate integrated waveguide for ultra-wideband applications,” *IEEE Transactions on Microwave Theory and Techniques*, vol. 63, no. 10, pp. 3175–3182, 2015.
- [139] E. Massoni, M. Bozzi, and K. Wu, “Increasing efficiency of leaky-wave antenna by using substrate integrated slab waveguide,” *IEEE Antennas and Wireless Propagation Letters*, vol. 18, no. 8, pp. 1596–1600, 2019.
- [140] E. Massoni, L. Silvestri, G. Alaimo, S. Marconi, M. Bozzi, L. Perregrini, and F. Auricchio, “3-d printed substrate integrated slab waveguide for single-mode bandwidth enhancement,” *IEEE Microwave and Wireless Components Letters*, vol. 27, no. 6, pp. 536–538, 2017.
- [141] M. D. Fernandez, J. A. Ballesteros, and A. Belenguer, “Design of a hybrid directional coupler in empty substrate integrated waveguide (esiw),” *IEEE Microwave and Wireless Components Letters*, vol. 25, no. 12, pp. 796–798, 2015.
- [142] D. Herraiz, H. Esteban, J. A. Martínez, A. Belenguer, and V. Boria, “Microstrip to ridge empty substrate-integrated waveguide transition for broadband microwave

- applications,” *IEEE Microwave and Wireless Components Letters*, vol. 30, no. 3, pp. 257–260, 2020.
- [143] J. A. Martinez, J. J. de Dios, A. Belenguer, H. Esteban, and V. E. Boria, “Integration of a very high quality factor filter in empty substrate-integrated waveguide at q-band,” *IEEE Microwave and Wireless Components Letters*, vol. 28, no. 6, pp. 503–505, 2018.
- [144] A. Belenguer, M. D. Fernandez, J. A. Ballesteros, J. J. de Dios, H. Esteban, and V. E. Boria, “Compact multilayer filter in empty substrate integrated waveguide with transmission zeros,” *IEEE Transactions on Microwave Theory and Techniques*, vol. 66, no. 6, pp. 2993–3000, 2018.
- [145] A. Niembro-Martín, V. Nasserddine, E. Pistono, H. Issa, A.-L. Franc, T.-P. Vuong, and P. Ferrari, “Slow-wave substrate integrated waveguide,” *IEEE Transactions on Microwave Theory and Techniques*, vol. 62, no. 8, pp. 1625–1633, 2014.
- [146] Y. Zhang, J.-Y. Deng, D. Sun, J.-Y. Yin, L.-X. Guo, X.-H. Ma, and Y. Hao, “Slow wave substrate-integrated waveguide with miniaturized dimensions and broadened bandwidth,” *IEEE Transactions on Microwave Theory and Techniques*, vol. 69, no. 8, pp. 3675–3683, 2021.
- [147] X. Li, K. Dhawaj, and T. Itoh, “Single-layer slow-wave substrate integrated waveguide with enhanced capacitance,” in *2018 IEEE/MTT-S International Microwave Symposium - IMS*, 2018, pp. 316–318.
- [148] H. Jin, Y. Zhou, Y. M. Huang, and K. Wu, “Slow-wave propagation properties of substrate integrated waveguide based on anisotropic artificial material,” *IEEE Transactions on Antennas and Propagation*, vol. 65, no. 9, pp. 4676–4683, 2017.
- [149] H. Jin, K. Wang, J. Guo, S. Ding, and K. Wu, “Slow-wave effect of substrate integrated waveguide patterned with microstrip polyline,” *IEEE Transactions on Microwave Theory and Techniques*, vol. 64, no. 6, pp. 1717–1726, 2016.
- [150] Y. Zhou, Y. M. Huang, H. Jin, D. Xu, S. Ding, L. Silvestri, M. Bozzi, and L. Perregini, “Effective extracting method for electromagnetic parameters of periodically loaded substrate integrated waveguide units,” in *2018 IEEE/MTT-S International Microwave Symposium - IMS*, 2018, pp. 1050–1053.

- [151] H. Jin, Y. Zhou, Y. M. Huang, S. Ding, and K. Wu, “Miniaturized broadband coupler made of slow-wave half-mode substrate integrated waveguide,” *IEEE Microwave and Wireless Components Letters*, vol. 27, no. 2, pp. 132–134, 2017.
- [152] J. Qiang, F. Xu, L. Yang, and J. Zhan, “Enhanced performance of multilayer band-pass filter using slow-wave empty substrate- integrated waveguide (sw-esiw),” *IEEE Microwave and Wireless Components Letters*, vol. 31, no. 12, pp. 1279–1282, 2021.
- [153] F. Xu and K. Wu, “Guided-wave and leakage characteristics of substrate integrated waveguide,” *IEEE Transactions on Microwave Theory and Techniques*, vol. 53, pp. 66–73, 1 2005.
- [154] Y. J. Cheng, J. Wang, and X. L. Liu, “94 ghz substrate integrated waveguide dual-circular-polarization shared-aperture parallel-plate long-slot array antenna with low sidelobe level,” *IEEE Transactions on Antennas and Propagation*, vol. 65, pp. 5855–5861, 11 2017.
- [155] C.-X. Mao, S. Gao, Y. Wang, Q.-X. Chu, and X.-X. Yang, “Dual-band circularly polarized shared-aperture array for  $c$  -/  $x$  -band satellite communications,” *IEEE Transactions on Antennas and Propagation*, vol. 65, pp. 5171–5178, 10 2017.
- [156] M. Ferrando-Rocher, J. I. Herranz-Herruzo, A. Valero-Nogueira, and B. Bernardo-Clemente, “Full-metal k-ka dual-band shared-aperture array antenna fed by combined ridge-groove gap waveguide,” *IEEE Antennas and Wireless Propagation Letters*, vol. 18, pp. 1463–1467, 7 2019.
- [157] Y. Chen, J. Zhao, and S. Yang, “A novel stacked antenna configuration and its applications in dual-band shared-aperture base station antenna array designs,” *IEEE Transactions on Antennas and Propagation*, vol. 67, no. 12, pp. 7234–7241, 2019.
- [158] K. Wang, X. Liang, W. Zhu, J. Geng, J. Li, Z. Ding, and R. Jin, “A dual-wideband dual-polarized aperture-shared patch antenna with high isolation,” *IEEE Antennas and Wireless Propagation Letters*, vol. 17, no. 5, pp. 735–738, 2018.
- [159] W.-W. Yang, X.-Y. Dong, W.-J. Sun, and J.-X. Chen, “Polarization reconfigurable broadband dielectric resonator antenna with a lattice structure,” *IEEE Access*, vol. 6, pp. 21 212–21 219, 2018.
- [160] A. A. Qureshi, D. M. Klymyshyn, M. Tayfeh, W. Mazhar, M. Borner, and J. Mohr, “Template-based dielectric resonator antenna arrays for millimeter-wave applications,” *IEEE Transactions on Antennas and Propagation*, vol. 65, pp. 4576–4584, 9 2017.

- [161] M. S. Abdallah, Y. Wang, W. M. Abdel-Wahab, and S. Safavi-Naeini, "Design and optimization of siw center-fed series rectangular dielectric resonator antenna array with 45° linear polarization," *IEEE Transactions on Antennas and Propagation*, vol. 66, no. 1, pp. 23–31, 2018.
- [162] F. Calignano, D. Manfredi, E. P. Ambrosio, S. Biamino, M. Lombardi, E. Atzeni, A. Salmi, P. Minetola, L. Iuliano, and P. Fino, "Overview on additive manufacturing technologies," *Proceedings of the IEEE*, vol. 105, pp. 593–612, 4 2017.
- [163] P. Nayeri, M. Liang, R. A. Sabory-Garcia, M. Tuo, F. Yang, M. Gehm, H. Xin, and A. Z. Elsherbeni, "3d printed dielectric reflectarrays: Low-cost high-gain antennas at sub-millimeter waves," *IEEE Transactions on Antennas and Propagation*, vol. 62, pp. 2000–2008, 4 2014.
- [164] "<https://speag.swiss/products/dak/dak-tl-2/>."
- [165] A. Fallahi, S. Hashemizadeh, and N. Kuster, "On the dielectric measurement of thin layers using open-ended coaxial probes," *IEEE Transactions on Instrumentation and Measurement*, vol. 70, pp. 1–8, 2021.
- [166] M. Bailey and C. Swift, "Input admittance of a circular waveguide aperture covered by a dielectric slab," *IEEE Transactions on Antennas and Propagation*, vol. 16, pp. 386–391, 7 1968.
- [167] J. Huang, S. J. Chen, Z. Xue, W. Withayachumnankul, and C. Fumeaux, "Wideband endfire 3-d-printed dielectric antenna with designable permittivity," *IEEE Antennas and Wireless Propagation Letters*, vol. 17, pp. 2085–2089, 11 2018.
- [168] M. Ferrando-Rocher, J. I. Herranz-Herruzo, A. Valero-Nogueira, and M. Baquero-Escudero, "Dual-band single-layer slot array antenna fed by  $k$  - /  $ka$  -band dual-mode resonators in gap waveguide technology," *IEEE Antennas and Wireless Propagation Letters*, vol. 20, pp. 416–420, 3 2021.
- [169] J. Baker-Jarvis, M. Janezic, P. Domich, and R. Geyer, "Analysis of an open-ended coaxial probe with lift-off for nondestructive testing," *IEEE Transactions on Instrumentation and Measurement*, vol. 43, pp. 711–718, 1994.
- [170] C. L. Brace and S. Etoz, "An analysis of open-ended coaxial probe sensitivity to heterogeneous media," *Sensors*, vol. 20, p. 5372, 9 2020.

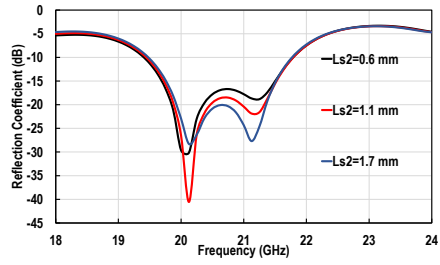
# APPENDICES

# Appendix A

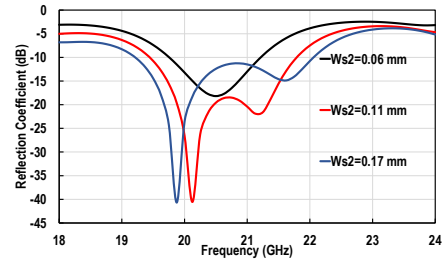
## sensitivity analysis 1

### A.1 Sensitivity of SICL-DRA Design Parameters

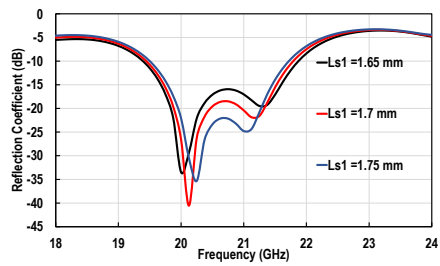
This section presents the sensitivity analysis for SICL-fed DRA design parameters. The sensitivity analysis is performed by considering a possible 2 mils oversize in the design dimensions after the manufacturing process.



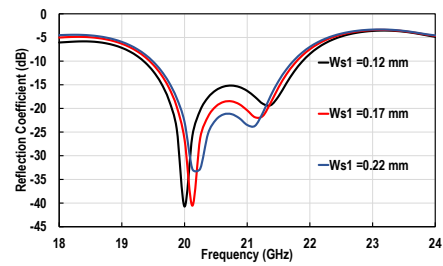
(a)



(b)

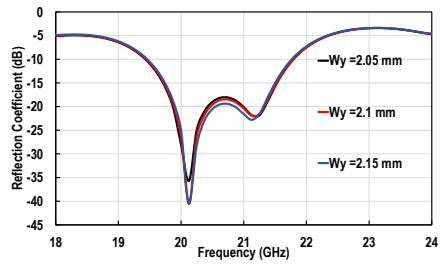


(c)

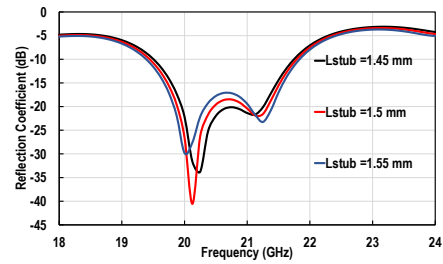


(d)

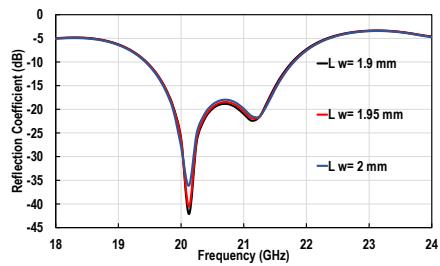
Figure A.1: Reflection coefficient variation with a)  $L_{S2}$  b)  $W_{S2}$  c)  $L_{S1}$  d)  $W_{S1}$



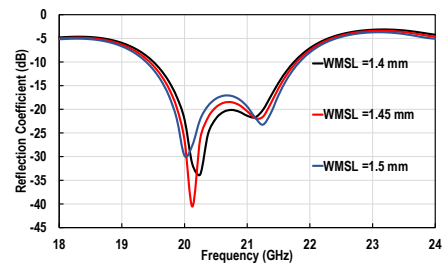
(a)



(b)

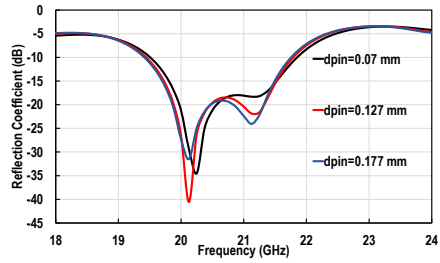


(c)

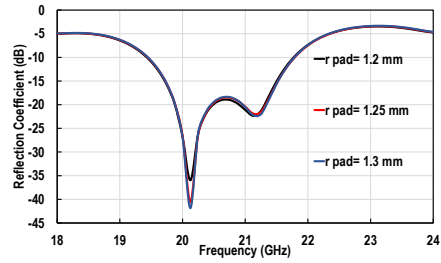


(d)

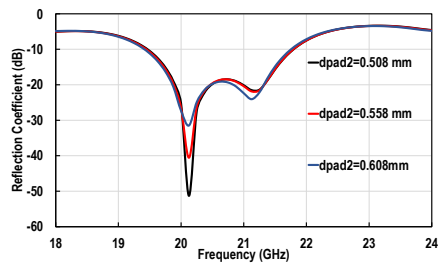
Figure A.2: Reflection coefficient variation with a)  $W_y$  b)  $L_{Stub}$  c)  $L_w$  d)  $W_{MSL}$



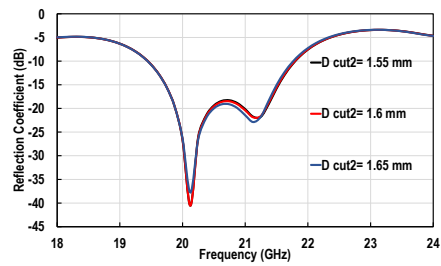
(a)



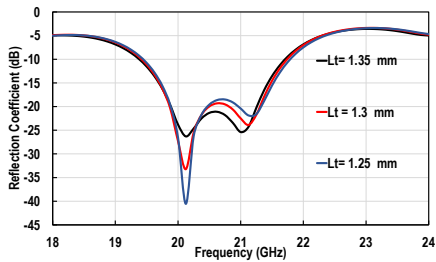
(b)



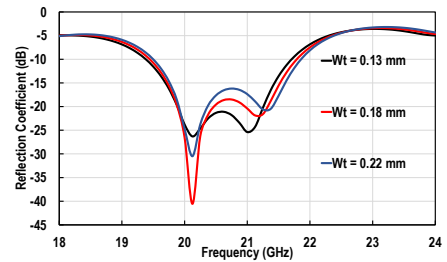
(c)



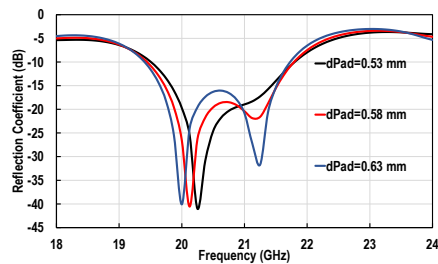
(d)

Figure A.3: Reflection coefficient variation with a)  $d_{pin}$  b)  $r_{pad}$  c)  $D_{pad2}$  d)  $D_{cut2}$ 

(a)

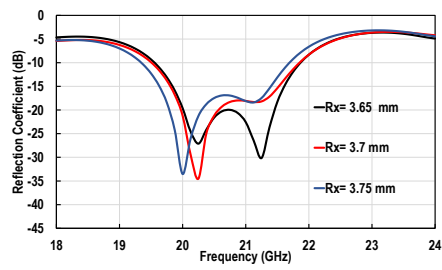


(b)

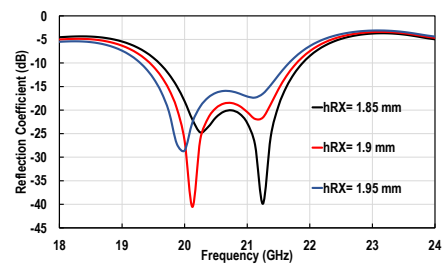


(c)

Figure A.4: Reflection coefficient variation with a)  $L_t$  b)  $W_t$  c)  $d_{pad}$



(a)



(b)

Figure A.5: Reflection coefficient variation with a)  $R_x$  b)  $h_{Rx}$

# Appendix B

## Sensitivity analysis 2

### B.1 Sensitivity of SIW-DRA Design Parameters

This section presents the sensitivity analysis for SIW-fed DRA design parameters. The sensitivity analysis is performed by considering a possible 2 mils oversize in the design dimensions after manufacturing.

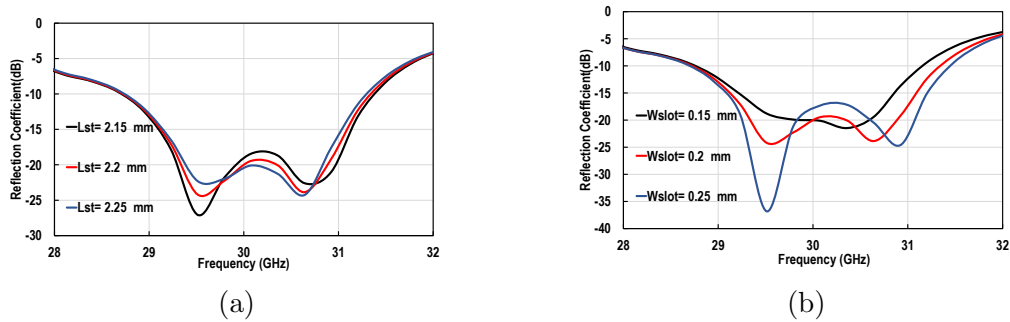


Figure B.1: Reflection coefficient variation with a)  $L_{st}$  b)  $W_{slot}$

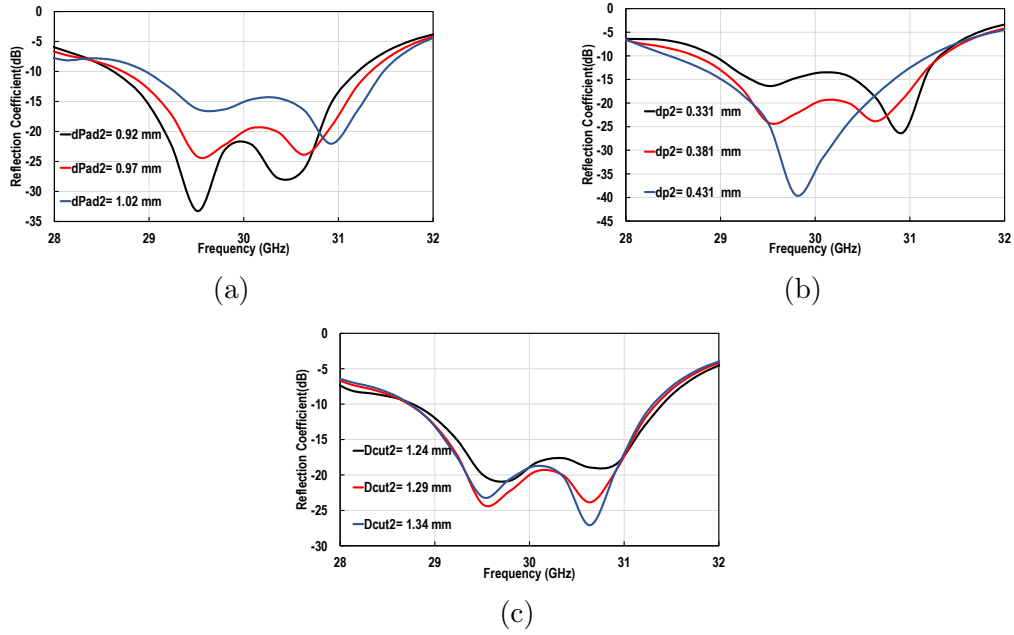


Figure B.2: Reflection coefficient variation with a)  $d_{pad2}$  b)  $d_{dp2}$  c)  $D_{cut2}$

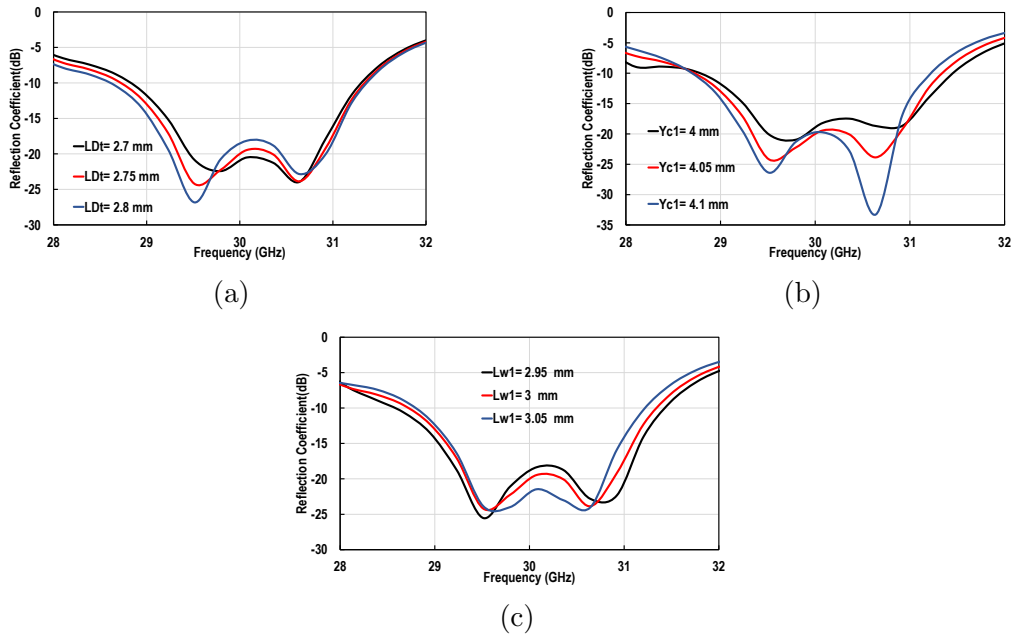
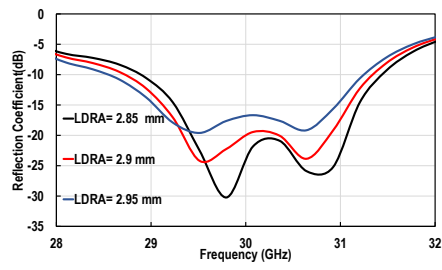
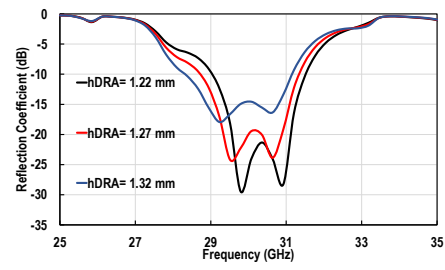


Figure B.3: Reflection coefficient variation with a)  $L_{Dt}$  b)  $Y_{c1}$  c)  $L_{w1}$



(a)



(b)

Figure B.4: Reflection coefficient variation with a)  $L_{DRA}$  b)  $h_{DRA}$